UNIVERSITÀ
DEGLI STUDI
DI PADOVA

Head Office: Università degli Studi di Padova

Department of Geosciences

Ph.D. COURSE IN: EARTH SCIENCES
SERIES XXXI

POLYMODAL FAULTING IN RIFTING SETTINGS: STRAIN FIELD AND ROLE OF PRE-EXISTING STRUCTURES

Coordinator: Prof. Claudia Agnini
Supervisor: Dr. Anna Breda
Co-Supervisor: Prof. Matteo Massironi

Ph.D. student: Luca Collanega

CONTENTS

Acknowledgements

Above all, I owe my special gratitude to my supervisors Dr. Anna Breda and Prof. Matteo Massironi. They constantly helped me during these three years, with their scientific competence and by motivating me with their enthusiasm and dedication.

I thank also Prof. Christopher Jackson for making my stay at Imperial College possible and Prof. Giacomo Corti for his help during my time at the Tectonic Lab of the University of Florence.

Oliver Duffy and Catherine Homberg are greatly acknowledged for their thorough review of this thesis and for pointing out future developments of this work.

I thank my family, to whom I dedicate this thesis, for being constantly a support to me and putting always my aspirations above theirs.

A special thank goes to my friend Marta Piloni. Our twenty-year friendship was an invaluable strength to me in some of the darkest moments of my PhD.

I thank all my friends at the Geosciences Department: Marta Cosma, Chiara Balestrieri, Carlotta Cappelli, Arianna Marcolla and Arianna Vettorello.

Finally, I would like to thank everyone who helped me during these three years by saying something or by not saying anything.

ABSTRACT

Normal faults have been typically thought to develop sub-perpendicularly to the extension direction, forming systems of sub-parallel faults. However, a variety of processes may result in the simultaneous development of faults with different strikes (i.e. polymodal faulting), most notably 3D strain fields and influence of pre-existing fabrics. Whilst the classic model on faulting suggests that complex fault patterns should result from polyphase deformation with different extension directions, the concept of polymodal faulting can account for the development of different fault sets under the same stress regime, having possibly a strong impact on the reconstruction of the palaeostress.

In the thesis, 3D seismic data were used to assess the occurrence of polymodal faulting in two different extensional tectonic settings: the Barents Sea rift-shear margin (**Paper 1**), offshore northern Norway, and the Taranaki back-arc rift (**Paper 3**), offshore New Zealand. Then, analogue models and kinematic analysis were used to investigate the deformation processes. In both settings, polymodal faulting was observed at the 10s of kilometres scale. The occurrence of polymodal faulting at such large scale may affect the previous interpretation of the structural histories of these sedimentary basins, reducing the number of tectonic phases that should be envisaged to explain the observed structures.

The tectonic setting appears to have a strong influence on the deformation processes, with polymodal faulting occurring under the control of a 3D strain field in the Barents Sea and of pre-existing basement fabrics in the Taranaki Basin. In the Barents Sea, the onset of a 3D strain field is related to the interaction between the Atlantic and the Arctic rifts, coupled with a characteristic brittle-ductile-brittle mechanical stratigraphy. The analogue models performed in this thesis (**Paper 2**) highlighted that in 3D strain fields, local fault interactions exert a strong control on the final fault geometries, with the faults forming perpendicular one to the other rather than in orthorhombic symmetry with respect to the principal strain axes as previously thought. In the Taranaki back-arc rift, despite the absence of extensional reactivation of the intra-basement structures, they appear to have exerted a strong control on the distribution and strike of normal faults. The growth history of normal faults highlighted that preferential nucleation/propagation within pre-existing weakness zones and local perturbation of the regional stress field may be effective mechanisms through which pre-existing structures can influence normal faults, even without their direct extensional reactivation.

In conclusion, complex fault patterns may not necessarily reflect a complex tectonic history, but can result from the dynamics of deformation processes, which appear to be strongly susceptible to the local influences of developing as well as pre-existing structures.

RIASSUNTO

Il modello classico della fagliazione (ovvero la teoria di Mohr-Coulomb) prevede che in un regime estensionale le faglie si formino perpendicolarmente alla direzione di estensione, dando luogo a sistemi di faglie sub-parallele fra loro. Tuttavia, una varietà di meccanismi possono portare allo sviluppo simultaneo di faglie con diverse orientazioni, detto fagliazione polimodale. In particolare, campi di strain 3D e l'influenza da parte di strutture pre-esistenti potrebbero portare allo sviluppo simultaneo di diversi sistemi di faglie in modo pervasivo e su ampia scala. A differenza del modello classico della fagliazione, il concetto di fagliazione polimodale può pertanto spiegare lo sviluppo simultaneo di diversi sistemi di faglie nell'ambito di un unico campo di stress. Adottare un modello o l'altro può dunque avere un impatto drastico sulla ricostruzione dell'evoluzione tettonica di un'area.

In questa tesi, si sono usati dati sismici 3D per valutare il presentarsi di fagliazione polimodale in due diversi contesti tettonici estensionali: il Mare di Barents (**Articolo 1**), un margine di rift-shear al largo della Norvegia Settentrionale, ed il Bacino del Taranaki (**Articolo 3**), un rift di retro-arco al largo della costa occidentale della Nuova Zelanda. Successivamente, i dati sismici sono stati integrati con modelli analogici e dettagliate ricostruzioni della storia cinematica di specifici piani di faglia al fine di meglio comprendere i meccanismi deformativi. In entrambi i contesti, la fagliazione polimodale è stata osservata alla scala delle decine di chilometri, suggerendo la rilevanza di questo processo in termini tettonici. Il verificarsi di fagliazione polimodale ad ampia scala implicherebbe infatti una riduzione del numero di fasi tettoniche necessarie per giustificare le strutture osservate, modificando l'attuale visione dell'evoluzione strutturale di questi bacini sedimentari.

Il confronto fra le due aree suggerisce che il contesto tettono-stratigrafico giochi un ruolo fondamentale sui meccanismi alla base della fagliazione polimodale. Nel caso del Mare di Barents, la fagliazione polimodale risulta essere l'espressione di un campo di strain 3D legato all'interazione fra rifting Artico e Atlantico; sebbene anche il disaccoppiamento fra deformazione superficiale e profonda dovuto ai livelli con reologia duttile sembra essere stato un fattore fondamentale. Nel caso del Bacino del Taranaki, invece, la fagliazione polimodale sembra essere avvenuta sotto il controllo di strutture profonde, ereditate da fasi tettoniche compressive precedenti al rifting.

La ricostruzione dei processi deformativi nelle due aree ha portato a rivedere i modelli esistenti della deformazione 3D (nel caso del Barents) e dell'eredità strutturale (nel caso del Taranaki). Da una parte, i modelli analogici della deformazione 3D (**Articolo 2**) hanno evidenziato come le faglie

tendano a svilupparsi perpendicolarmente le une alle altre, piuttosto che con simmetria ortorombica rispetto agli assi della distensione, come previsto dal modello classico di Reches (1978). Questa tesi suggerisce pertanto che le interazioni locali tra faglie siano il principale meccanismo di controllo sulle geometrie finali in campi di strain 3D. Dall'altra parte, lo studio del Taranaki ha posto in luce come strutture profonde del basamento cristallino possano esercitare una notevole influenza sulla distribuzione e orientazione delle faglie normali, malgrado l'assenza di una diretta riattivazione estensionale delle stesse. La nucleazione/propagazione preferenziale delle faglie normali da anisotropie pre-esistenti e perturbazioni locali del campo di stress regionale sembrano essere meccanismi alternativi alla riattivazione estensionale, attraverso cui strutture pre-esistenti possono esercitare una forte influenza sulle faglie normali.

In conclusione, questa tesi dimostra che sistemi di faglie complessi non necessariamente sono legati ad una complessa storia strutturale, consistente di molteplici fasi tettoniche. La complessità dei processi deformativi, ed in particolare la suscettibilità di questi a strutture pre-esistenti o in fase di formazione, può infatti spiegare lo sviluppo di sistemi di faglie complessi anche nell'ambito di un'unica fase tettonica.

INTRODUCTION

1. Background

The classic Mohr-Coulomb theory predicts the development of conjugate fault sets striking parallel to the intermediate principal stress axis σ_2, assuming the deformation to be planar (Fig. 1a; Anderson, 1951). According to this simple model, the extension of a homogeneous material should result in the development of a single system of faults orthogonal to the least principal stress σ_3 (*i.e.* the extension direction; *e.g.* Gawthorpe and Leeder, 2008). Hence, multiple rotations of the stress fields are required to explain the complex fault patterns commonly observed in rifting settings, with fault sets striking along different directions (*e.g.* the North Sea, Whipp *et al*., 2014; the Gulf of Suez, Younes and McClay, 2002; the Gulf of Aden, Bellahansen *et al.*, 2013). However, the simultaneous development of different fault sets (*i.e.* polymodal faulting) has been suggested in several settings based on the crosscutting relationships between different fault sets and the architecture of growth strata (Healy *et al.*, 2015; Reeve *et al.*, 2015 and references therein). Polymodal fault systems are often local features, being clearly associated to large faults, or are the expression of the mobilisation of specific sedimentary units (Duffy *et al.*, 2015 and references therein). Indeed, local perturbation of the regional stress field due to fault slip (Maerten *et al.*, 2002), accommodation of along-strike variations of displacement (Destro, 1995; Stewart, 2001) and breaching of relay zones (Trudgill, 2002) may result in the development of secondary faults striking obliquely to major faults. Alternatively, gravity gliding above salt and mud layers (*e.g.* Stewart and Clark, 1999) or compaction and dewatering of clayey intervals (*e.g.* Cartwright and Lonergan, 1996) may lead to development of complex fault patterns within specific stratigraphic intervals. However, the onset of 3D stress fields ($\sigma_1 > \sigma_2 > \sigma_3$) and the influence of well-distributed basement fabrics could possibly result in the development of pervasive polymodal fault systems, representing viable alternative mechanisms with respect to multiple rotations of the extension direction. To interpret correctly the occurrence of polymodal faulting and its driving mechanism is crucial to infer the palaeo-stress and, thus, to reconstruct the tectonic evolution of an area. The accommodation of 3D stress fields has long been reported to require the simultaneous development and activity of different fault sets, with the mathematical model of Reches (1978) first proving the onset of at least four fault sets in a 3D strain field.

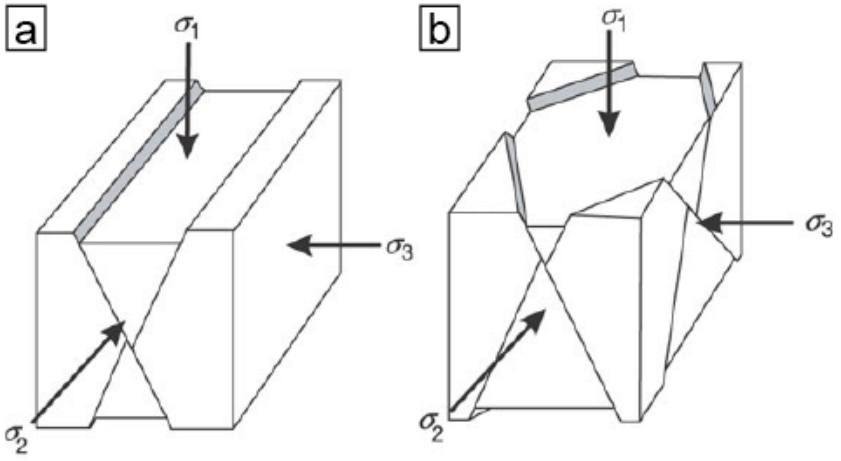

Fig. 1. Comparison between the Anderson's (a) and Reches' (b) models of faulting. (a) Note that the faults strike parallel to σ_2 and perpendicular to σ_3. (b) Note that the faults are arranged in orthorhombic symmetry, with σ_2 and σ_3 oriented along the bisectors of their intersection angles (modified after Healy *et al.*, 2006).

Assuming homogeneous and stable stress/strain distribution, Reches (1978) predicted that the four sets of faults should develop symmetrically with respect to the intermediate and the least principal stress (σ_2, σ_3), resulting in orthorhombic symmetry (Fig. 1b). This theoretical model is supported by both natural and laboratory examples, with orthorhombic arrangements being widely observed at the scale of microfractures (*i.e.* <1 mm; *e.g.* Aydin and Reches, 1982, Reches and Dieterich 1983) and meso-fractures (*i.e.* <10 mm; *e.g.* Krantz, 1988; Healy *et al.*, 2006). However, the geological literature on normal faults at larger scales (>100 m) is still dominated by bimodal fault patterns, with few examples of orthorhombic arrangements observed at the scale of kilometres (Krantz, 1988; Bistacchi and Massironi, 2000; Miller *et al.*, 2007; Franceschi *et al.*, 2014). The onset of 3D strain fields at the km-scale may (i) be restricted to specific tectonic settings and/or (ii) be hindered by the presence of pre-existing weaknesses. Furthermore, the model of Reches may be scale-dependent, representing a general model for the deformation at the scale of fractures but being of limited applicability at the scale of faults. Indeed, Reches himself described his analysis as "incomplete" (Reches, 1978), as it assumed the entire fault system to develop simultaneously. However, local interactions between developing faults have been shown to exert a first-order control on their nucleation and propagation, affecting strongly the final fault pattern (Gupta and Scholz, 2000).

On the other hand, the influence by deep basement fabrics can lead to the development of misoriented faults, strongly oblique (up to 60°) with respect to the regional extension direction (Morley *et al.*, 2004). As oblique faults are developing under the influence of basement fabrics, new normal faults can simultaneously develop orthogonal to the extension direction, resulting in polymodal faulting (Morley *et al.*, 2004; Reeve *et al.*, 2015). Depending on the scale and

distribution of the intra-basement fabrics, these polymodal systems could possibly be spread across wide areas. Although deep intra-basement fabrics appear to control the large-scale structure of several rifts (*e.g.* the North Sea, Bartholomew *et al.*, 1993; the Barents Sea, Gernigon *et al.*, 2014; the East African Rift, Ring, 1994), their influence on individual faults is less clear. Indeed, 3D seismic data highlighted various possible geometric relationships between intra-basement structures and normal faults, with the latter merging, exploiting and crosscutting the former (Fig. 2; Reeve *et al*., 2013; Bird *et al.*, 2015; Phillips *et al.*, 2016). These variable geometric relationships suggest that (i) different factors control whether and to which extent intra-basement fabrics influence normal faults (*e.g.* dip, obliquity, relative strength, spacing; Morley *et al.*, 2004) and that (ii) simple extensional reactivation is not the sole mechanism through which intra-basement structures can influence normal faults. In particular, pervasive intra-basement fabrics have been suggested to re-orient locally the regional stress field (Reeve *et al.*, 2015), having possibly a far-reaching influence on normal faults in the sedimentary cover.

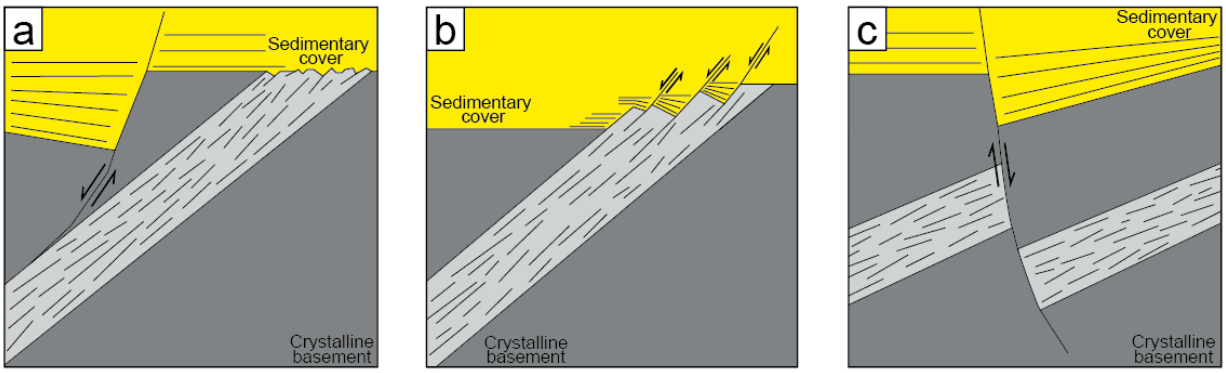

Fig. 2. Scheme of the possible geometric relationships between intra-basement structures and rift-related normal faults identified by Phillips *et al.* (2016). Normal faults can merge with (a), exploit (b) or crosscut (c) intra-basement shear zones (modified after Phillips *et al.*, 2016).

2. Study areas

During my PhD, I analysed faulting in two different extensional tectonic settings: the rift-shear Barents Sea margin and the back-arc rift Taranaki Basin.

The first case study (**Paper 1**) is represented by an area of 10,000 km^2 across the Hoop Fault Complex, one of the major structural lineaments of the Barents Sea (offshore northern Norway). The present day structure of the Barents platform consists of a fan-shaped array of basins and highs (*e.g.* Gabrielsen *et al.*, 1990; Faleide *et al.*, 1993), which developed during a long extensional history starting in the late Carboniferous and leading to the opening of the Norwegian-Greenland Sea in the Oligocene (*e.g.* Faleide *et al.*, 2008 and references therein; Fig. 3).

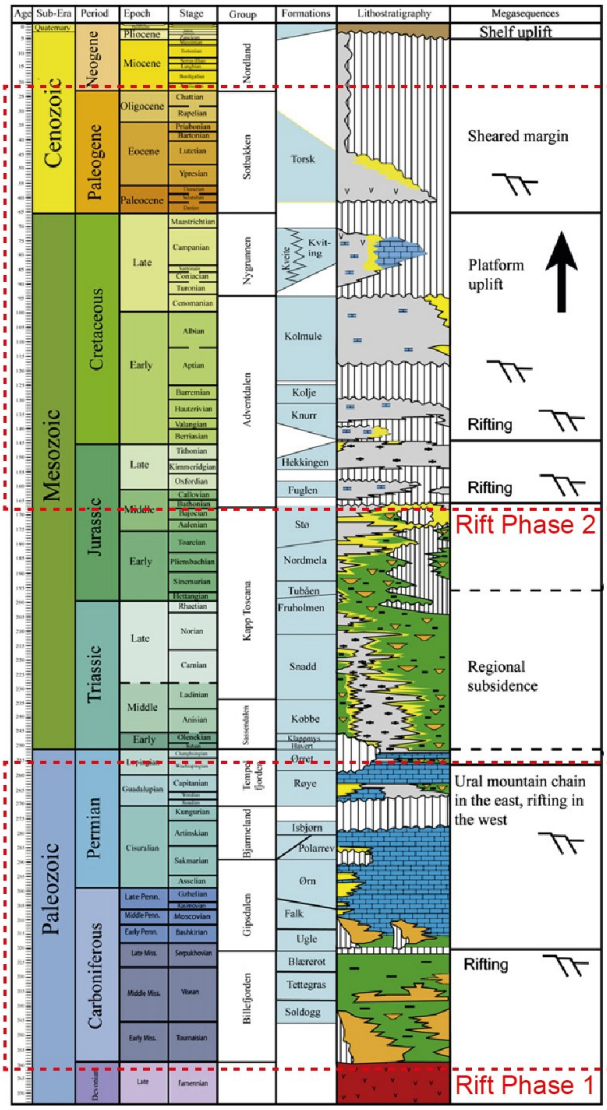

Fig. 3. Schematic diagram of the tectonic evolution of the Barents Sea. Note the two major rifting events in the late Carboniferous-Permian and in the late Mesozoic-Cenozoic (modified after Glørstad-Clark *et al.*, 2010).

Two main rifting phases occurred in the late Carboniferous-Permian (*e.g.* Gudlaugsson *et al.*, 1998) and in the late Mesozoic-Cenozoic (*e.g.* Faleide *et al.*, 1993) respectively, with an intervening phase of tectonic quiescence and regional subsidence in the Triassic (Glørstad-Clark *et al.*, 2010; 2011; Fig. 3). In particular, several rift pulses occurred during the late Mesozoic-Cenozoic, reflecting the interplay between the Atlantic and the Arctic stress regimes (*e.g.* Faleide *et al.*, 1993; Faleide *et al.*, 2008; Serck *et al.*, 2017). Being a transitional area between the shallow platform and deep marginal basins (Gabrielsen *et al.*, 1990), the Hoop Fault Complex presents excellent seismic resolution of the earliest rift structures, representing an ideal setting to evaluate the interaction between the Atlantic and the Arctic rifts at their onset.

The second case study (**Paper 3**) is represented by an area of 1500 km^2 on the uplifted western margin of the Taranaki Basin, offshore New Zealand. The Taranaki Basin first developed as a rift basin during the Late Cretaceous-Paleocene in relation to the break-up of Gondwana (*e.g.* Giba *et al.*, 2010; Strogen *et al.*, 2017; Fig. 4). As the subduction of the Pacific Plate initiated east of the Taranaki Basin, extension was followed by compression during the Eocene-Miocene (*e.g.* Reilly *et al.*, 2015). Finally, the Taranaki Basin has developed as a back-arc rift during the Plio-Pleistocene, with dominant NE-SW and NNE-SSW faulting, and minor N-S and NW-SE faults thought to be inherited structures of the Late Cretaceous-Paleocene rift (Giba *et al.*, 2010; Giba *et al.*, 2012). Although the major basin-bounding faults of the Taranaki Basin appear to follow the boundaries between deep basement terranes (Muir *et al.*, 2000), the influence of basement fabrics on the development of distinct normal faults has been poorly investigated. Thanks to its location on the uplifted margin of the Taranaki Basin, our study area presents excellent imaging of the intrabasement structures and a weakly-deformed, stratigraphically flat sedimentary succession, making it an ideal location to examine the early-stage interactions between intra-basement structures and the overlying Plio-Pleistocene normal faults.

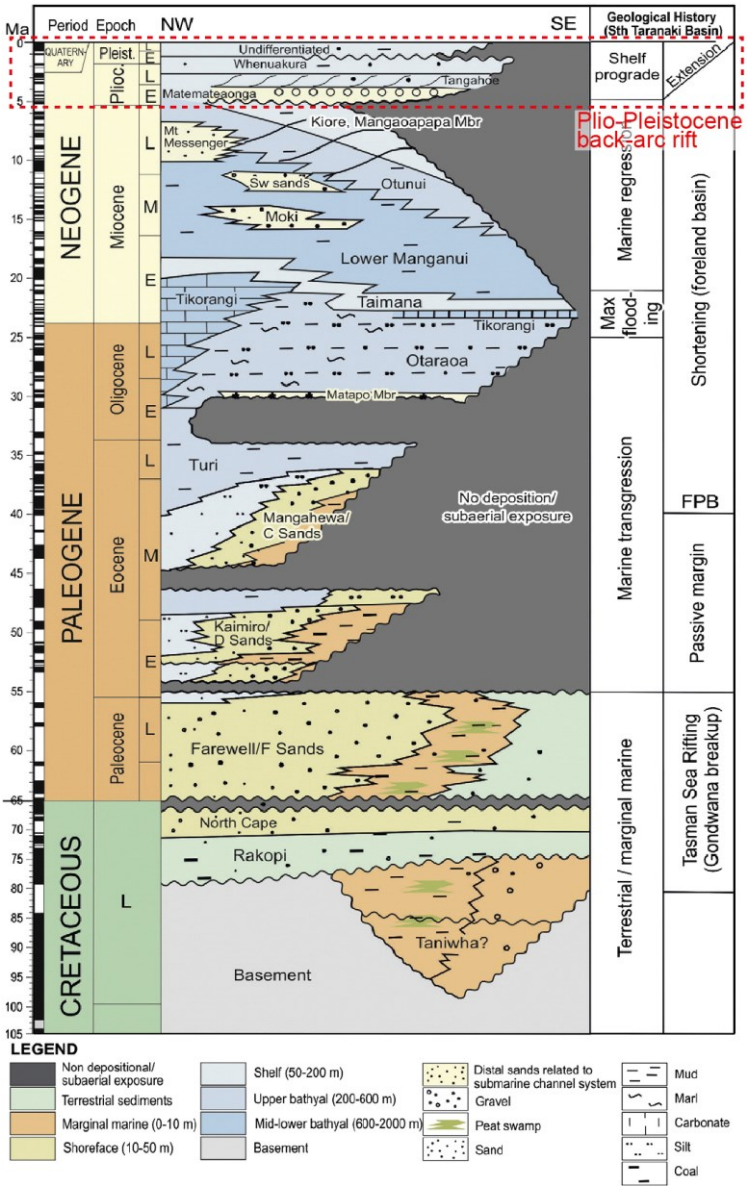

Fig. 4. Schematic diagram of the tectonic evolution of the Taranaki Basin. Note the Plio-Pleistocene back-arc rifting, which is the focus of the present thesis (modified after Reilly *et al.*, 2015).

3. Aims of the PhD project

In this thesis, I used 3D seismic data to map and reconstruct the activity phases of complex fault patterns, finding evidence of polymodal faulting. Then, I used analogue models and kinematic analysis to investigate the role of 3D strain fields and the influence by intra-basement fabrics in the development of polymodal fault systems (Fig. 5).

Following this workflow, my PhD project aims to answer these interconnected questions:

- Can polymodal faulting occur at the regional scale, representing an alternative explanation to multiple rotations of the regional stress fields (**Paper 1**, **Paper 3**)?
- Which are the key-conditions for the onset of three-dimensional deformation? (**Paper 1**) And how do normal faults develop in 3D strain fields (**Paper 2**)?
- How do basement fabrics influence the development of normal faults in the overlying sedimentary cover (**Paper 3**)?

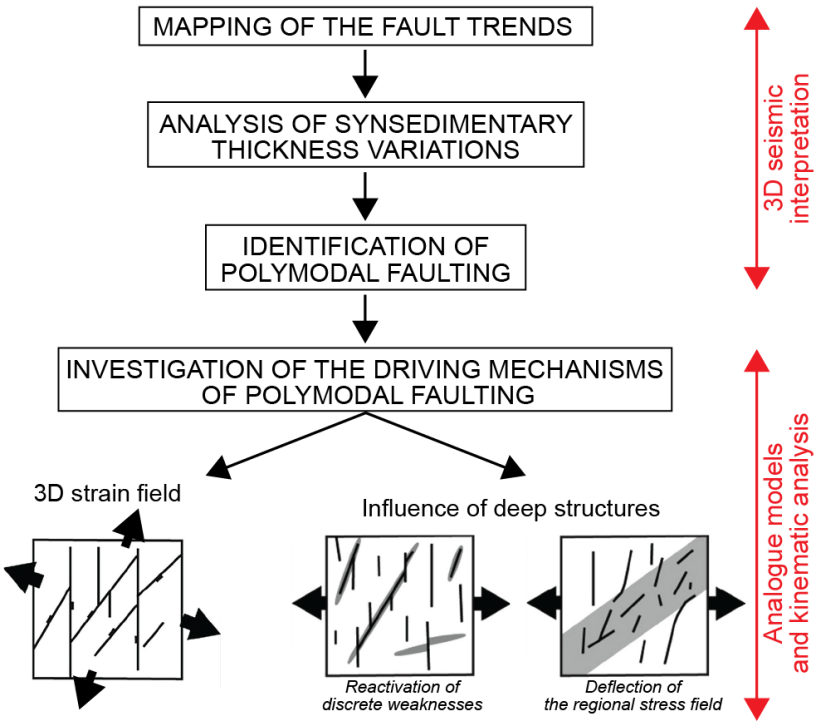

Fig. 5. Workflow of the PhD project (sketches of polymodal faulting modified after Reeve *et al.*, 2015).

The research outcomes of my PhD project are presented in the form of three papers:

PAPER 1. The onset of N-Atlantic rifting in the Hoop Fault Complex (SW Barents Sea): An orthorhombic dominated faulting?

This study presents a 3D seismic-based structural analysis of the Late Mesozoic-Cenozoic rifting in the Hoop Fault Complex. We use time-thickness maps to constrain the activity range of the various fault systems and compare the fault patterns at different levels to test the influence of deep Carboniferous-Permian structures. During the early stage of the rift, WNW-ESE- and NNE-SSW-striking normal faults appear to be simultaneously active, with across-fault thickness variations indicating their coeval synsedimentary activity. Further, these two nearly orthogonal fault systems present similar spatial distribution and vertical extent, consisting of tens of closely spaced (1-2 km) faults vanishing in the Triassic clay-rich succession. As rifting progressed, deformation localised on a major graben/half-graben system, with the activation of a NE-SW half-graben followed by the activation of a N-S graben at its northern tip. This graben/half-graben system crosscuts the Triassic succession, with the NE-SW half-graben clearly dislocating the Carboniferous-Permian succession. Following the activation of the graben/half-graben, only the NNE-SSW fault system remained extensionally active, whilst no thickness variations can be observed across the WNW-ESE faults.

As the WNW-ESE and NNE-SSW fault sets appear completely detached from deep structures, we interpret them as conjugate sets of an orthorhombic system accommodating a 3D strain field, according to the model of Reches (1978). The transition from well-distributed orthorhombic faulting to a localised graben/half-graben system indicates the focussing of the extension along a specific direction, which may reflect the progressive northward opening of the Atlantic. Alternatively, the strain field evolution may be driven by the localisation of deformation on deep structures of the late Carboniferous-Permian rift, followed by upward propagation. This work highlights the importance of both the tectonic setting and the rheological layering of the sedimentary succession in the development of a 3D strain field. On the one hand, the interaction between the Atlantic and the Arctic rifts appears to be key to the onset of a 3D strain field, as indicated by the cessation of polymodal faulting when the Atlantic rift became dominant. On the other hand, the presence of a thick clay-rich succession retarded the influence of deep fabrics over the upper part of the succession, preventing the localisation of the deformation on pre-existing structures during the early stage of the rift.

PAPER 2. The role of fault interactions in 3D strain fields

This study is the direct sequel of Paper 1, presenting an analysis of the development of faults in 3D strain fields based on analogue models. By simple, brittle-ductile, gravity-driven models, we reproduced isotropic radial extension and synchronous bidirectional extension along two perpendicular directions. Isotropic radial extension resulted in the development of a polygonal fault pattern, with faults generally intersecting at high angles (90°-120°). Curvilinear faults typically intersect minor straight faults in their points of maximum curvature, simulating triple junctions. The curvilinear and the straight faults developed simultaneously as a coupled system, indicating an anisotropic strain field with a preferential extension direction approximately perpendicular to the curvilinear faults. In contrast, the global strain field remains symmetric and stable during the whole experiment, suggesting that the anisotropic strain fields associated to individual faults compensate each other. When two perpendicular extension directions are applied to the model, two fault systems developed perpendicularly to each extension direction, forming characteristic T-shaped and L-shaped intersections. The developments of the two fault systems seem largely interrelated, with the growth of a fault along a given direction generally followed by the nucleation of a new perpendicular fault at a short distance. This interaction between adjacent faults is likely related to the stress drop due to the activity of a fault, which hinders the nucleation and propagation of parallel faults within its stress shadow zone but does not affect perpendicular faults.

Our analogue models display a clear similarity to natural examples with (i) the model of radial extension reproducing the curvilinear fault patterns of the Afar triple junction and (ii) the model of synchronous bidirectional extension reproducing the characteristic intersection style of the Hoop Fault Complex, characterised by T-shaped and L-shaped intersections. These similarities suggest that tectonic settings under the simultaneous influence of different rift systems are prone to the onset of 3D strain fields, whose symmetry appear to reflect the number and the geometry of the intersecting rift systems. Despite the stability of the global strain field, the local strain field may be extremely variable spatially and temporally, with local interactions between faults exerting a primary control on the development of faults and, thus, on the final fault pattern.

PAPER 3. How do intra-basement fabrics influence normal fault growth? Insights from the Taranaki Basin, offshore New Zealand

As in Paper 1, we used the 3D seismic-based structural analysis to perform the study of the Plio-Pleistocene rifting in the Taranaki Basin. Although the majority of the faults follow the regional NE-SW/NNE-SSW trend, there are also oblique fault segments with strikes ranging between NW-SE and N-S. All the rift-oblique and some rift-parallel normal faults correlate with the underlying intra-basement fabrics, which are interpreted as Mesozoic shear zones. However, there is no evidence of extensional reactivation of the latter, which generally display reverse throw at the top basement level. In order to investigate these enigmatic relationships between intra-basement fabrics and normal faults, we performed 3D kinematic analysis on selected fault planes.

Normal faults physically connected to intra-basement fabrics generally display an area of reverse throw immediately above the top of the crystalline basement, passing sharply to elongated throw maxima. This throw distribution suggests that intra-basement fabrics were reactivated during the Miocene compression, propagating upwards as reverse structures, which later offered preferential nucleation sites for normal faults during the Plio-Pleistocene rifting. Among the normal faults oblique to the Plio-Pleistocene trend, only the normal faults connected to km-wide intrabasement structures propagated to the upper part of the sedimentary cover. The upward propagation of these normal faults may be favoured by local perturbations of the regional stress field arising above km-wide intra-basement structures; this is supported also by nucleation of fault segments striking oblique to the regional trend of the rift but parallel to the deep intra-basement structures at a distance of ca. 1500 m above the top of the basement. Our study demonstrates that (i) intrabasement fabrics can influence normal faults without being extensionally reactivated and (ii) preferential nucleation from pre-existing weaknesses and local perturbation of the stress field may strongly influence the development of normal faults, leading to polymodal faulting.

References

Anderson, E.M., 1951. The Dynamics of Faulting. Oliver and Boyd, London, (183 pp.).

Aydin, A., Reches, Z., 1982. Number and orientation of fault sets in the field and in experiments. Geology 10, 107. https://doi.org/10.1130/0091-7613(1982)10<107:NAOOFS>2.0.CO;2

Bartholomew, I.D., Peters, J.M., Powell, C.M., 1993. Regional structural evolution of the North Sea: oblique slip and the reactivation of basement lineaments. Petroleum Geology Conference Series 4, Geological Society, London, 1109-1122

Bellahsen, N., Husson, L., Autin, J., Leroy, S., d'Acremont, E., 2013. The effect of thermal weakening and buoyancy forces on rift localization: Field evidences from the Gulf of Aden oblique rifting. Tectonophysics 607, 80–97. https://doi.org/10.1016/j.tecto.2013.05.042

Bird, P.C., Cartwright, J.A., Davies, T.L., 2015. Basement reactivation in the development of rift basins: an example of reactivated Caledonide structures in the West Orkney Basin. Journal of the Geological Society 172, 77–85. https://doi.org/10.1144/jgs2013-098

Bistacchi, A., Massironi, M., 2000. Post-nappe brittle tectonics and kinematic evolution of the north-western Alps: an integrated approach. Tectonophysics 327, 267–292. https://doi.org/10.1016/S0040-1951(00)00206-7

Cartwright, J.A., Lonergan, L., 1996. Volumetric contraction during the compaction of mudrocks: A mechanism for the development of regional-scale polygonal fault systems. Basin Research 8, 183–193. https://doi.org/10.1046/j.1365-2117.1996.01536.x

Destro, N., 1995. Release fault: A variety of cross fault in linked extensional fault systems, in the Sergipe-Alagoas Basin, NE Brazil. Journal of Structural Geology 17, 615–629. https://doi.org/10.1016/0191-8141(94)00088-H

Duffy, O.B., Bell, R.E., Jackson, C.A.-L., Gawthorpe, R.L., Whipp, P.S., 2015. Fault growth and interactions in a multiphase rift fault network: Horda Platform, Norwegian North Sea. Journal of Structural Geology 80, 99–119. https://doi.org/10.1016/j.jsg.2015.08.015

Faleide, J.I., Tsikalas, F., Breivik, A.J., Mjelde, R., Ritzmann, O., Engen, Ø., Wilson, J., Eldholm, O., 2008. Structure and evolution of the continental margin off Norway and the Barents Sea. Episodes 31, 82–91.

Faleide, J.I., Vågnes, E., Gudlaugsson, S.T., 1993. Late Mesozoic-Cenozoic evolution of the south-western Barents Sea in a regional rift-shear tectonic setting. Marine and Petroleum Geology 10, 186–214. https://doi.org/10.1016/0264-8172(93)90104-Z

Franceschi, M., Massironi, M., Franceschi, P., Picotti, V., 2014. Spatial analysis of thickness variability applied to an Early Jurassic carbonate platform in the central Southern Alps

(Italy): a tool to unravel syn-sedimentary faulting. Terra Nova 26, 239–246. https://doi.org/10.1111/ter.12092

Gabrielsen, R.H., Færseth, R.B., Jensen, L.N., Kalheim, J.E., Riis, F., 1990. Structural elements of the Norwegian continental shelf, Part I: The Barents Sea Region, Norwegian Petroleum Directorate Bulletin 6, (33 pp.).

Gawthorpe, R.L., Leeder, M.R., 2008. Tectono-sedimentary evolution of active extensional basins. Basin Research 12, 195–218. https://doi.org/10.1111/j.1365-2117.2000.00121.x

Gernigon, L., Brönner, M., Roberts, D., Olesen, O., Nasuti, A., Yamasaki, T., 2014. Crustal and basin evolution of the southwestern Barents Sea: From Caledonian orogeny to continental breakup: Evolution of the Barents Sea. Tectonics 33, 347–373. https://doi.org/10.1002/2013TC003439

Giba, M., Nicol, A., Walsh, J.J., 2010. Evolution of faulting and volcanism in a back-arc basin and its implications for subduction processes: TARANAKI BASIN EVOLUTION. Tectonics 29, n/a-n/a. https://doi.org/10.1029/2009TC002634

Giba, M., Walsh, J.J., Nicol, A., 2012. Segmentation and growth of an obliquely reactivated normal fault. Journal of Structural Geology 39, 253–267. https://doi.org/10.1016/j.jsg.2012.01.004

Glørstad-Clark, E., Birkeland, E.P., Nystuen, J.P., Faleide, J.I., Midtkandal, I., 2011. Triassic platform-margin deltas in the western Barents Sea. Marine and Petroleum Geology 28, 1294–1314. doi:10.1016/j.marpetgeo.2011.03.006

Glørstad-Clark, E., Faleide, J.I., Lundschien, B.A., Nystuen, J.P., 2010. Triassic seismic sequence stratigraphy and paleogeography of the western Barents Sea area. Marine and Petroleum Geology 27, 1448–1475. doi:10.1016/j.marpetgeo.2010.02.008

Gudlaugsson, S.T., Faleide, J.I., Johansen, S.E., Breivik, A.J., 1998. Late Palaeozoic structural development of the South-western Barents Sea. Marine and Petroleum Geology 15, 73–102. doi:10.1016/S0264-8172(97)00048-2

Gupta, A., Scholz, C.H., 2000. A model of normal fault interaction based on observations and theory. Journal of Structural Geology 22, 865–879. https://doi.org/10.1016/S0191-8141(00)00011-0

Healy, D., Blenkinsop, T.G., Timms, N.E., Meredith, P.G., Mitchell, T.M., Cooke, M.L., 2015. Polymodal faulting: Time for a new angle on shear failure. Journal of Structural Geology 80, 57–71. https://doi.org/10.1016/j.jsg.2015.08.013

Healy, D., Jones, R.R., Holdsworth, R.E., 2006. Three-dimensional brittle shear fracturing by

tensile crack interaction. Nature 439, 64–67. https://doi.org/10.1038/nature04346

Krantz, R.W., 1988. Multiple fault sets and three-dimensional strain: Theory and application. Journal of Structural Geology 10, 225–237. https://doi.org/10.1016/0191-8141(88)90056-9

Maerten, L., Gillespie, P., Pollard, D.D., 2002. Effects of local stress perturbation on secondary fault development. Journal of Structural Geology 24, 145–153. https://doi.org/10.1016/S0191-8141(01)00054-2

Miller, J.M., Nelson, E.P., Hitzman, M., Muccilli, P., Hall, W.D.M., 2007. Orthorhombic fault–fracture patterns and non-plane strain in a synthetic transfer zone during rifting: Lennard shelf, Canning basin, Western Australia. Journal of Structural Geology 29, 1002–1021. https://doi.org/10.1016/j.jsg.2007.01.004

Morley, C.K., 2010. Stress re-orientation along zones of weak fabrics in rifts: An explanation for pure extension in 'oblique' rift segments? Earth and Planetary Science Letters 297, 667–673. https://doi.org/10.1016/j.epsl.2010.07.022

Morley, C.K., Haranya, C., Phoosongsee, W., Pongwapee, S., Kornsawan, A., Wonganan, N., 2004. Activation of rift oblique and rift parallel pre-existing fabrics during extension and their effect on deformation style: examples from the rifts of Thailand. Journal of Structural Geology 26, 1803–1829. https://doi.org/10.1016/j.jsg.2004.02.014

Muir, R.J., Bradshaw, J.D., Weaver, S.D., Laird, M.G., 2000. The influence of basement structure on the evolution of the Taranaki Basin, New Zealand. Journal of the Geological Society 157, 1179–1185. https://doi.org/10.1144/jgs.157.6.1179

Phillips, T.B., Jackson, C.A.-L., Bell, R.E., Duffy, O.B., Fossen, H., 2016. Reactivation of intrabasement structures during rifting: A case study from offshore southern Norway. Journal of Structural Geology 91, 54–73. https://doi.org/10.1016/j.jsg.2016.08.008

Reches, Z., 1978. Analysis of faulting in three-dimensional strain field. Tectonophysics 47, 109–129. https://doi.org/10.1016/0040-1951(78)90154-3

Reches, Z., Dieterich, J.H., 1983. Faulting of rocks in three-dimensional strain fields I. Failure of rocks in polyaxial, servo-control experiments. Tectonophysics 95, 111–132. https://doi.org/10.1016/0040-1951(83)90263-9

Reeve, M.T., Bell, R.E., Duffy, O.B., Jackson, C.A.-L., Sansom, E., 2015. The growth of non-colinear normal fault systems; What can we learn from 3D seismic reflection data? Journal of Structural Geology 70, 141–155. https://doi.org/10.1016/j.jsg.2014.11.007

Reeve, M.T., Bell, R.E., Jackson, C.A.-L., 2014. Origin and significance of intra-basement seismic

reflections offshore western Norway. Journal of the Geological Society 171, 1–4. https://doi.org/10.1144/jgs2013-020

Reilly, C., Nicol, A., Walsh, J.J., Seebeck, H., 2015. Evolution of faulting and plate boundary deformation in the Southern Taranaki Basin, New Zealand. Tectonophysics 651–652, 1–18. https://doi.org/10.1016/j.tecto.2015.02.009

Ring, U., 1994. The influence of preexisting structure on the evolution of the Cenozoic Malawi rift (East African rift system). Tectonics 13, 313–326. https://doi.org/10.1029/93TC03188

Serck, C.S., Faleide, J.I., Braathen, A., Kjølhamar, B., Escalona, A., 2017. Jurassic to Early Cretaceous basin configuration(s) in the Fingerdjupet Subbasin, SW Barents Sea. Marine and Petroleum Geology 86, 874–891. https://doi.org/10.1016/j.marpetgeo.2017.06.044

Stewart, S.A., 2001. Displacement distributions on extensional faults: Implications for fault stretch, linkage, and seal. AAPG Bulletin 85, 587–599.

Stewart, S.A., Clark, J.A., 1999. Impact of salt on the structure of the Central North Sea hydrocarbon fairways, in: Petroleum Geology of Northwest Europe: Proceedings of the 5th Conference. Geological Society of London, pp. 179–200. https://doi.org/10.1144/0050179

Strogen, D.P., Seebeck, H., Nicol, A., King, P.R., 2017. Two-phase Cretaceous–Paleocene rifting in the Taranaki Basin region, New Zealand; implications for Gondwana break-up. Journal of the Geological Society 174, 929–946. https://doi.org/10.1144/jgs2016-160

Trudgill, B.D., 2002. Structural controls on drainage development in the Canyonlands grabens of southeast Utah. AAPG Bulletin 86, 1095–1112.

Whipp, P.S., Jackson, C.A.-L., Gawthorpe, R.L., Dreyer, T., Quinn, D., 2014. Normal fault array evolution above a reactivated rift fabric; a subsurface example from the northern Horda Platform, Norwegian North Sea. Basin Research 26, 523–549. https://doi.org/10.1111/bre.12050

Younes, A.I., McClay, K., 2002. Development of accomodation zones in the gulf of Suez-Red Sea rift, Egypt. AAPG Bulletin 86, 1003–1026.

PAPER 1

Submitted to *Tectonophysics* 11 August 2016, received in revised form 30 March 2017, accepted 3 April 2017, available online 4 April 2017

ONSET OF N-ATLANTIC RIFTING IN THE HOOP FAULT COMPLEX (SW BARENTS SEA): AN ORTHORHOMBIC DOMINATED FAULTING?

Luca Collanega[1], Matteo Massironi[1], Anna Breda[1], Bent Erlend Kjølhamar[2]

[1] Dipartimento di Geoscienze, University of Padova, Via G.Gradenigo, 6 - 35131 Padova, Italy

[2] TGS, Lensmannslia 4, 1386 Asker, Norway

Corresponding author: luca.collanega@gmail.com

Tectonophysics 706-707 (2017) 59-70, http://dx.doi.org/10.1016/j.tecto.2017.04.003

Luca Collanega did the entire seismic interpretation work, wrote the first version of the manuscript and drafted all the figures. Matteo Massironi and Anna Breda designed the general structure of the paper, inspired discussions and edited the final manuscript. Bent Erlend Kjølhamar contributed to calibrate the stratigraphy and gave important clues on the regional geology of the study area.

ABSTRACT

The Hoop Fault Complex is one of the main faults systems in the south-western Barents Sea. This platform underwent a long extensional history under the influence of both the Atlantic and the Arctic rifts, which culminated in the Atlantic break-up in the Cenozoic. The object of this paper is the structural analysis of the late Mesozoic rifting in the Hoop Fault Complex area, based on a 10.000 km^2 3D seismic volume.

We constrained the intervals of activity of the main faults systems during the late Mesozoic rifting through the synsedimentary thickness variations, reconstructing the evolution of the strain field. In order to clarify the relationship between the strain field and the rheological layering, we compared the structures at different depths, highlighting a decoupling of shallow and deep deformations along the Triassic ductile clay-rich layers.

A transition from an orthorhombic faulting, corresponding to a 3D strain field, to an Andersonian faulting, related to a planar strain field, was observed. The change of the strain field could be driven by the evolution of the regional stress field or, alternatively, by the reactivation of deep structures. In this latter case, the structural evolution of the Hoop Fault Complex could potentially represent a general process to be extended to other rifting settings with a similar mechanical stratigraphy.

1. Introduction

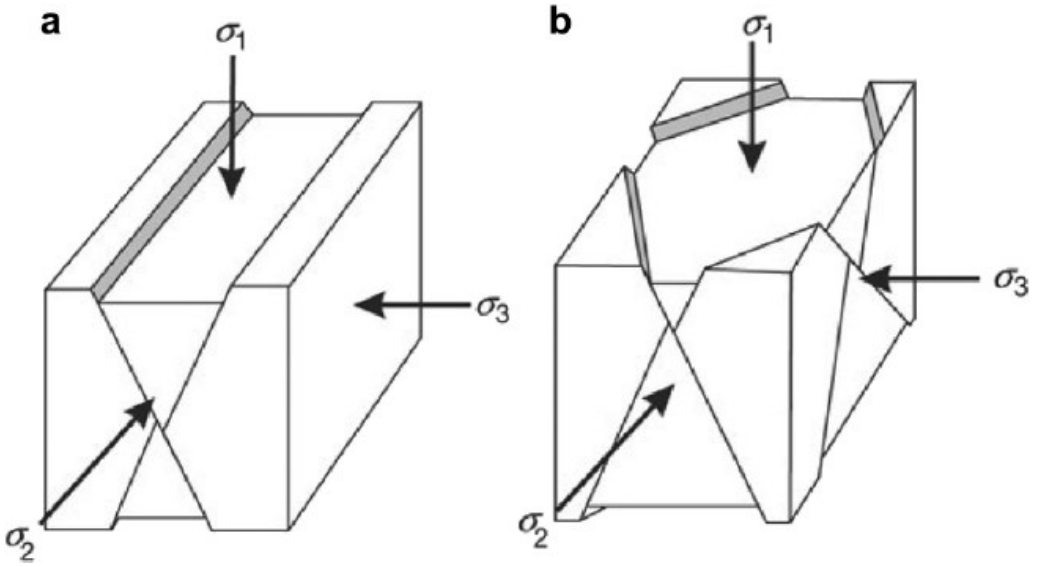

Fig. 1. (a) Andersonian fault pattern and the associated stress field (Anderson, 1951); (b) orthorhombic fault pattern and the associated stress field according to Reches (1978) (modified after Healy *et al*., 2006).

Orthorhombic fault systems consist of four sets of faults developed simultaneously in a rhomboidal pattern (Fig. 1) (Reches, 1978). The robust theoretical analysis of Reches (Reches, 1978; 1983; Reches and Dieterich, 1983) and Krantz (Krantz, 1988) pointed out that this fault arrangement is required to accommodate a three-dimensional deformation, where none of the principal strains equals zero ($\varepsilon_1, \varepsilon_2, \varepsilon_3 \neq 0$) (see Supplementary materials for more details on the model of Reches). Given the 3D nature of the crust, a 3D strain is expected to be more common than planar strain (Healy *et al*., 2015), however few examples of orthorhombic systems have been described in recent years. This is possibly due to the difficulty of proving the simultaneous activity of different fault trends. Nevertheless, orthorhombic patterns have been described at different scales: hundreds of meters (Aydin and Reches, 1982; Carvell *et al.,* 2014), kilometers (Krantz, 1988; Miller *et al.,* 2007), tens of kilometers (Franceschi *et al*., 2014). All the previously cited examples of orthorhombic systems have been described in extensional settings, suggesting a connection between these fault arrangements and extensional domains.

In this work, an orthorhombic fault system has been observed and analyzed in an area of 10.000 km^2 across the Hoop Fault Complex (SW Barents Sea), one of the major fault zones of the Barents Shelf, which marked the transition between the stable Bjarmeland Platform (to the east) and the basinal province (to the west) during the late Mesozoic-Cenozoic rifting (Fig. 2). Thanks to the location at the transition between stable and highly subsiding areas, the sedimentary succession corresponding to the initial phase of the rift is at very shallow depth, assuring excellent seismic

resolution. Furthermore, the Hoop Fault Complex is an old zone of weakness, affecting a sequence characterized by units with different rheological properties (Glørstad-Clark *et al.*, 2010). Hence, it has been possible to study the influence of rheological layering and reactivation processes on the nucleation of orthorhombic systems.

The imaging of the structures at different levels of the stratified succession allowed for the comparison between shallow and deep deformations. In addition, we were able to define the relative activation order of the various fault systems of the late Mesozoic-Cenozoic rifting thanks to synsedimentary thickness variations highlighted in time-thickness maps. Hence, 3D seismics enabled us to address the activity of the orthorhombic system in the tectonic framework of the Barents Sea.

The development of an orthorhombic system in the Hoop Fault Complex has been seen in the light of the overall late Mesozoic structural architecture of basins and highs of the Barents Shelf, which largely reflects Caledonian weakness zones of the basement (Gernigon *et al.*, 2014). Further, we addressed the relationship between orthorhombic faulting and the specific tectonic framework of the Barents Sea, characterized by the interaction between the Atlantic and the Arctic rifts, as well as the possible significance of this system in terms of general processes occurring during rifting. Indeed, the specific rheological layering of the Barents Sea succession and the amazing imaging possibilities disclosed by 3D seismic could highlight processes difficult to appreciate in other settings. In summary, this work addresses the following interconnected questions about orthorhombic fault systems in a rift tectonic setting:

(a) Why an orthorhombic regime might develop within opening rifts despite a pre-existing buried architecture?

(b) What is the key criterion in terms of rheological stratigraphy that leads to such a development?

(c) Which is the regional tectonism that might favour evolutions between 3D and planar strain regimes?

2. Geological framework

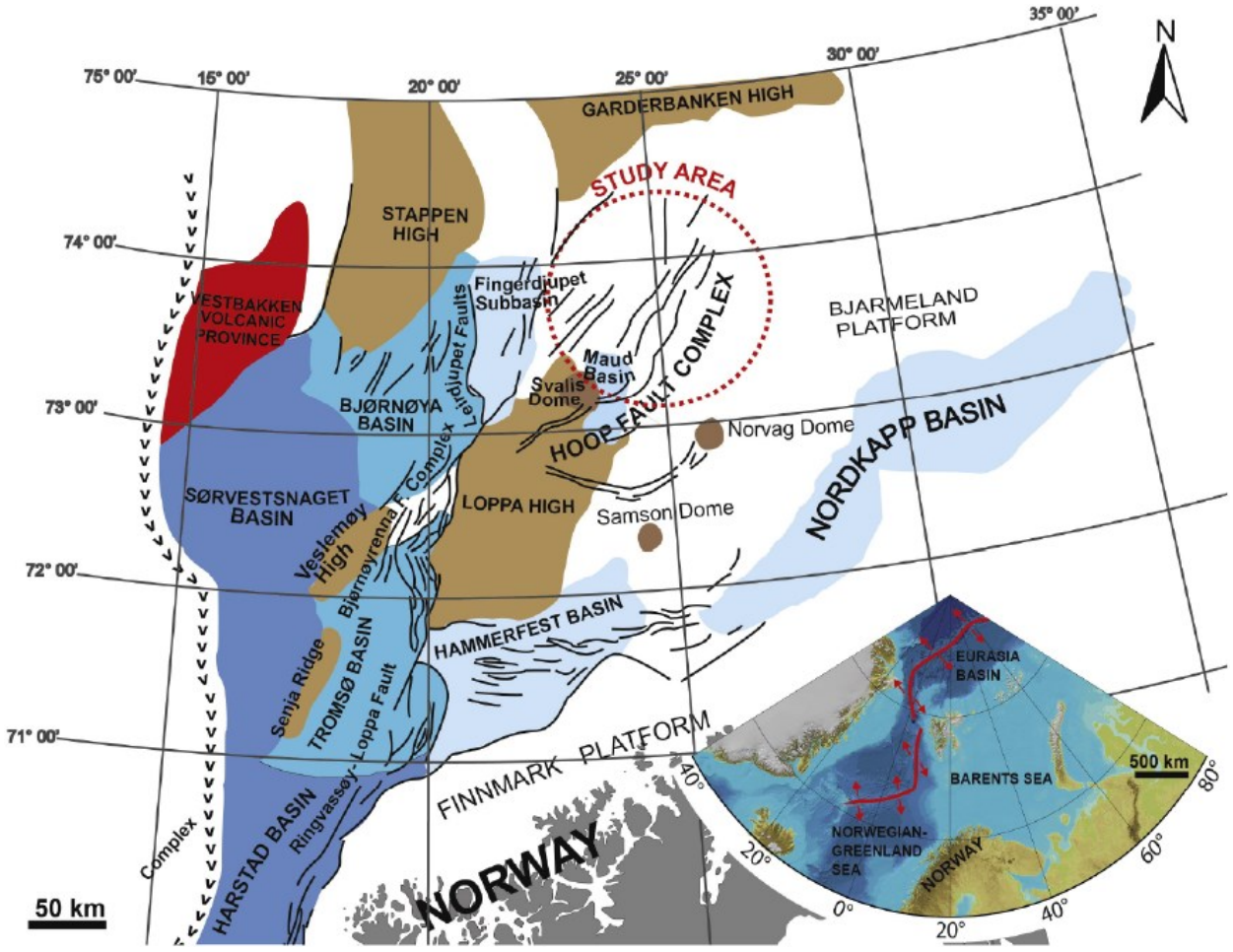

Fig. 2. Main structural elements and faults complexes of the late Mesozoic-Cenozoic rift in the south-western Barents Sea (modified after Gabrielsen *et al*. 1990). Red = volcanic province; brown = structural highs; blue = structural lows (the darkest the deepest); white = stable platform; V = continental margin. The red circle indicates approximately the study area of this work. The inset shows the geodynamic setting of the Barents Sea. Base map from Jakobsson *et al.* (2012).

The tectonic history of the western Barents Sea is largely related to the Caledonian and Uralian orogenesis and to the subsequent rifting and opening of the Atlantic and Arctic oceans (Doré, 1991; Faleide *et al*., 1993; Tsikalas *et al.*, 2012). The Caledonian orogeny, resulting from the collision of Baltica and Laurentia (culminated 400 Ma), largely controlled the basement structural grain underneath the sedimentary cover of the western Barents Sea (Gernigon *et al.*, 2014). After this compressional phase, the tectonic evolution of the Barents Sea was characterized by prevalent extensional tectonics.

The first major rifting event that affected the Barents Shelf occurred between the Middle Carboniferous and the Lower Permian (Gudlaugsson *et al.*, 1998). During this event, the Barents Platform developed its characteristic structural configuration, consisting of a fan-shaped array of

basins and highs controlled by anisotropies inherited from the structural grain of the Caledonides (Gudlaugsson *et al.*, 1998). The Carboniferous rift structures strongly controlled the pattern of sedimentation during the Permian, as indicated by the development of carbonate buildups at the basin margins and intra-basinal highs and by the deposition of evaporites within the basins (Gudlaugsson *et al.*, 1998). The salt was remobilized during successive periods of tectonic activity; in particular, along the Hoop Fault Complex, salt remobilization led to the development of the Svalis Dome and the Maud Basin during the Early to Middle Triassic (Gabrielsen *et al*., 1990). The fault-controlled subsidence in the Middle Carboniferous-Lower Permian was followed by regional subsidence in the Upper Permian and Triassic (Gudlaugsson *et al*., 1998). During Triassic, large volumes of sediments were deposited by alluvial-deltaic prograding systems with the major provenance areas located to the east and south-east, mainly sourced by the Uralides orogen (Worsley, 2008; Glørstad-Clark *et al.*, 2010), reaching thicknesses at places exceeding 2000 m.

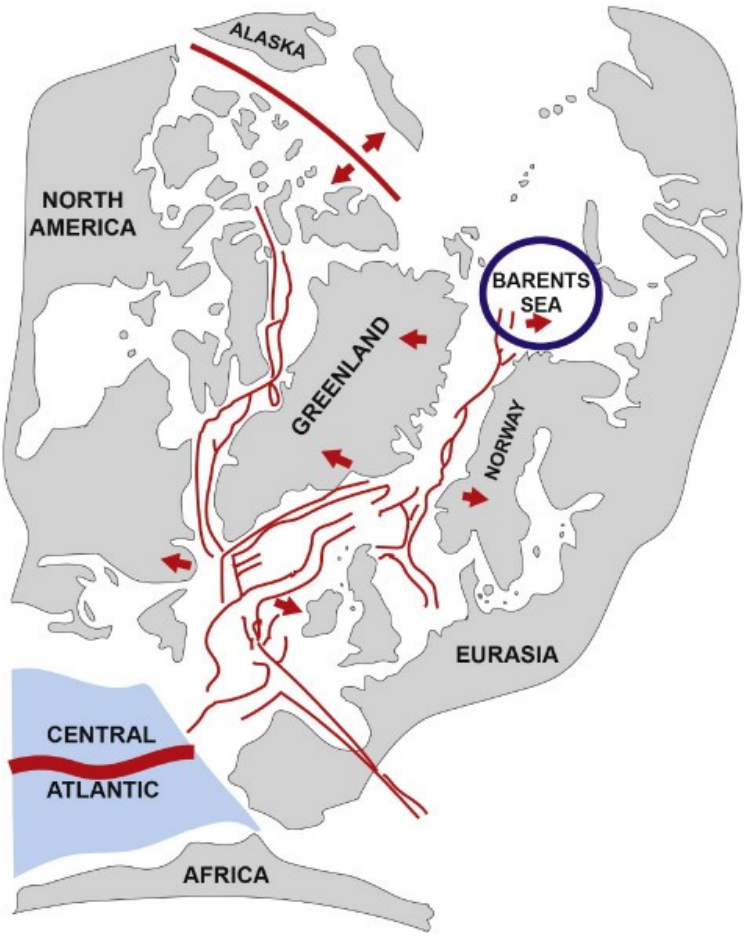

Fig. 3 Palinspastic reconstruction showing the location of the Barents Sea at the onset of the late Mesozoic rifting. Thick red line = Atlantic ridge; thin red lines = main faults of the Atlantic and the Arctic rifts; red arrows = extension directions; blue shading = Atlantic oceanic crust (modified after Faleide *et al*., 1993).

The sedimentation was characterized by predominant deposition of clays, locally rich in organic matter, with secondary silt and sand intervals (Dalland *et al.*, 1988). In the Lower-Middle Jurassic, a shallow marine environment was established, leading to the deposition of prevailing sandy units (Faleide *et al.*, 2008).

In the late Mesozoic-early Cenozoic, the progressive northward spreading of the Central Atlantic (Dorè *et al*., 1999) and the incipient opening of the Arctic led to the other major rifting event in the Barents history (Fig. 3) (Faleide *et al*., 1993). The structuring during this rifting event was largely controlled by the reactivation of deep fault systems inherited from late Paleozoic times (Faleide *et al*., 1993). The earliest indications of a paleogeographic differentiation due to the rifting have been observed in the Middle Jurassic sedimentary succession of the Hammerfest Basin (Fig. 2) (Faleide *et al.*, 1993). In the Cretaceous, deep basins (Bjørnøya, Tromsø and Harstad Basins) developed west of the Bjarmeland Platform (Fig. 2) and finally, in the early Cenozoic, the tectonic activity focused along the present day oceanic margin, with the development of the Sørvestsnaget marginal basin (Fig. 2). Overall, the late Mesozoic-early Cenozoic rifting is characterized by a progressive westward shift of the tectonic activity (Faleide *et al.*, 1993). This change parallels a transition from oblique extension in the Middle Jurassic to a mega-shear setting in the Late Cretaceous and, finally, to a combined sheared-rifted continental margin at the break-up of the Norwegian-Greenland Sea in the early Cenozoic (Faleide *et al.*, 1993). The shear component is interpreted to reflect the interaction between the Atlantic and the Arctic rifts (Faleide *et al*., 1993) (Fig. 3). During plate separation, the margin developed a distinct segmentation and the passive margin stage was reached at different moments in different locations (Faleide *et al.*, 2008). Since the end of active rifting in the Oligocene, strong uplift and erosion affected the Barents platform (Faleide *et al.*, 2008).

The late Mesozoic-Cenozoic rifting resulted in fan-shaped array of basins and highs, with an increasing relief towards the margin, under the control of the late Paleozoic rift and the basement structures (Faleide *et al.,* 1993; Gernigon *et al*., 2014) (Fig. 2). In particular, a fault system (consisting of the Ringvassøy-Loppa Fault Complex, the Bjørnøyrenna Fault Complex and the Leirdjupet Fault Complex) marks the transition from the eastern Bjarmeland Platform, scarcely affected by the late Mesozoic-Cenozoic extension, to the Cretaceous deep basins (Fig. 2) (Gabrielsen *et al*., 1990). The Hoop Fault Complex parallels these fault systems and is connected to the Bjørnøyrenna Fault Complex through a series of *en echelon* minor grabens (Gabrielsen *et al.*, 1990). Faults activity in the Hoop area has been observed during the Carboniferous-Permian time and successively in the Middle Triassic, Late Jurassic-Early Cretaceous and possibly

Cenozoic (Gabrielsen *et al*., 1990). This implies an old weakness belt along the Hoop zone. In particular, a thickness increase and a change from plane-parallel seismic facies to clinoform geometries in the Triassic have been observed across the Hoop Fault Complex, suggesting a control on sedimentation by this fault system (Glørstad-Clark *et al.*, 2010).

3. Data and methods

Two adjacent migrated 3D datasets have been used: the HFC_MERGE, acquired by TGS in 2013, and the HFCE14, acquired by TGS in 2014. The HFC_MERGE was shot as a dual source with 8-10 streamers and a 100-75 m separation. It covers an area of about 7700 km^2 at a water depth of about 400 m along the Hoop Fault Complex. The bin spacing of the seismic cube is 18.75 X 12.5 m, the record length is 7100 ms TWT and the vertical sampling rate is 4 ms TWT. The HFCE14 covers an area of a 3400 km^2, east of the HFC_MERGE. This volume was shot as a dual source with 10 streamers and a 75 m separation; bin spacing, record length and vertical sampling rate are the same as in the HFC_MERGE.

The seismic interpretation is based on the workflow illustrated in Fig. 4. The starting point has been the lithostratigraphic interpretation based on the geological literature of the western Barents (e.g. Glørstad-Clark *et al.*, 2010; Glørstad-Clark *et al.*, 2011; Klausen *et al.*, 2016); following this, the main stratigraphic units (upper Paleozoic, Triassic, Jurassic, Cretaceous and Cenozoic packages) have been identified (Fig. 5). In the late Mesozoic interval, which is the focus of this paper, four horizons with good lateral continuity and corresponding to clear facies changes have been picked.

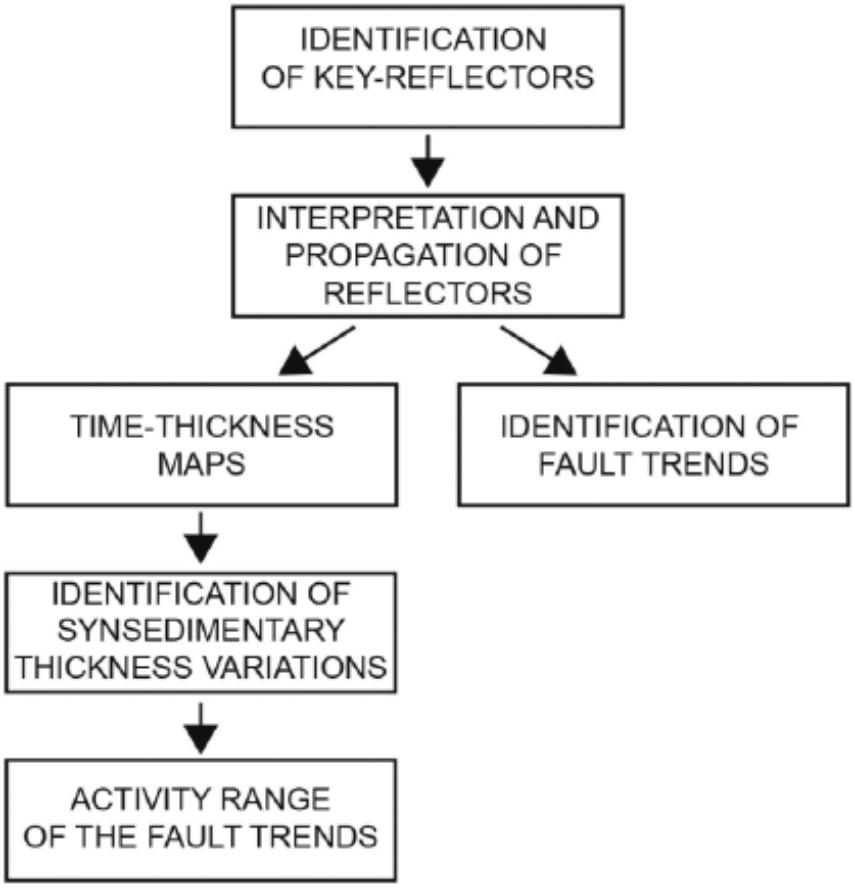

Fig. 4. Workflow of the seismic interpretation.

Since no detailed lithostratigraphic interpretation has been performed, the reflectors have been named in alphabetic order from the deepest to the shallowest one (Fig. 6):

Reflector A, the first interpretable positive event at the top of the weak Triassic reflectors (900-1250 ms);

Reflector B, the positive event located approximately in the middle of the package of strong Jurassic reflectors (850-1200 ms);

Reflector C, the positive event between the strong Jurassic and the weak Cretaceous reflectors (800-1100 ms);

Reflector D, the positive event at the top of the Cretaceous prograding system of northern provenance (650-950 ms).

Reflector B has been taken as reference to map the main fault trends in the study area, being a strong event, which can be accurately picked in seismic sections and effectively spread through the seismic volume, with ideal features to highlight the fault pattern (brittle behavior and position approximately in the middle of the Jurassic interval). This reflector has been mapped in the whole 3D acreage and the main faults have been traced in map view and described through rose diagrams elaborated in ArcGIS. Three time-thickness maps of the late Mesozoic package have been created through the subtraction of the 3D surfaces of adjacent horizons. The interval between Reflector A and Reflector B corresponds to the Nordmela Fm., which is characterised by claystone with minor sandstones deposited in tidal to estuarine channels during the lower Jurassic (Dalland *et al.*, 1988).

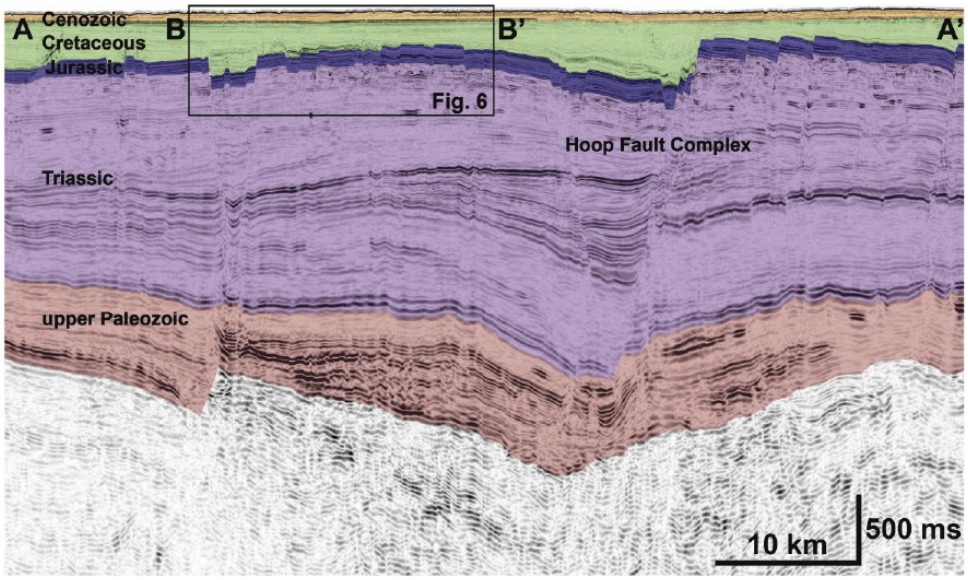

Fig. 5. Seismic section across the study area showing the main stratigraphic packages. Note the remarkable thickness of the Triassic interval and the regional unconformity at the base of the Cenozoic package. See Fig. 11 for the location of the seismic section.

The upper interval between reflectors B and C consists of the coastal sands of the Stø Fm. (Dalland *et al.*, 1988). Finally, the interval between Reflector C and D consists of large-scale southward prograding clinothems, which are related to the uplift of the northern margin of the Barents platform (Worsley, 2008). The time-thickness maps have been elaborated in three different areas that are representative of the main fault trends. Thickness variations across faults highlighted phases of synsedimentary activity and allowed us to define the relative activation order of the various systems in the study area.

The vertical extent and the geometries associated to each trend have been analyzed through seismic sections. Finally, the main faults have been mapped in the reflector at the top of the Carboniferous-Permian carbonates and evaporites in order to compare shallow and deep structures.

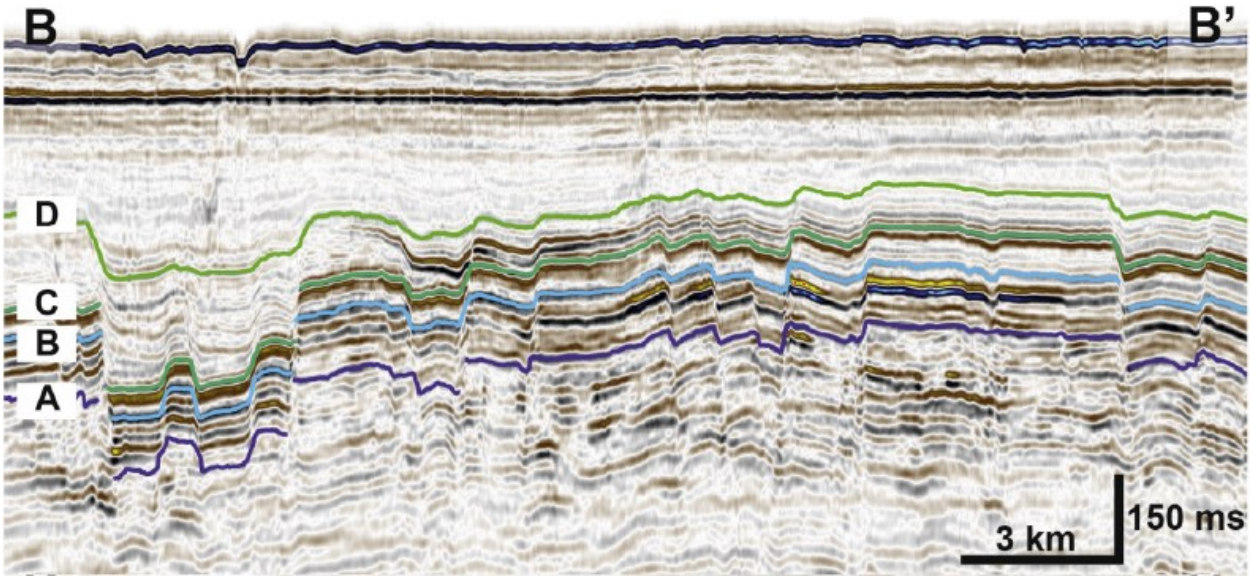

Fig. 6. The late Mesozoic-Cenozoic package (detail of Fig. 5) with the horizons picked and propagated in this work: Reflector A (dark blue), Reflector B (light blue), Reflector C (dark green) and Reflector D (light green). The reflectors delimit intervals with different seismic amplitude, lateral continuity and geometry. Note the package of strong reflectors, corresponding to the Jurassic interval, and the normal faults pertaining the late Mesozoic succession. See Fig. 11 for the location of the seismic section.

4. Results

Four mainly extensional fault systems have been recognized based on the trend in map view and the vertical extent: NE-SW, N-S, NNE-SSW and WNW-ESE (Fig. 7). The main structure observed is a NE-SW half-graben with downthrow to the NW, passing northwards to a N-S symmetric graben (Fig. 7). This half-graben/graben, which represents the northernmost segment of the Hoop Fault Complex, separates the Bjarmeland Platform (to the east) from a subsiding area transitional to the Fingerdjupet subbasin (to the west). To the south the throw of the NE-SW half-graben decreases approaching the Maud Basin, while to the north the N-S graben passes into a swarm of normal faults towards the Garderbanken High (Figs. 2; 7). In the western part of the survey, some major faults parallel this half-graben/graben system, with a NE-SW trend to the south and a NNW-SSE trend to the north. The other two main trends observed in the study area, the WNW-ESE and the NNE-SSW, are almost perpendicular to each other and define a system of small horsts and grabens, whose intersection define a series of alternating upthrown and downthrown rectangular blocks (Fig. 7).

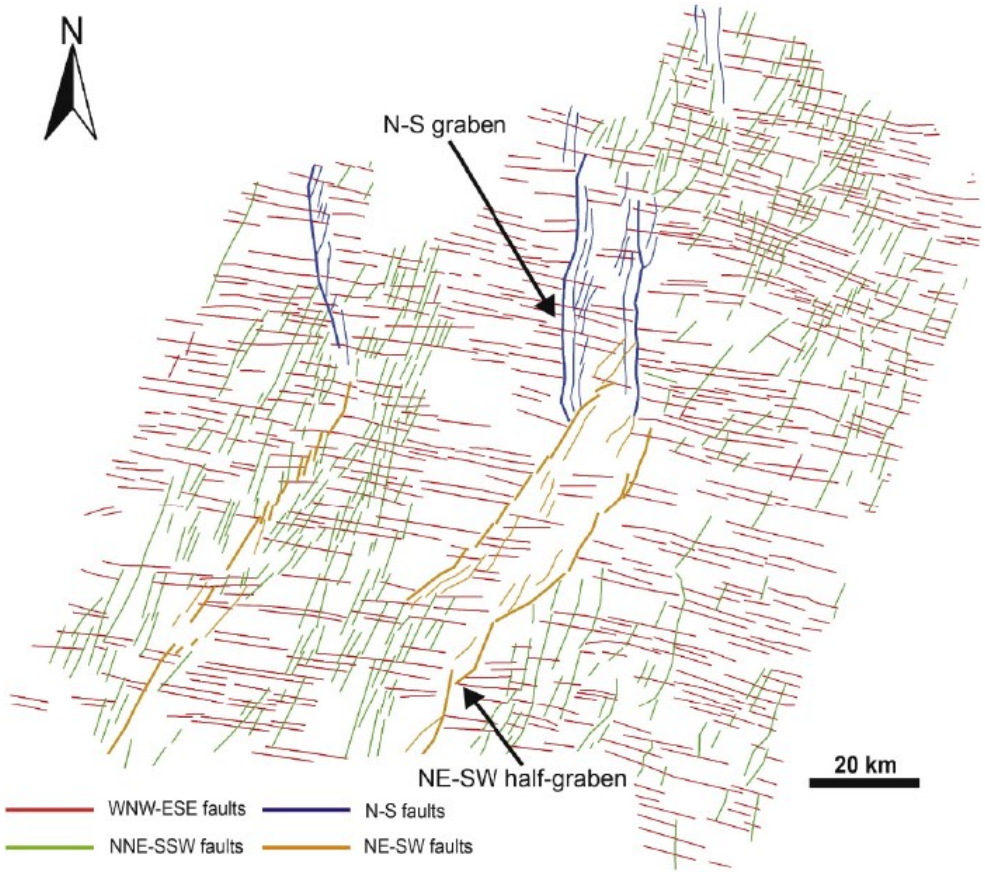

Fig. 7. Main fault systems active during the late Mesozoic-Cenozoic rifting in the Hoop Fault Complex. The fault systems were defined according to the trend in map view and the vertical extent.

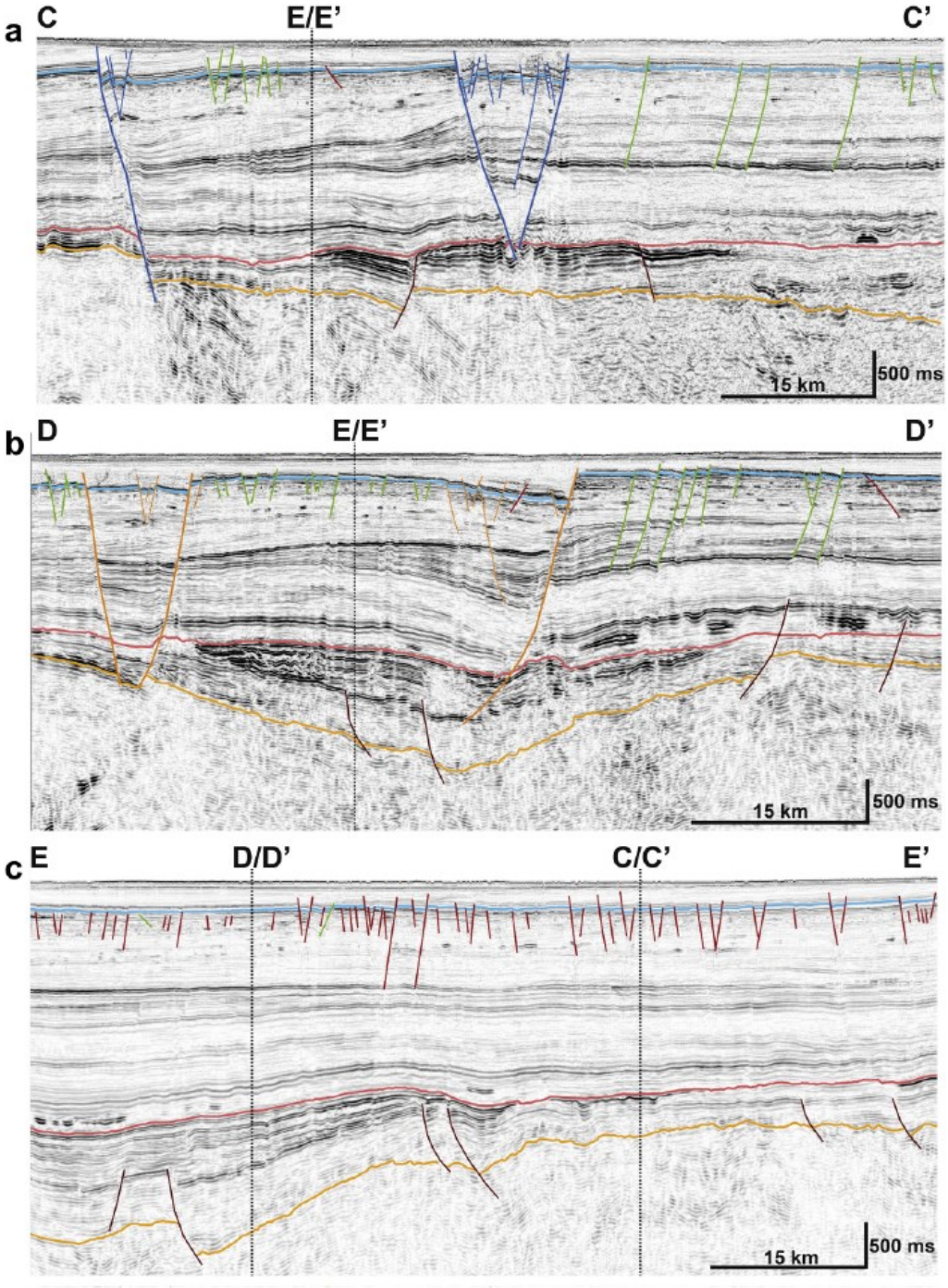

Fig. 8. Seismic sections across the main faults trends in the study area. Color legend as in Fig. 7, dark red segments highlight Carboniferous-Permian faults. Reference seismic reflectors have been traced: top of the basement (orange), top of Permo-Carboniferous carbonates (red) and reflector B (light blue); (a) seismic section across the N-S graben (blue) and the NNE-SSW faults (green); (b) seismic section across the NE-SW half-graben (orange) and the NNE-SSW faults (green); (c) seismic section across the WNW-ESE faults (red). Note that the WNW-ESE and the NNE-SSW faults vanish in the Triassic package, while the N-S graben and the NE-SW half-graben reach the Permian package. See Fig. 11 for location of the lines.

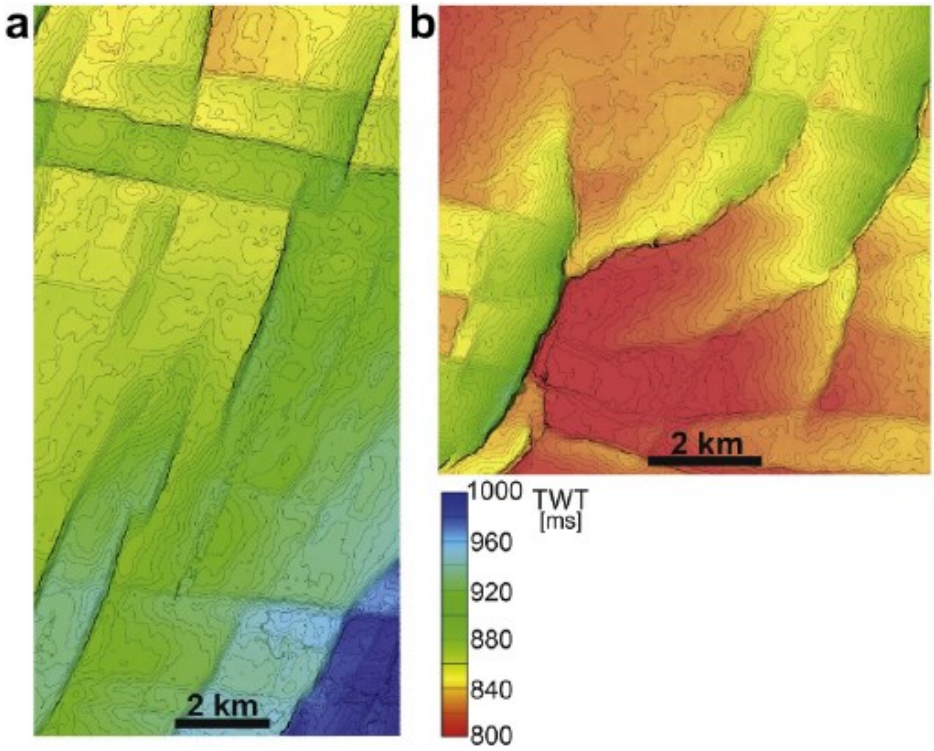

Fig. 9. Map view geometries of the NNE-SSW faults. See Fig. 11 for location of these areas; (a) *en echelon* arrangement of the NNE-SSW faults west of the NE-SW half-graben; (b) spoon-shaped geometry of the NNE-SSW faults east of the NE-SW half-graben.

Map view distribution and vertical extent indicate a clear distinction between the WNW-ESE, NNE-SSW and the NE-SW, N-S faults. The WNW-ESE and the NNE-SSW trends are represented by tens of closely spaced (1-2 km spacing) faults distributed in almost the whole area of the survey, while the N-S and the NE-SW trends are limited to the graben/half-graben in the central part of the survey and to the system that parallels it, 25 kilometers westwards (Fig. 7). Furthermore, the graben/half-graben develops through the whole Triassic clay-rich package reaching the Permian carbonates, while the WNW-ESE and the NNE-SSW faults affect only the upper part of the succession, vanishing into the Middle-Upper Triassic clays (Fig. 8). Finally, the NE-SW and the N-S faults are associated with higher throw than the NNE-SSW and the WNW-ESE faults (Fig. 8) (up to 300 ms of vertical separation for the NE-SW half-graben and up to 150 ms for the N-S graben versus 60 ms on average for the NNE-SSW faults and 30 ms for the WNW-ESE faults). Hence, the NE-SW and the N-S faults represent a focused deformation, while the NNE-SSW and the WNW-ESE faults suggest a well-distributed and widespread deformation.

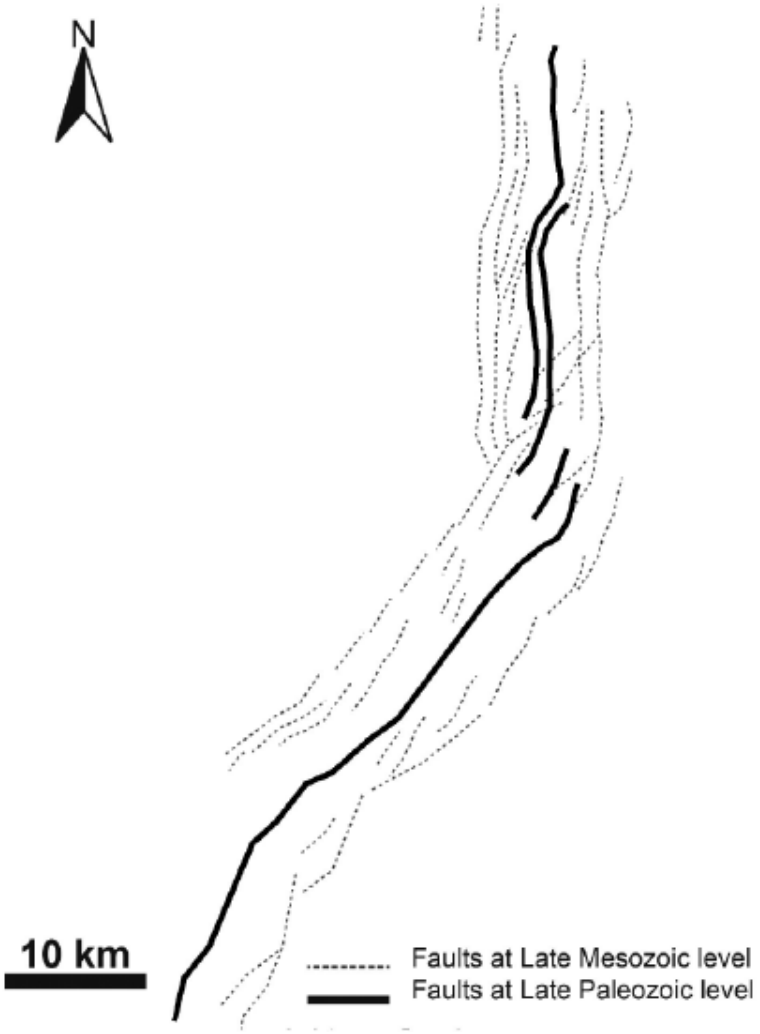

Fig. 10. Comparison between late Mesozoic and late Paleozoic structures. Dotted segments indicate shallow late Mesozoic faults; solid segments indicate deep late Paleozoic faults. The late Mesozoic NE-SW half-graben and graben correspond to a wide half-graben at Permian level, while at this level just a narrow graben can be observed corresponding to the Mesozoic N-S graben.

However, also the two trends of the graben/half-graben display significantly different features (map view geometries and vertical extent), in addition to the different throw. While the bounding faults of the N-S graben are straight in map view, the fault of the NE-SW half-graben display a segmented pattern, characterized by NNE-SSW major segments linked by NE-SW junctions (Fig. 7). Furthermore, the maps of deep horizons and the seismic sections highlighted a significant dislocation in the Permian carbonates corresponding to the NE-SW half-graben and only the basal termination of the N-S graben (Fig. 10).

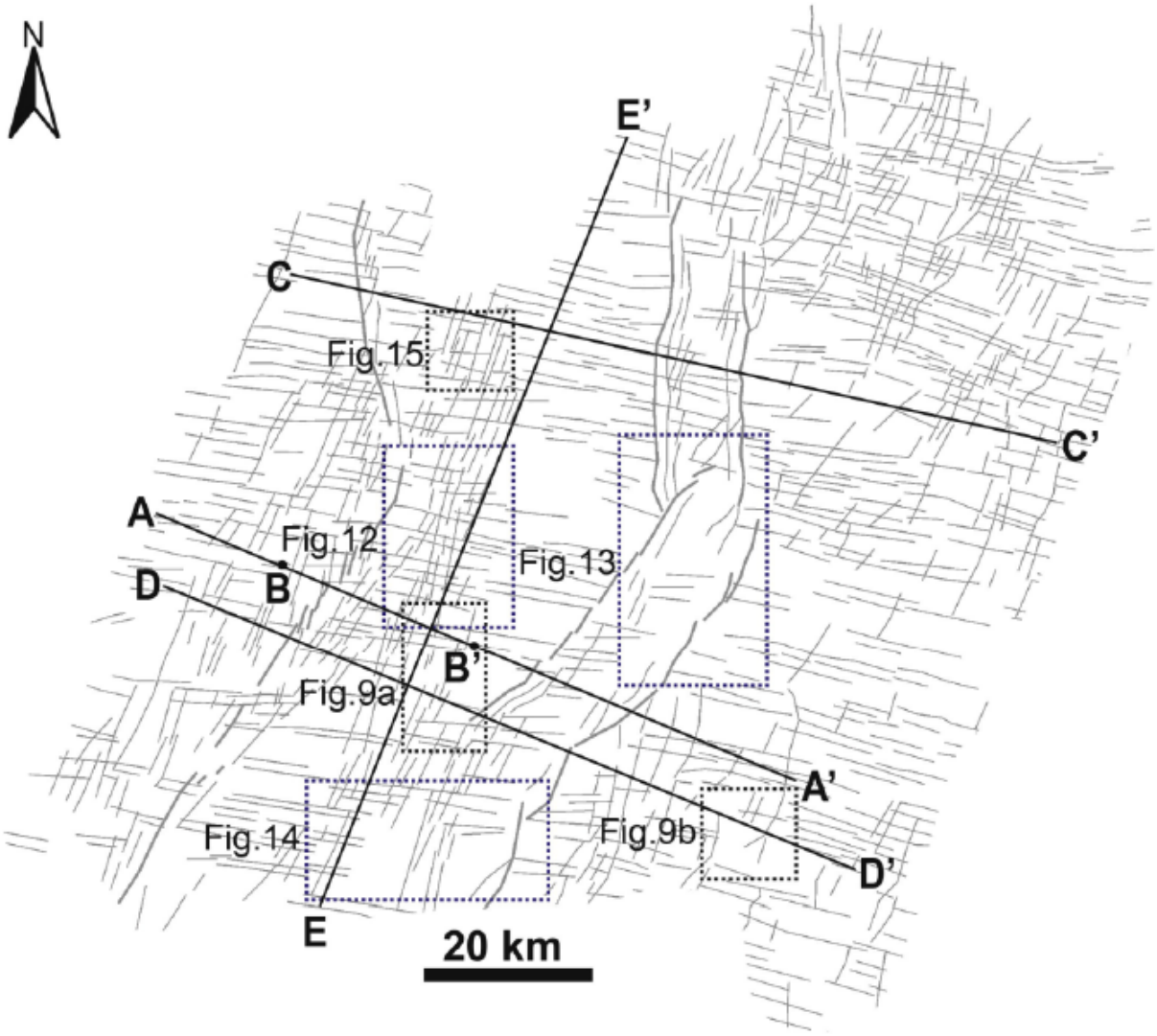

Fig. 11. Dotted blue boxes indicate the location of the time-thickness maps in Figs. 12, 13 and 14; dotted black boxes indicate the location of the close-ups of the WNW-ESE, NNE-SSW faults in Figs. 9a, 9b and 15; solid black lines indicate the location of seismic lines in Figs. 5, 6 and 8.

Similarly, some differences can be observed between the WNW-ESE and the NNE-SSW sets. The WNW-ESE faults are widespread in the whole area of the survey with homogeneous features, whereas the NNE-SSW faults are observed only at a distance of some kilometers from the graben/half-graben and display different geometrical characteristics to the west and to the east of this structure (Fig. 9). Indeed, the western ones display a straight pattern in map view with *en echelon* right stepover arrangement (Fig. 9a), whereas the eastern ones are characterized by map-view spoon-shaped geometry (Fig. 9b). This geometry, coupled with listric fault planes synthetic to the main fault of the NE-SW half-graben (Fig. 8b), suggests that these faults accommodated the gravitational collapse of the half-graben footwall.

The relative activation order of the various fault systems has been defined through the synsedimentary thickness variations. Three areas representative of the various fault trends have been selected and searched for thickness variations across the faults (Fig. 11).

The deepest time-thickness map (AB package) highlights outstanding thickness variations across the WNW-ESE faults and smaller thickness variations across the NNE-SSW (Fig. 12a). Hence, thickness variations indicate the simultaneous activity of these fault sets and confirm they belong to the same fault system, as suggested by the map view distribution and the vertical extent. No thickness increase has been observed within the graben/half-graben system in this interval, except for a localized thickness increase along the boundary faults of the N-S graben (Fig. 13a). Since picking and propagation errors are very likely to occur along the fault plane and no thickness variations can be observed otherwise in the inner part of the graben, we attributed this local thickness variation to mispicking, and consequently we inferred the inactivity of this structure during the deposition of AB package. In this time-thickness map, the major depocentre is located towards the south-western margin of the study area and corresponds to the ancient Maud Basin (Fig. 14a). Hence, during this time interval the general pattern of sedimentation was still controlled by structures pre-existing the late Mesozoic rifting.

In the time-thickness map of the overlying stratigraphic interval (BC package), sharp thickness variations have been observed across the WNW-ESE and the NNE-SSW faults (Fig. 12b), indicating the ongoing activity of these systems. A general thickness variation is observed across the NE-SW half-graben (Figs.13b and 14b) whereas no thickness variations match the N-S graben (Fig.13b). The thickness variation across the NE-SW half-graben suggests a reactivation of this inherited structure during this time interval. Moreover, the Maud Basin does not appear as a depocentre anymore, hence the sedimentation seems to be mainly constrained by structures related to the late Mesozoic rifting.

In the shallowest time-thickness map (CD package), the main thickness variations are associated with the N-S graben (Fig.13c) and the NE-SW half-graben (Fig.14c), distinct thickness variations can be observed across the NNE-SSW faults but there are no apparent thickness variations across the WNW-ESE ones (Fig.12c). This setting suggests that, during this time interval, the regional strain was mainly accommodated by the graben/half-graben system. However, NNE-SSW faults continue to be extensionally active, unlike the WNW-ESE. The thickness variations across faults are accompanied by a general thickness increase northwards (Fig. 13c), that likely reflects the origin of the sediment.

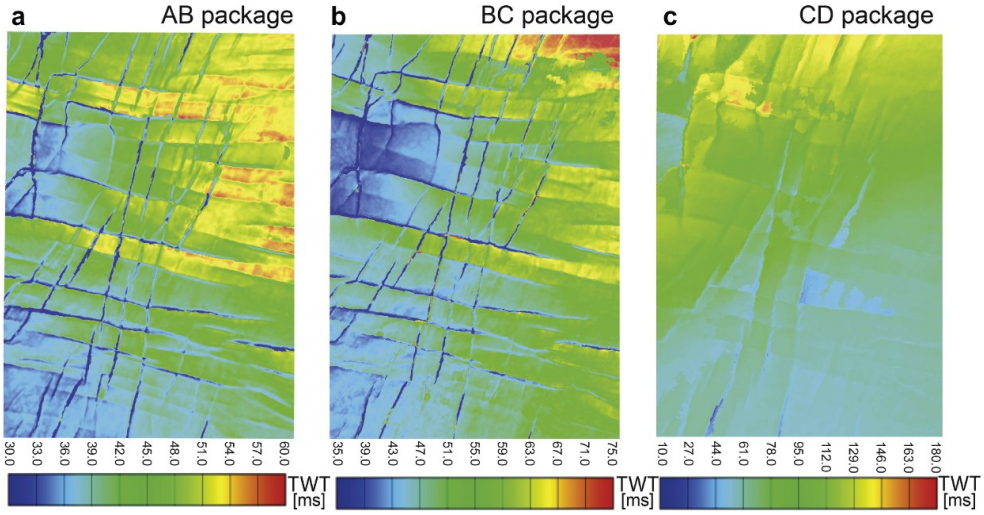

Fig. 12. Time-thickness maps across the WNW-ESE and the NNE-SSW faults. (a) time-thickness map of the package between reflector A and reflector B (deepest interval); (b) time-thickness map of the package between reflector B and reflector C (intermediate interval); (c) time-thickness map of the package between reflector C and reflector D (shallowest interval). Note the initial coeval activity of the WNW-ESE and the NNE-SSW faults (a and b), followed by the deactivation of the WNW-ESE ones (c). See Fig. 11 for location of this area.

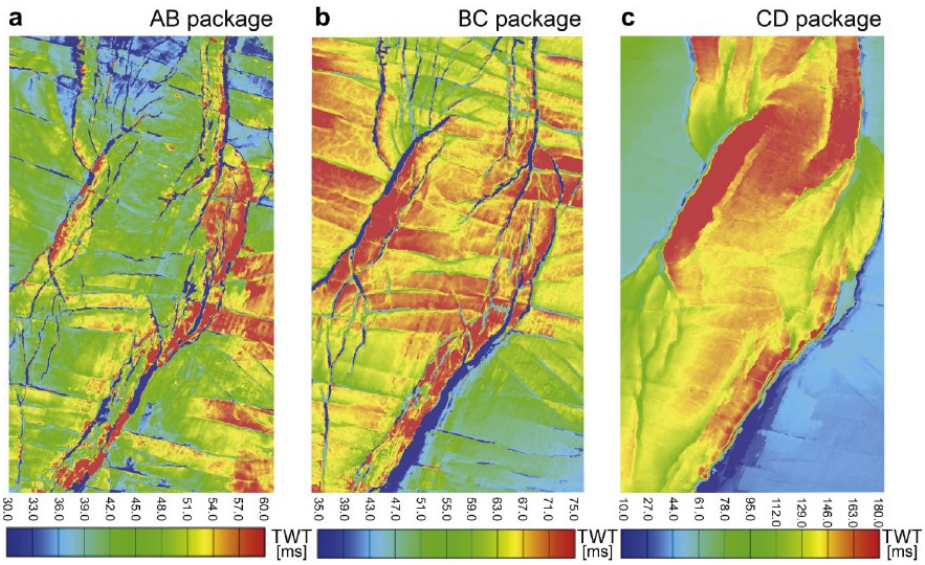

Fig. 13. Time-thickness maps across the N-S and the NE-SW graben. (a) time-thickness map of the package between reflector A and reflector B (deepest interval); (b) time-thickness map of the package between reflector B and reflector C (intermediate interval); (c) time-thickness map of the package between reflector C and reflector D (shallowest interval). Note the progressive activation of the NE-SW half-graben (b) and of the N-S graben (c), accompanied by the deactivation of the WNW-ESE faults. See Fig. 11 for location of this area.

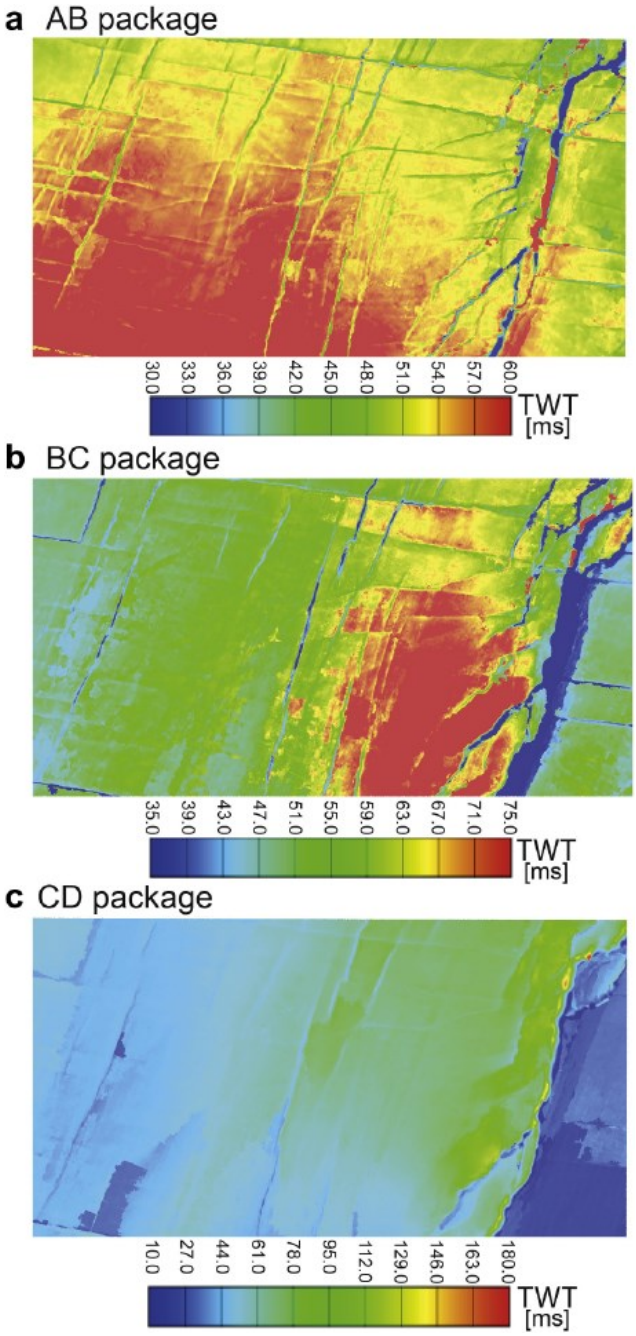

Fig. 14. Time-thickness maps across the NE-SW half-graben. (a) time-thickness map of the package between reflector A and reflector B (deepest interval); (b) time-thickness map of the package between reflector B and reflector C (intermediate interval); (c) time-thickness map of the package between reflector C and reflector D (shallowest interval). Note the switch of the main depocentre from the Maud Basin (located south of this map) (a) to the NE-SW half-graben (b and c). See Fig. 11 for location of this area.

5. Discussion

Thickness variations in AB and BC packages (Figs. 12a and 12b) indicate clearly the simultaneous activity of WNW-ESE and NNE-SSW fault sets, suggesting their interpretation as conjugate sets of an orthorhombic system. The simultaneous activity of these systems is confirmed even by their mutually non-univocal cross-cutting relationships (Fig. 15). Finally, even the similar vertical extent (Fig. 8) and spatial distribution (Fig. 7) of the two sets suggest their association. However, minor thickness variation across the NNE-SSW faults and local *en echelon* arrangement associated with some segments of this system (Fig. 9a) suggest a more relevant transtensional component for this set with respect to the WNW-ESE during the early phases of rifting.

The orthorhombic system was the first structure to develop at the onset of the late Mesozoic rift (Figs. 12a, 13a and 14a). Later, as the rifting progressed (Figs. 12b, 13b and 14b), the activity of the orthorhombic system was accompanied by the activation of the NE-SW half-graben, which became predominant during the last time interval investigated (Figs. 12c, 13c and 14c), when also the N-S graben initiated. In this last time interval also the NNE-SSW set of the orthorhombic system was surely active, whereas no evidence of the activity of the WNW-ESE faults has been detected. The development of an orthorhombic system at the beginning of the late Mesozoic rifting in the Hoop Fault Complex seems to be closely related to the rheological layering of the sedimentary succession.

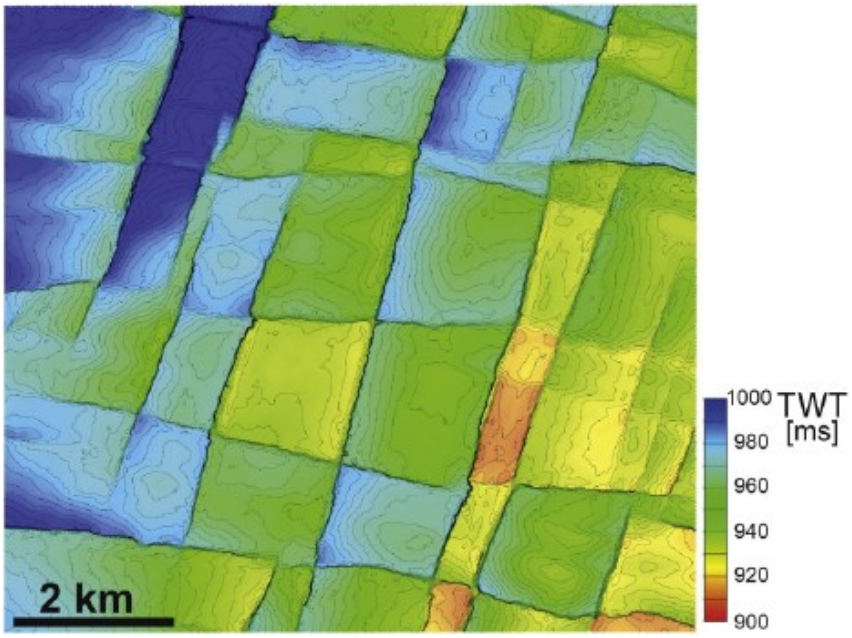

Fig. 15. Map view of the orthorhombic system. No consistent cross-cutting relationships between the two sets of the orthorhombic system can be observed, confirming the coeval activity of the two sets. See Fig. 11 for location of this area.

Indeed, as shown in Fig. 8, a ca. 1500-2000 m thick interval of Middle-Upper Triassic clays confined vertically the orthorhombic system, limiting the extent of stress drop zone around faults and inhibiting fault linkage and coalescence. This resulted in the well-distributed, regularly spaced faults of the orthorhombic system (Fig. 7), which is typical of vertically confined fault systems (Soliva and Schultz, 2008).

During the initial phases of the rifting, the strain localization on clay minerals (Collettini *et al.*, 2009; Montesi, 2013) most probably slowed down the downward propagation of the fault planes, leading to the decoupling of the upper part of the succession, devoid of pre-existing discontinuities, from any deep structures. Hence, in the upper part of the succession the orthorhombic fault system could develop as the direct expression of the actual strain field, while in the lower part the deformation focused on pre-existing structures, preventing the formation of new faults.

As the rifting proceeded, the role of inherited deep structures became dominant. This is evident both at the scale of the whole Barents Shelf and at the scale of our study area. Indeed, on one hand the overall rifting architecture of the Barents has been proven to reflect deep basement trends (Gernigon *et al.,* 2014), on the other in our study area the activity of the orthorhombic system was followed by the activation of the NE-SW half-graben, which several pieces of evidence suggest to be a reactivated structure of the Permian rift. Certainly, seismic lines and time-structure maps highlight a significant dislocation corresponding to the NE-SW half-graben at the Permian level (Figs. 8 and 10). In addition, a thickness increase and a change from parallel seismic facies to clinoforms geometries can be observed across the NE-SW half-graben in the Triassic package (Fig. 8b). Similar features have been described across other NE-SW faults nearby our study area and have been related to differential compaction over late Paleozoic grabens or reactivation of late Paleozoic faults (Glørstad-Clark *et al.*, 2010), suggesting this is an inherited Permian fault trend. Finally, the NE-SW half-graben displays a segmented pattern in the late Mesozoic map (Fig. 7) that resembles the geometries observed in analogue models for oblique reactivation of inherited structures (Corti, 2012). Hence, the decoupling action of the clay interval was efficient until some point of the deformation, after which the deep structures reached the shallowest part of the succession, deactivating the orthorhombic system and controlling the subsequent structural evolution. However, also a change of the strain field played an important role in the development of the rift. Indeed, the N-S graben, the last structure to be activated in our study area, is a newly formed structure, indicative of a change from 3D to planar strain field.

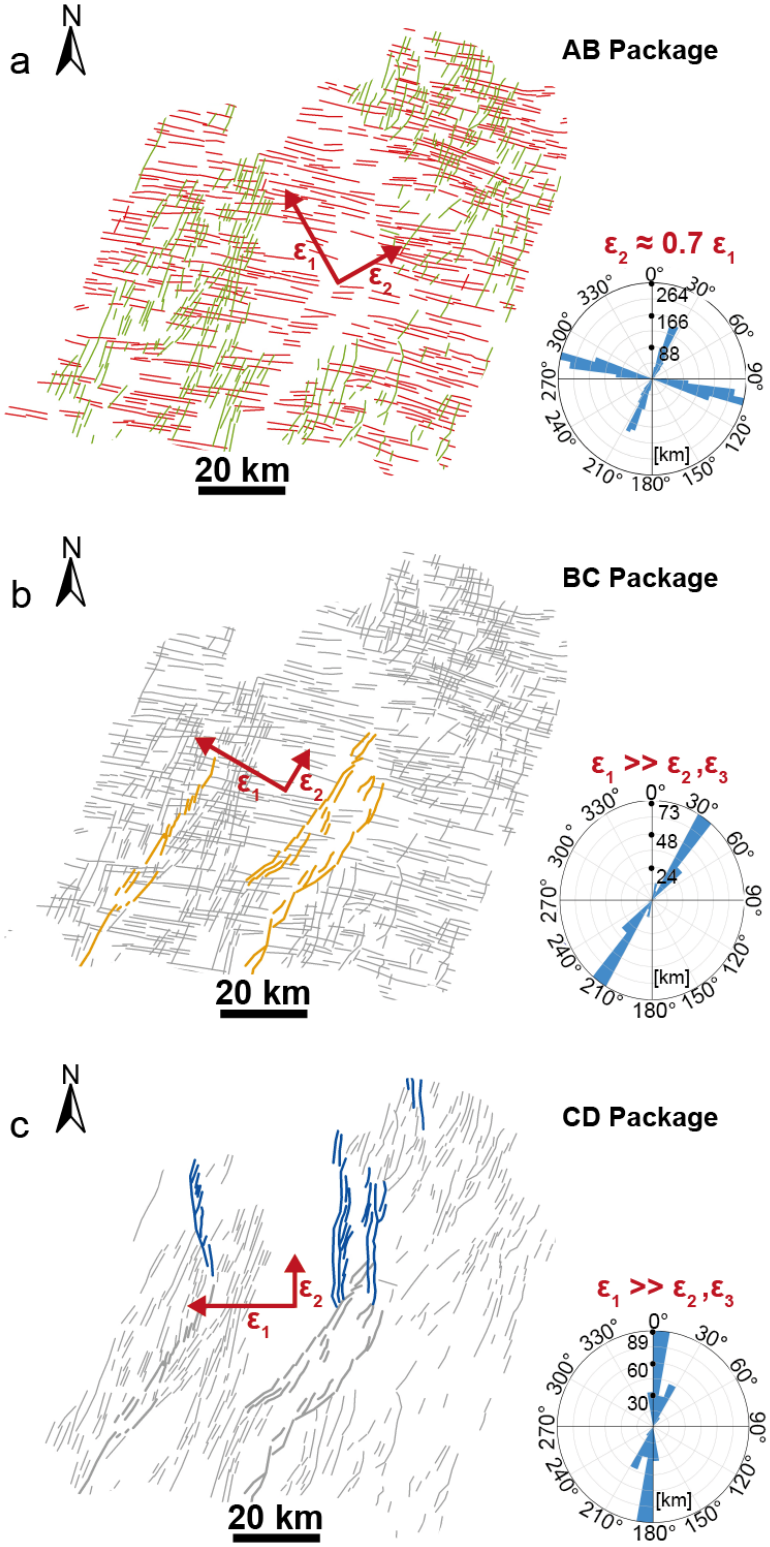

Fig. 16. Activity range of the various fault systems and strain field evolution. The faults active in each stratigraphic interval have been traced, distinguishing the faults already active (grey ones) and the faults activated in that specific interval (colored ones), which are indicative of the strain field. Red arrows indicate the principal strain axes. (a) faults active and strain field in the deepest stratigraphic interval (AB package); (b) faults active and strain field in the intermediate stratigraphic interval (BC package); (c) faults active and strain field in the shallowest stratigraphic interval (CD package). Fault segments were weighted by their length in the rose diagrams.

Two different observations point out that the N-S graben is a newly formed structure. Only the basal termination of the N-S graben has been observed at the Permian level, proving this is not an inherited structure of the Permian rift (Fig. 10). In addition, the N-S graben displays straight boundaries and internal faults (Fig. 7), as it has been observed in the analogue models of structures developed perpendicularly to the extension axis (Corti, 2012).

Based on this structural analysis, the evolution of the strain field in the Hoop Fault Complex during the late Mesozoic has been reconstructed. An oblate strain ellipsoid with the extension axes coincident with the bisectors of the angles between the fault sets has been associated to the orthorhombic system, according to Reches (1978). Furthermore, the strain ratio *K* has been calculated from the acute intersection angle α between the fault sets:

$$K= \varepsilon_2/\varepsilon_1=\tan^2(\alpha/2)=\tan^2(80°/2)=0.7$$

and the principal strain axes ε_1 and ε_2 have been placed respectively as the bisector of the obtuse and the acute angles (Fig. 16) according to Krantz (1988). Hence, the orthorhombic fault system of the Hoop Fault Complex and surroundings is the expression of an oblate strain/stre field with a preferential extension direction oriented N330° (Fig. 16). The oblate strain field could be due to the interaction between the Atlantic and the Arctic rifts, which prevented the definition of a unique extension axis. This interaction determined a component of shear in the Barents rifting (Faleide *et al.*, 1993), which could be responsible for the *en echelon* arrangement of the NNE-SSW set of the orthorhombic system (Fig. 9a).

The subsequent reactivation of the NE-SW half-graben marks the transition from a 3D strain field to a planar strain field, with the main extension axis oriented N300° (Fig. 16). This transition does not necessarily imply a change in the strain field since the NE-SW half-graben is a reactivated structure and the oblate strain field, which led to the development of the orthorhombic system, could account also for its reactivation. However, a change from the oblate strain field to a planar one cannot be excluded.

Finally, the development of the N-S graben indicates an anti-clockwise rotation of the main extension axis, from N300° to N270° (Fig. 16). Since the N-S graben appears as a newly formed structure, perfectly responding to the theory of Anderson, it must be the expression of planar strain and strain fields, with the least principal strain σ_3 clearly defined and oriented perpendicularly to the N-S graben. This evolution of the strain field is indicated also by the ongoing extensional

activity of the NNE-SSW set of the orthorhombic system, more properly oriented than the WNW-ESE faults.

Considering the structural evolution of the Hoop Fault Complex as a whole, two main trends have been highlighted: a transition from 3D to planar strain field and an anti-clockwise rotation of the main extension axis. Although the reactivation of deep structures had a great deal of influence over the structural evolution of the Barents, these trends could reflect the geodynamic setting, characterized by the progressive northward opening of the North Atlantic during the late Mesozoic (Dorè *et al.*, 1991). Indeed, the approaching of the Atlantic break-up could have led to a progressive focusing of the extension along a specific direction, accompanied by a rotation of the main extension axis.

According to our analysis, the two fundamental conditions for the development of the orthorhombic fault system of the Hoop Fault Complex were the decoupling from the deep structures and a tectonic setting preventing the definition of a unique extension direction. Even though the clay-rich interval clearly acted as a detachment, constraining the orthorhombic fault system to the upper part of the succession, a far field control of the deep buried structures on the orthorhombic system is discernible. Indeed, the NNE-SSW set of the orthorhombic system is less developed near the graben and it was less extensionally active than the WNW-ESE set in the early phase of the rifting. The focusing of the deformation on the deep structures with trends similar to the NNE-SSW set (Fig. 10) decreased the activity along the faults of this set and at places prevented their development, while the WNW-ESE system, having a very different trend, was unaffected by the buried faults. This suggests that the deep structures had an influence on the shallow strain field even prior to their propagation to the surface.

Our identification of an orthorhombic system at the scale of tens of kilometers indicates that these fault arrangements can be not only small scale elements, responding to local perturbation of the stress field (Aydin and Reches, 1982; Krantz, 1988; Miller *et al.*, 2007; Carvell *et al.*, 2014), but significant features in terms of regional tectonics, as suggested by Franceschi *et al*. (2014). Indeed, Franceschi *et al*. (2014) reconstructed the development of an orthorhombic fault system at the scale of tens of kilometers during the Jurassic rifting of the Trento Platform (NE Alps). The identification of an orthorhombic system at the same scale, active during the late Mesozoic rifting of the Barents Sea, confirms the connection between orthorhombic faulting and specific rifting settings.

6. Conclusions

Our analysis detected an orthorhombic fault system at the scale of tens of kilometers in the area of the Hoop Fault Complex (SW Barents Sea), indicating that these fault arrangements can be significant in terms of regional tectonics. The orthorhombic faulting is the expression of an oblate strain ellipsoid (Reches, 1978; Krantz, 1988), here characterized by a distributed faulting in the whole horizontal plane, with a preferential direction of extension oriented NNW-SSE. The absence of a unique extension direction could reflect the interaction between the Atlantic and the Arctic rifts in the Barents Shelf.

The orthorhombic system developed at the onset of the late Mesozoic rift and affected only the upper brittle part of the succession, which during the early phases of the rifting was decoupled from the deep structures by a several 100s m thick ductile succession of clays. Otherwise, in the lower part of the succession pre-existing structures focused the deformation, preventing the growth of new faults. Hence, the interleaving of a thick horizon of detachment within the succession of the Hoop Fault Complex and the consequent decoupling between deep inherited faults and shallow superstructures allowed for the expression of a 3D stress field as an orthorhombic fault system, making the Hoop Fault Complex an exceptional record of the strain field evolution during the early phases of a rift.

As the rifting proceeded, the oblate strain field evolved into a planar strain field with the extension focused along a specific direction, as indicated by the reactivation of a deep NE-SW half-graben and the activation of a new N-S graben. This transition was accompanied by the rotation of the main extension axis from NNE-SSW to E-W (Fig. 16). The focusing of the deformation on deep structures and their propagation towards the surface played possibly an important role in the evolution of the strain field. However, the change in the stress field indicated by the activation of the N-S graben, a completely new structure, certainly was significant in the transition from oblate to planar strain. The focusing of the extension along a specific direction could reflect the approaching of the North Atlantic break-up, which started in the Central Atlantic and progressively moved northwards (Dorè *et al.*, 1999). The comparison with other rifting settings could clarify whether the onset of the 3D stress field reflects the interaction between two rifts (the Atlantic and the Arctic) or a general process, happening during the early phases of rifting events.

Acknowledgements

We would like to thank TGS for permission to use and to publish the seismic data and DownUnder Geosolutions for providing the seismic interpretation software. Reidun Myklebust is recognized for her contribution in reading and commenting the manuscript. Thanks to Dr. Nick Timms and to Prof. Peter Betts for their constructive reviews of the manuscript.

7. Supplementary materials

The theory of Reches was first proposed in 1978 to account for the simultaneous activity of different fault sets arranged in orthorhombic symmetry (Reches, 1978). The theory is based on a mathematical model which assumes that (i) the deformation is accommodated solely by slip; (ii) the distribution of the deformation is homogeneous; (iii) the resistance to faulting is cohesive, and thus independent of the normal stress. Two logical steps can be distinguished in the mathematical analysis of Reches. First, four sets of faults are demonstrated to be sufficient to accommodate a general deformation in three dimensions (Fig. 1a). Then, a symmetrical arrangement with respect to the principal stress axes is deduced from the assumption of a homogeneous stress distribution (Fig. 1b). By combining these results, orthorhombic fault system are predicted to develop in response to 3D deformation.

Subsequently, this model has been corroborated by experiments on rock failure, where four sets of faults in orthorhombic symmetry were observed under "truly triaxial" stresses (Reches and Dieterich, 1983). Finally, the theory of Reches has been further developed from a mathematical point of view by Krantz (1988), assuming that the slip is equally distributed among the fault sets. This work proposed a relationship between the strain ratio ($\varepsilon_2/\varepsilon_1$) and the angle α between the fault sets:

$$\varepsilon_2/\varepsilon_1=\tan^2(\alpha/2),$$

finding a good agreement between the prediction of the model and the geometric and kinematic parameters of the normal fault array of San Rafael Swell in central Utah.

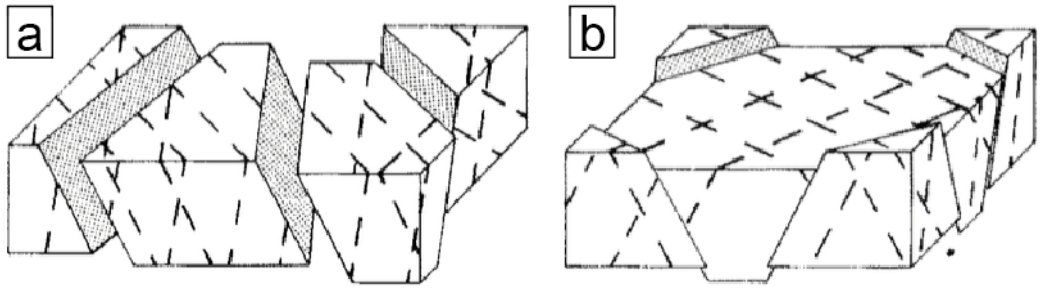

Fig. 16. Block diagrams illustrating the main results of the theory of Reches (modified after Reches, 1978). First, four sets of faults are demonstrated to be sufficient to accommodate any kind of 3D deformation (Fig. 1a); then, a preferential orthorhombic arrangement is inferred putting additional assumptions (Fig. 1b).

References

Anderson, E.M., 1951. The Dynamics of Faulting. Oliver and Boyd, London, (183 pp.).

Aydin, A., Reches, Z., 1982. Number and orientation of fault sets in the field and in experiments. Geology 10, 107–112. doi:10.1130/0091-7613(1982)10<107:NAOOFS>2.0.CO;2

Carvell, J., Blenkinsop, T., Clarke, G., Tonelli, M., 2014. Scaling, kinematics and evolution of a polymodal fault system: Hail Creek Mine, NE Australia. Tectonophysics 632, 138–150. doi:10.1016/j.tecto.2014.06.003

Collettini, C., Niemeijer, A., Viti, C., Marone, C., 2009. Fault zone fabric and fault weakness. Nature 462, 907–910. doi:10.1038/nature08585

Corti, G., 2012. Evolution and characteristics of continental rifting: Analog modeling-inspired view and comparison with examples from the East African Rift System. Tectonophysics 522–523, 1–33. doi:10.1016/j.tecto.2011.06.010

Dalland, A., Worsley, D., Ofstad, K., 1988. A lithostratigraphic scheme for the Mesozoic and Cenozoic succession offshore mid- and northern Norway. Norwegian Petroleum Directorate Bulletin 4, (65 pp.).

Doré, A.G., 1991. The structural foundation and evolution of Mesozoic seaways between Europe and the Arctic. Palaeogeography, Palaeoclimatology, Palaeoecology 87, 441–492. doi:10.1016/0031-0182(91)90144-G

Doré, A.G., Lundin, E.R., Jensen, L.N., Birkeland, **Ø**., Eliassen, P.E., Fichler, C., 1999. Principal tectonic events in the evolution of the northwest European Atlantic margin, in: Petroleum Geology of Northwest Europe: Proceedings of the 5th Conference. Geological Society of London, pp. 41–61.

DUG Insight (version 3.0). Windows/Linux/Mac. Perth, Western Australia: DownUnder GeoSolutions (http://www.dugeo.com).

Faleide, J.I., Tsikalas, F., Breivik, A.J., Mjelde, R., Ritzmann, O., Engen, O., Wilson, J., Eldholm, O., 2008. Structure and Evolution of the Continental Margin off Norway and the Barents Sea. Episodes 31, 82–91.

Faleide, J.I., Vågnes, E., Gudlaugsson, S.T., 1993. Late Mesozoic-Cenozoic evolution of the south-western Barents Sea in a regional rift-shear tectonic setting. Marine and Petroleum Geology 10, 186–214. doi:10.1016/0264-8172(93)90104-Z

Franceschi, M., Massironi, M., Franceschi, P., Picotti, V., 2014. Spatial analysis of thickness variability applied to an Early Jurassic carbonate platform in the central Southern Alps (Italy): a tool to unravel syn-sedimentary faulting. Terra Nova 26, 239–246.

doi:10.1111/ter.12092

Gabrielsen, R.H., Færseth, R.B., Jensen, L.N., Kalheim, J.E., Riis, F., 1990. Structural elements of the Norwegian continental shelf, Part I: The Barents Sea Region, Norwegian Petroleum Directorate Bulletin 6, (33 pp.).

Gernigon, L., Brönner, M., Roberts, D., Olesen, O., Nasuti, A., Yamasaki, T., 2014. Crustal and basin evolution of the southwestern Barents Sea: From Caledonian orogeny to continental breakup: Evolution of the Barents Sea. Tectonics 33, 347–373. https://doi.org/10.1002/2013TC003439

Glørstad-Clark, E., Birkeland, E.P., Nystuen, J.P., Faleide, J.I., Midtkandal, I., 2011. Triassic platform-margin deltas in the western Barents Sea. Marine and Petroleum Geology 28, 1294–1314. doi:10.1016/j.marpetgeo.2011.03.006

Glørstad-Clark, E., Faleide, J.I., Lundschien, B.A., Nystuen, J.P., 2010. Triassic seismic sequence stratigraphy and paleogeography of the western Barents Sea area. Marine and Petroleum Geology 27, 1448–1475. doi:10.1016/j.marpetgeo.2010.02.008

Gudlaugsson, S.T., Faleide, J.I., Johansen, S.E., Breivik, A.J., 1998. Late Palaeozoic structural development of the South-western Barents Sea. Marine and Petroleum Geology 15, 73–102. doi:10.1016/S0264-8172(97)00048-2

Healy, D., Blenkinsop, T.G., Timms, N.E., Meredith, P.G., Mitchell, T.M., Cooke, M.L., 2015. Polymodal faulting: Time for a new angle on shear failure. Journal of Structural Geology 80, 57–71. doi:10.1016/j.jsg.2015.08.013

Healy, D., Jones, R.R., Holdsworth, R.E., 2006. Three-dimensional brittle shear fracturing by tensile crack interaction. Nature 439, 64–67. doi:10.1038/nature04346

Jakobsson, M., Mayer, L.A., Coakley, B., Dowdeswell, J.A., Forbes, S., Fridman, B., Hodnesdal, H., Noormets, R., Pedersen, R., Rebesco, M., Schenke, H.W., Zarayskaya, Y., Accettella, A.D., Armstrong, A., Anderson, R.M., Bienhoff, P., Camerlenghi, A., Church, I., Edwards, M., Gardner, J.V., Hall, J.K. , Hell, B., Hestvik, O. B., Kristoffersen, Y., Marcussen, C., Mohammad, R., Mosher, D., Nghiem, S.V., Pedrosa, M.T.Travaglini, P. G., Weatherall P., 2012. The International Bathymetric Chart of the Arctic Ocean (IBCAO) Version 3.0, Geophysical Research Letters. doi: 10.1029/2012GL052219

Klausen, T.G., Ryseth, A., Helland-Hansen, W., Gjelberg, H.K., 2016. Progradational and backstepping shoreface deposits in the Ladinian to Early Norian Snadd Formation of the Barents Sea. Sedimentology 63, 893–916. doi:10.1111/sed.12242

Krantz, R.W., 1988. Multiple fault sets and three-dimensional strain: Theory and application.

Journal of Structural Geology 10, 225–237. doi:10.1016/0191-8141(88)90056-9

Miller, J.M., Nelson, E.P., Hitzman, M., Muccilli, P., Hall, W.D.M., 2007. Orthorhombic fault–fracture patterns and non-plane strain in a synthetic transfer zone during rifting: Lennard shelf, Canning basin, Western Australia. Journal of Structural Geology 29, 1002–1021. doi:10.1016/j.jsg.2007.01.004

Montesi, L.G.J, 2013. Fabric development as the key for forming ductile shear zones and enabling plate tectonics. Journal of Structural Geology 50, 254-266. doi: 10.1016/j.jsg.2012.12.011

Reches, Z., 1983. Faulting of rocks in three-dimensional strain fields II. Theoretical analysis. Tectonophysics 95, 133–156. doi:10.1016/0040-1951(83)90264-0

Reches, Z., 1978. Analysis of faulting in three-dimensional strain field. Tectonophysics 47, 109–129. doi:10.1016/0040-1951(78)90154-3

Reches, Z., Dieterich, J.H., 1983. Faulting of rocks in three-dimensional strain fields I. Failure of rocks in polyaxial, servo-control experiments. Tectonophysics 95, 111–132. doi:10.1016/0040-1951(83)90263-9

Soliva, R., Schultz, R.A., 2008. Distributed and localized faulting in extensional settings: Insight from the North Ethiopian Rift–Afar transition area. Tectonics 27, TC2003. doi:10.1029/2007TC002148

Tsikalas, F., Faleide, J.I., Eldholm, O., Blaich, O.A., 2012. The NE Atlantic conjugate margins, in: D.G. Roberts (ed.), Regional Geology and Tectonics: Phanerozoic Passive Margins, Cratonic Basins and Global Tectonic Maps. Elsevier, Amsterdam, The Netherlands, pp. 140–201.

Worsley, D., 2008. The post-Caledonian development of Svalbard and the western Barents Sea. Polar Research 27, 298–317. doi:10.1111/j.1751-8369.2008.00085.x

PAPER 2

To be submitted to *Nature Geoscience*

LOCAL INSTABILITY OF FAULT INTERACTIONS IS THE KEY TO 3D DEFORMATION

Luca Collanega[1], Giacomo Corti[2], Anna Breda[1], Matteo Massironi[1]

[1] Dipartimento di Geoscienze, University of Padova, Via G.Gradenigo, 6 - 35131 Padova, Italy

[2] CNR, Consiglio Nazionale delle Ricerche, Istituto di Geoscienze e Georisorse, U.O. Firenze, Via G.La Pira, 4, 50121 Florence, Italy

Corresponding author: luca.collanega@gmail.com

To be submitted to *Nature Geoscience*

All four authors were actively involved in designing and discussing the experiments. Luca Collanega performed the analogue models, drafted the manuscript and all the figures. Giacomo Corti had a key-role in implementing the experiments and developing the comparison to natural examples. Anna Breda and Matteo Massironi inspired discussions and edited the final manuscript.

ABSTRACT

Orthorhombic fault patterns have been typically thought to be the preferential fault arrangements to accommodate 3D deformation. However, previous models considered the deformation to occur under stable stress/strain conditions, thereby excluding the possibility of an interaction between developing faults. Here, we show that in a 3D strain field the strike of new incipient faults is strongly controlled by adjacent more mature faults, preventing the development of orthorhombic patterns. We use analogue models, along with analysis of the local and global strain fields, to reconstruct the dynamics of 3D deformation. Even within a globally stable strain field, fault geometries indicate a strong spatial and temporal instability of the local extension direction, which appears to be primarily controlled by the stress drop occurring in the proximity of developing

faults. Final fault geometries display a strong similarity with fault patterns in tectonic settings under the simultaneous influence of different rift systems, which thus appear prone to the onset of 3D strain fields. We conclude that local interactions between adjacent faults through their local stress field exert a primary control on the accommodation of 3D deformation.

1. Introduction

Although the deformation of the continental crust clearly occurs in a 3D environment, the classic and most widespread model of deformation, the theory of Mohr-Coulomb, assumes the deformation to be bi-dimensional (Anderson, E.M., 1952). Strong experimental evidence supports this model of deformation, with different experimental set-ups highlighting the development of systems of sub-parallel faults perpendicular to the extension direction (*e.g.* Withjack and Jamison, 1986; McClay and White, 1995). Furthermore, by introducing multiple phases of deformation or oblique reactivation of pre-existing structures, this simple model can account for complex fault patterns with several sets of curvilinear, segmented and zig-zag faults (Keep and McClay, 1997; Henza *et al.*, 2011). However, the 2D nature of the deformation remains uncertain, with the simultaneous activity of different fault sets suggesting the onset of 3D strain fields in both natural and laboratory examples (Reches, 1978; Healy *et al.*, 2015). In particular, 3D strain fields can arise at the local scale in response to (i) stress perturbations around salt diapirs (Nikolinakou *et al.*, 2014; Coleman *et al.*, 2018) and (ii) within overlapping transfer zones (Miller *et al.*, 2007). More recently, 3D strain fields have been suggested to occur also at the regional scale (Collanega *et al.*, 2017; McCormack *et al.*, 2018), playing possibly an important role in terms of tectonic processes. The classic model of 3D deformation considers the development of faults under homogeneous and stable stress/strain conditions, implying that faults should develop symmetrically with respect to the strain axes (i.e. in the case of four fault sets, with orthorhombic symmetry; Reches, 1978; 1983). However, seismological studies indicate that the rupture of a fault has an immediate effect on the local stress field, with the decrease of the seismicity rate indicating a long-lasting stress drop in the adjacent region of a fault (Stein, 1999; Toda *et al.*, 2012). In particular, the development of a normal fault appears to hinder the nucleation and propagation of other faults accommodating the same component of the extension, as indicated by characteristic spacing and throw patterns of normal faults in 2D strain fields (Gupta and Scholz, 2000). Recreating both isotropic radial extension and synchronous extension along two perpendicular directions, we highlighted a strong spatial and temporal variability of the extension direction even within a globally stable strain field. The local interactions between developing faults are shown to be the primary control on the local strain field and thus on the final fault geometries, going well beyond the model of orthorhombic faulting.

2. Analogue modelling

In order to highlight spatial and temporal variations of the local strain field, we reproduced simple, stable and highly symmetrical strain fields: isotropic radial extension and synchronous bidirectional extension. As we used gravity-driven models, the shape of the model proved to be the most efficient way to constrain the overall strain field, with a circular model producing isotropic radial extension and a square model producing synchronous bidirectional extension (see for more details the Methods section in the Supplementary Materials).

2.1. Isotropic radial extension

Isotropic radial extension results in a polygonal fault pattern with a uniform strike distribution (Fig. 1a, rose diagram). Normal faults generally intersect each other at high angles (90°-120°), producing triple junctions of grabens (Fig. 1a, intersection angles). Two arms of the triple junctions typically accrue more displacement than the third one and merge into a major curvilinear graben. This evolution results in two populations of faults with different length and sinuosity: (i) major, high-sinuosity normal faults and (ii) minor, straight faults intersecting the former in their points of maximum curvature (Fig. 1a, Fault length-sinuosity).

The major curvilinear grabens and the associated minor normal faults develop simultaneously since the onset of deformation (Fig. 1b, Stage T_1), suggesting they are kinematically related structures. As the deformation proceeds, the curvilinear grabens accrue more displacement than the straight faults (Fig. 1b, Stage T_2), reflecting an anisotropic strain field with a preferential extension direction perpendicular to the curvilinear faults (Fig. 1b, strain evolution). Although the local strain field associated with each triple junction is anisotropic, the global strain field of the whole model remains radially isotropic during the whole experiment (Fig. 1b, strain evolution). Hence, the anisotropic local strain fields associated with differently oriented triple junctions appear to compensate one another through the interaction between adjacent faults.

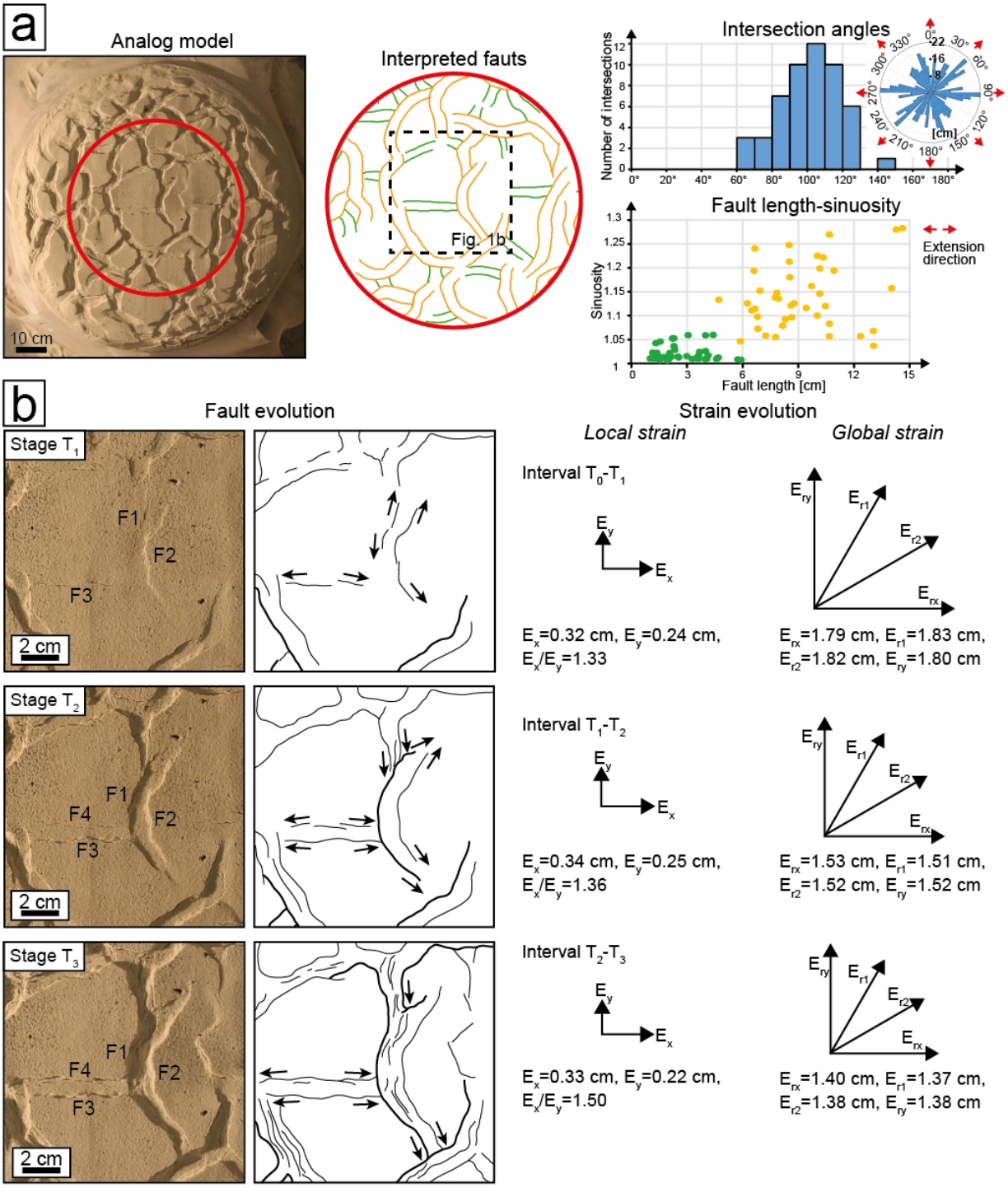

Fig. 1 Analogue model of faulting under isotropic radial extension. a, Final-stage fault pattern with analysis of fault geometries (intersection angles, strike distribution, fault length and sinuosity). Fault geometries were analysed in the central part of the model delimited by the red circle. Major curvilinear faults (orange segments) intersect minor straight faults (green segments) in their points of maximum curvature. In the fault length-sinuosity diagram, orange points and green points correspond to curvilinear and straight faults, respectively. **b**, Faults evolution, with quantification of the local and global deformation. Extension on the x direction appears dominant within the area shown in b, whilst at the global scale extension is equal along each radial direction.

2.2. Synchronous bidirectional extension

When a model is extended simultaneously along two perpendicular directions, two fault systems develop perpendicularly to each extension direction (Fig. 2a, rose diagram), which thus appear to have acted independently one from the other. The two fault systems (in our models, striking N-S and E-W) are equally developed in terms of total length (Fig. 2a, rose diagram), as faults of each system are truncated by faults of the other in equal measure (Fig. 2a, interpreted faults). The geometry of fault intersections appears to be controlled by the relative maturity of the intersecting faults, with low-displacement faults terminating against more mature faults, producing T-shaped intersections. When the two intersecting faults have similar maturity, they generally terminate one against the other, with the development of L-shaped intersections (Fig. 2a, interpreted faults). As deformation proceeds, new secondary faults propagate outwards from the highly deformed knee-points of L-shaped intersections, leading to Y-shaped geometries (Fig. 2a). Since faults of each system abut against faults of the other, T-shaped and L-shaped intersections are oriented along the N-S and the E-W axes of the model. The presence of T-shaped and L-shaped intersections oriented along both axes of the model is a diagnostic feature of synchronous bidirectional extension with respect to two-phase extension, where 2nd phase-faults abut systematically against 1st phase-faults, resulting in T-shaped intersections all oriented along the same axis (Supplementary Figure 2).

Whilst in two-phase extension 1st phase-faults strongly constrain the development of 2nd phase-faults, in synchronous bidirectional extension the two fault systems appear to influence each other to the same extent, developing broadly simultaneously in identical conditions. In particular, the development of a fault perpendicular to an extension direction is generally accompanied by the nearby nucleation of a new fault oriented perpendicular to the other extension direction (Fig. 2b). As new faults develop, the old ones remain active, with faults of both systems being active simultaneously during the whole experiment. The simultaneous activity of the two fault systems favours the transfer of displacement at fault intersections (Mouslopoulou *et al.*, 2007), resulting in preferential development of T-shaped and L-shaped intersections with respect to X-shaped intersections (Fig. 2a, histogram of intersection types). Although the two extension directions act simultaneously, the alternating nucleation of N-S- and E-W-striking faults suggests that one extension direction alternatively prevails over the other, with an oscillation of the local strain field (Fig. 2b). In contrast, the global strain field remains broadly stable and symmetrical during the experiment (Fig. 2b), suggesting that the oscillation of the local strain field likely reflects the interaction between adjacent faults.

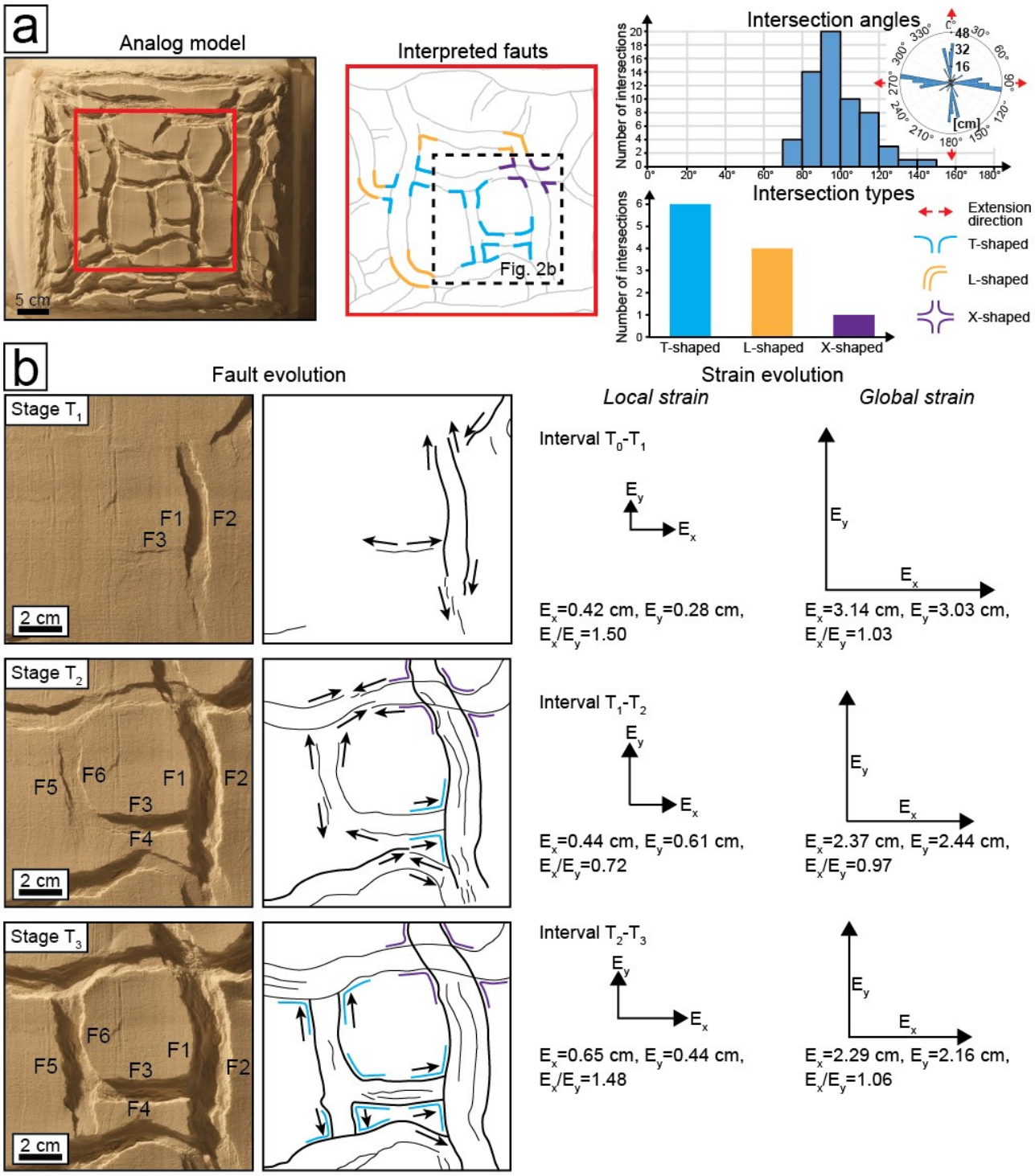

Fig. 2 Analogue model of faulting under synchronous bidirectional extension. a, Final-stage fault pattern, with analysis of the intersection style (intersection angle and geometry). Fault geometries were analysed in the central part of the model delimited by the red square. Faults intersect each other approximately at 90°, producing preferentially T-shaped and L-shaped intersections. **b**, Faults evolution, with quantification of the local and global deformation. The alternated development of perpendicular faults reflects the oscillation of the dominant extension direction at the local scale, which contrasts with a symmetrical and stable global strain field.

To re-equilibrate the local strain field with the global strain field, the development of a fault triggers the nucleation of new faults that accommodate the other component of the extension, thereby favouring the development of perpendicular faults and hindering the development of parallel faults. Whilst in a 2D strain field the activity of a fault causes an overall stress drop in the adjacent region (Gupta and Scholz, 2000), it appears that in a 3D strain field the stress drop is "direction sensitive", affecting only the component of the extension perpendicular to the fault. The interaction between faults through their local stress field represents a robust, self-sustaining process, which could potentially propagate across wide areas.

3. Comparison to natural examples

To test the effective occurrence of the deformation processes observed in our experiments, we compared their final fault geometries to natural examples. We selected tectonic settings under the simultaneous influence of different rift systems, and thus different extension directions, which can most likely host 3D strain fields.

3.1. Afar Depression

The Afar Depression is at the triple junction between the Gulf of Aden, Red Sea and East African rifts (Fig. 3a; *e.g*. Mckenzie *et al.*, 1970; Mohr, 1983). At present day, two main structural domains can be distinguished, with the Tendaho Goba'ad Discontinuity (TGD) separating an area under the influence of the NE-SW-directed Africa-Arabia extension to the north from an area controlled by the NW-SE-directed Nubia-Somalia extension to the south (Fig. 3a; Ebinger and Hayward, 1996; Hayward and Ebinger 1996).

However, a variety of structural trends passing one into the other suggests spatial and temporal variation of the main extension direction, reflecting a complex interplay between the three rifts of the triple junction (Tesfaye *et al.*, 2003; Wolfenden *et al.*, 2004). In particular, the NE-SW Africa-Arabia motion associated with the Gulf of Aden/Red Sea rift system has been shown to have a far-field influence on the stress field in southern Afar, with the development of a dike along a WNW-ESE direction captured in real time in 2000 (Keir *et al.*, 2011). The development of this anomalously oriented dike in an area under the main influence of the East African Rift (Beyene and Abdelsalam, 2005) indicates that the extension directions associated with the different rift systems can act simultaneously on the same area, possibly interacting with each other.

Similarly, in the central part of Afar curvilinear faults suggest a complex strain field, subject also to other influences beyond the NE-SW Africa-Arabia motion. In particular, 100 km north of the

Tendaho Goba'ad Discontinuity fault geometries display a strong similarity with our experiments on radial extension, with a major curvilinear graben (the Immino graben) intersecting minor, approximately perpendicular normal faults in the point of maximum curvature (Figs. 3b and c). The gradual transition between the different fault trends suggests that the curvilinear and the straight faults developed as a coupled system, expression of a sole and most likely radial strain field. The onset of a radial strain field may reflect the interaction between the three rift systems with their respective extension directions acting simultaneously and merging together. Despite this radial component, the NE-SW Africa-Arabia motion appears to have a major influence over the strain field in this part of Afar, with the Immino graben elongated approximately on a WNW-ESE direction (Fig. 3b).

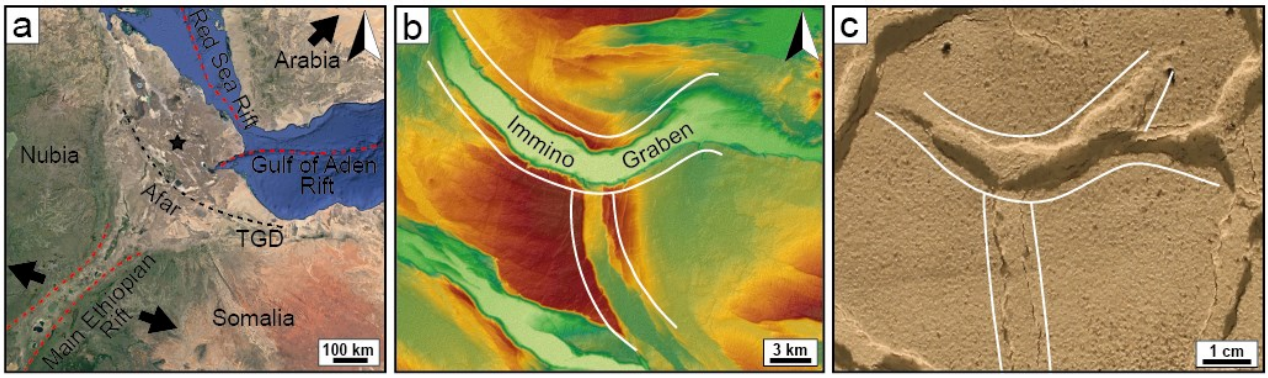

Fig. 3 Evidence for radial extension in the Afar Depression. a, Location of Afar at the intersection between the Red Sea, Gulf of Aden and East African rifts. TGD, Tendaho Goba'ad Discontinuity. The black star indicates the location of the study area in **b**. **b**, **c**, Similarity between fault geometries in a digital elevation model (from Shuttle Radar Topography Mission-SRTM) (**b**) and analogue models (**c**). In both cases, a major curvilinear graben is intersected by minor normal faults in its point of maximum curvature.

3.2. Barents Sea

The Barents Sea is a rift-shear margin resulting from the interaction between the Atlantic and Arctic oceans (*e.g.* Faleide *et al.*, 1993; Faleide *et al.*, 2008; Fig. 4a), whose rifting and later break-ups occurred largely simultaneously during the late Mesozoic-Cenozoic (Faleide *et al.*, 1993). During this time interval, two nearly perpendicular fault systems developed at the regional scale, with WNW-ESE (Osmundsen *et al.*, 2014; Collanega *et al.*, 2017; Mulrooney *et al.*, 2017) and N-S to NNE-SSW faults (Blaich *et al.*, 2017; Collanega *et al.*, 2017) suggested to respond to the influence of the Arctic and the Atlantic rifts respectively (Serck *et al.*, 2017). As rifting progressed, these fault systems were reactivated several times (Serck *et al.*, 2017) with activity phases varying in different sectors of the Barents Platform (*cf.* Blaich *et al.*, 2017; Mulrooney *et al.*, 2017; Serck *et al.*, 2017), indicating temporal and spatial variations of the main extension direction. Such instability of the stress field has been suggested to reflect a complex interaction between the Atlantic and the Arctic rifts (Serck *et al.*, 2017).

Three-dimensional seismic data from a shallow-depth area of the Barents Sea reveal that WNW-ESE and NNE-SSW faults have very similar geometries to those of our experiment on synchronous bidirectional extension (Figs. 4b and c). In particular, we note that the predominant intersection style between faults is represented by L-shaped and T-shaped intersections oriented along both axes of the model, which are diagnostic features of synchronous bidirectional extension with respect to two-phase extension (*cf.* Fig. 2 and Supplementary Figure 2).

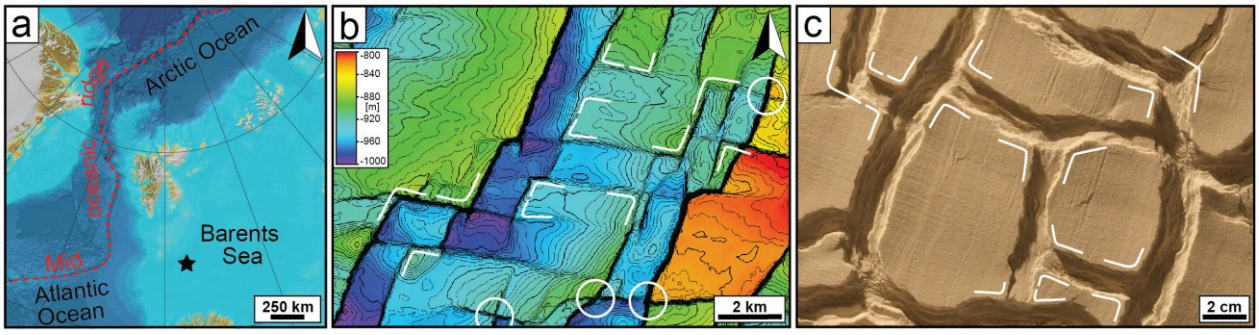

Fig. 4 Evidence for synchronous bidirectional extension in the Barents Sea. a, Location of the Barents along the rift-shear margin between the Atlantic and the Arctic oceans. The black star indicates the location of the study area in **b**. **b**, **c**, Similarity between fault geometries on a 3D seismic surface (**b**) and in analogue models (**c**) In both cases, two approximately perpendicular fault systems abut against each other, producing preferentially T-shaped and L-shaped intersections. However, in the natural example (**b**) WNW-ESE and NNE-SSW faults occasionally crosscut each other, producing X-shaped intersections (indicated by the white circles).

We thus suggest that the extension directions of the Atlantic and the Arctic rifts, at least periodically, acted simultaneously producing a 3D strain field with a synchronous bidirectional extension. As the Atlantic rift became dominant due to its proximity (Collanega *et al.*, 2017; Serck *et al.*, 2017), the NNE-SSW faults may have propagated laterally crosscutting occasionally the WNW-ESE faults (Fig. 4b, white circles), with originally T-shaped intersections evolving into X-shaped intersection.

4. Dynamics of 3D strain fields

3D strain fields have been previously thought as spatially homogeneous and temporally stable (Reches, 1978; 1983). Our work highlights a strong spatial and temporal instability of 3D deformation, with an extension direction prevailing over the others at the local scale even in stable and symmetrical 3D strain fields. The local strain field, and thus the final fault geometries, appears to reflect the interactions between adjacent faults more than the regional strain field. Indeed, our models show that a developing fault affects the strike of new faults nucleating nearby, favouring the development of new perpendicular faults. A similar effect has been observed for new faults propagating outwards from reactivated structures, which strike perpendicularly to the pre-existing structures rather than to the regional extension direction (Henza *et al.*, 2010; Duffy *et al.*, 2015; Withjack *et al.*, 2017; Deng *et al.*, 2018). These fault geometries suggest that in complex strain fields, the stress drop associated to the development of a fault affects only the component of the extension that is accommodated by that fault. This direction-sensitive stress drop results in a spatially and temporally variable local strain field, with the activities of adjacent faults compensating each other. Our work demonstrates that a 3D deformation can be accommodated by a series of interacting normal faults that strike perpendicularly to the local extension direction, thus behaving according to the Mohr-Coulomb theory.

The similarity between our models and natural examples suggests that tectonic settings under the simultaneous influence of different rift systems are prone to the onset of 3D strain fields. In particular, in the Afar Triple Junction the interaction of three different rift systems resulted in radial extension; whereas in the Barents Sea rift-shear margin the two extension directions of the Arctic and the Atlantic rifts remained distinct. Hence, the number and the geometry of the intersecting rift systems seem to control the symmetry of the strain field.

5. Supplementary materials

5.1. Methods

To reproduce a 3D strain field, it is necessary that at least two extension directions act simultaneously on a model. In 2D deformation experiments, the extension is generally applied through moving basal plates resulting in velocity discontinuities, which tend to localise the deformation and affect the stress field in a dominant way (Morley, 1999; Corti, 2012). Such localisation of deformation represents a major challenge when attempting to reproduce a 3D strain field, as it favours the onset of distinct areas subjected either to an extension direction or to the other but not to both of them. To overcome this issue, we used gravity-driven extension experiments (Supplementary Figure 1a; Gartrell, 1997, 2001; Vendeville *et al.*, 1987), where extension is achieved by the gravitational spreading of a ductile basal layer without introducing velocity discontinuities, therefore resulting in a distributed deformation.

We constructed simple, two-layer models by using a mixture of quartz and K-feldspar sand (70:30% in weight, grain size <250 μm, angle of internal friction of ~39°, cohesion of ~65 Pa and density of ~1,55 g/cm^3; Montanari *et al.*, 2017) and transparent silicone (Polydimetilsiloxane, PDMS) for the upper brittle layer and the basal ductile layer, respectively (Supplementary Figure 2a). Under the experimental conditions (i.e. low strain rate), PDMS exhibits a newtonian behaviour with viscosity of 2×10^4 Pa·s and density of 0.96 g/cm^3 (Weijermars, 1986). Hence, in free conditions PDMS flows away from the model centre to the margins, resulting in widespread deformation of the upper brittle sand layer (Gartrell, 1997, 2001). As PDMS tends to flow perpendicularly to the model boundaries in order to minimise the dissipation of energy, by creating models with different shapes it was possible to constrain the flow and, thus, the strain field. In particular, we created (i) a circular model, which extended equally along each radial direction giving an isotropic radial strain field and (ii) a square model, which equally extended perpendicularly to each model side with the onset of synchronous bidirectional extension (Supplementary Figure 2b). To keep the strain field stable during the experiments we cut regularly PDMS along the edges of the models, preserving their original shapes.

The tendency of PDMS to develop a circular shape (due to the surface tension of fluids) resulted in a gradient of extension along the sides of the square model, with maximum extension at the mid points and minimum extension at the vertices (Supplementary Figure 2b). However, the development of straight grabens parallel to the model sides (Fig. 2) implies that the extension

gradient, or at least its effects on the fault geometries, were negligible in the central part of the model, which is the base for all the considerations made in this work.

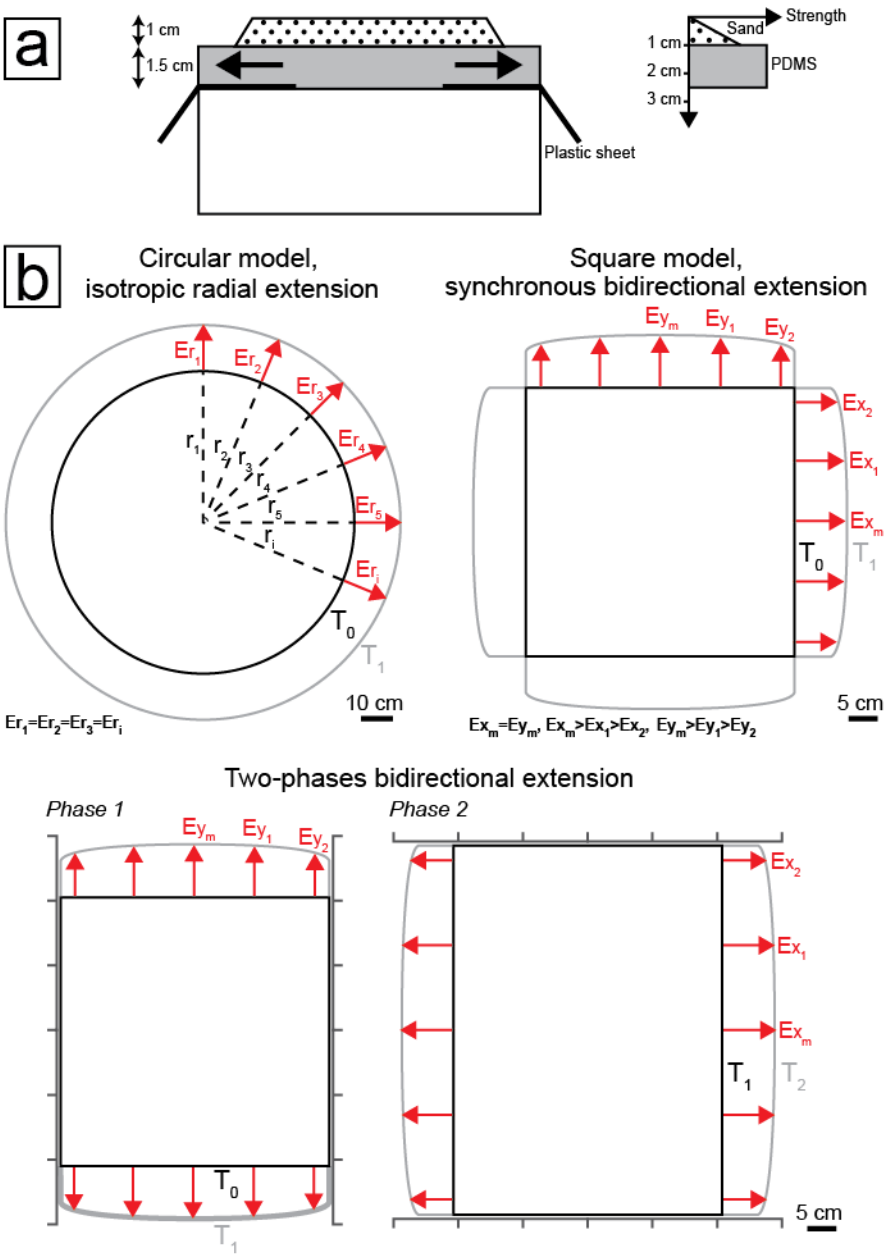

Fig. 1 Experimental set-ups. a, schematic cross-section of the experimental set-ups and corresponding strength profile. **b**, schematic top-views of the three experimental set-ups investigated. Red arrows indicate the extension at the model boundaries (the length of the arrows has been exaggerated to highlight the evolution of the model). The natural tendency of PDMS to flow perpendicularly to the model boundaries has been exploited to reproduce different strain fields by creating models of different shapes.

To identify diagnostic geometries of synchronous bidirectional extension, we reproduced also two-phase extension in models having the same shape, size and mechanical layering as the previous ones, and we compared the final fault patterns. We forced the lateral flow of PDMS along a specific direction by putting lateral barriers on two opposite sides of the model (1st deformation phase); then, we moved the lateral barriers to the other sides of the model, forcing the PDMS to flow on the direction perpendicular to the previous one (2nd deformation phase; Supplementary Figure 2b). To record the evolution of the faults we took sequential photographs of the top of the models during deformation. Once the faults reached their final stage, we determined their strike and intersection angle using ArcGIS. Finally, we measured the extension by way of markers on the model surface to quantify the local and the global deformation of the model.

5.2. *Supplementary Figure 2*

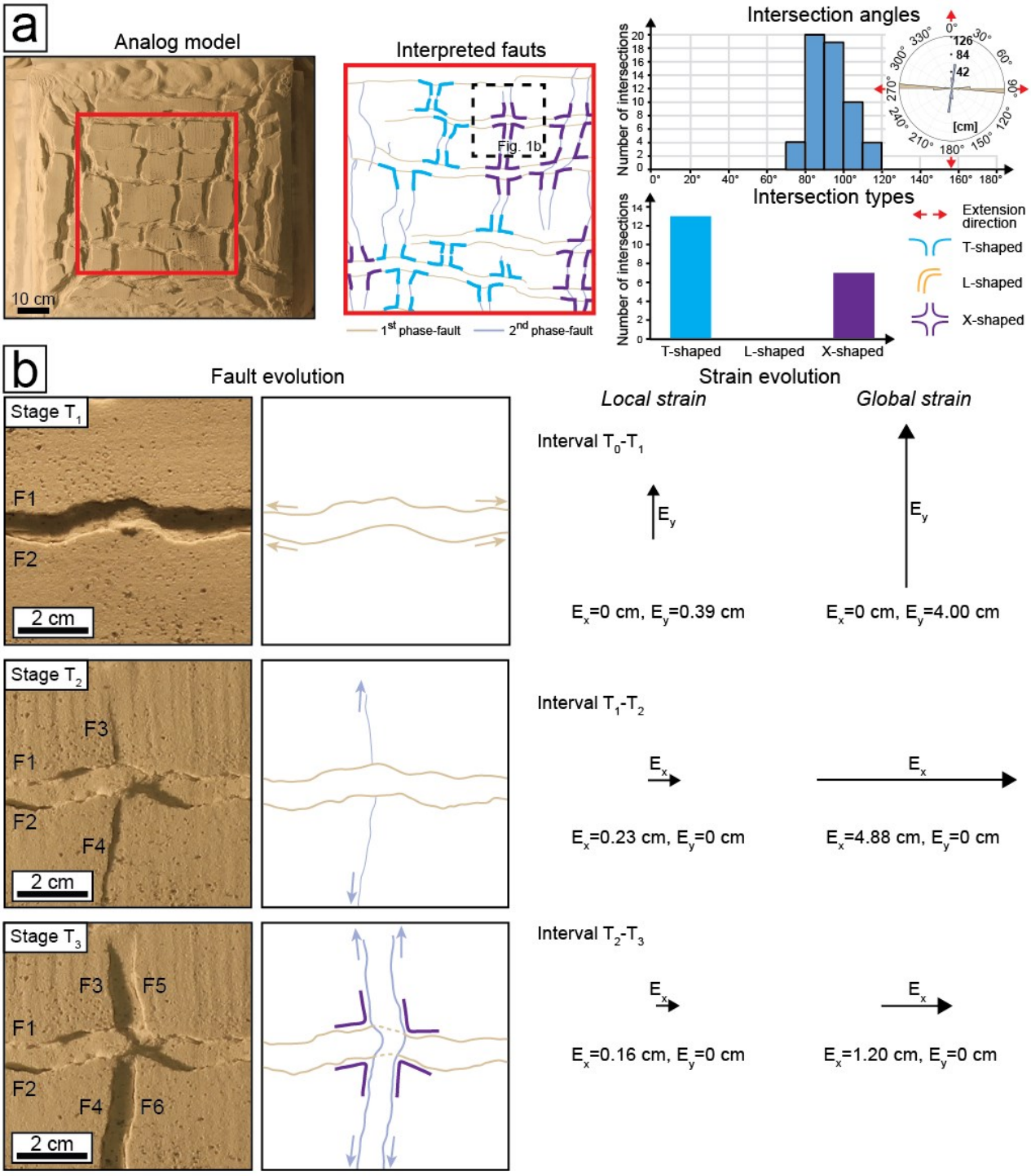

Fig. 2 Analogue model of faulting under two-phase extension. a, Final-stage fault pattern, with analysis of the intersection style (intersection angle and geometry). Fault geometries were analysed in the central part of the model delimited by the red square. Second-phase faults systematically terminate against and occasionally crosscut first-phase faults, producing T-shaped and X-shaped intersections. **b**, Fault evolution, with quantification of the local and global deformation. Second-phase faults initially terminate against first-phase faults (stage T_2), crosscutting them with increasing amount deformation (stage T_3).

References

Anderson, E.M., 1951. The Dynamics of Faulting. Oliver and Boyd, London, (183 pp.).

Beyene, A., Abdelsalam, M.G., 2005. Tectonics of the Afar Depression: A review and synthesis. Journal of African Earth Sciences 41, 41–59. https://doi.org/10.1016/j.jafrearsci.2005.03.003

Blaich, O.A., Tsikalas, F., Faleide, J.I., 2017. New insights into the tectono-stratigraphic evolution of the southern Stappen High and its transition to Bjørnøya Basin, SW Barents Sea. Marine and Petroleum Geology 85, 89–105. https://doi.org/10.1016/j.marpetgeo.2017.04.015

Collanega, L., Massironi, M., Breda, A., Kjølhamar, B.E., 2017. Onset of N-Atlantic rifting in the Hoop Fault Complex (SW Barents Sea): An orthorhombic dominated faulting? Tectonophysics 706–707, 59–70. https://doi.org/10.1016/j.tecto.2017.04.003

Corti, G., 2012. Evolution and characteristics of continental rifting: Analog modeling-inspired view and comparison with examples from the East African Rift System. Tectonophysics 522–523, 1–33. https://doi.org/10.1016/j.tecto.2011.06.010

Deng, C., Gawthorpe, R.L., Fossen, H., Finch, E., 2018. How Does the Orientation of a Preexisting Basement Weakness Influence Fault Development During Renewed Rifting? Insights From Three-Dimensional Discrete Element Modeling. Tectonics 37, 2221–2242. https://doi.org/10.1029/2017TC004776

Ebinger, C.J., Hayward, N.J., 1996. Soft plates and hot spots: Views from Afar. Journal of Geophysical Research: Solid Earth 101, 21859–21876. https://doi.org/10.1029/96JB02118

Faleide, J.I., Tsikalas, F., Breivik, A.J., Mjelde, R., Ritzmann, O., Engen, Ø., Wilson, J., Eldholm, O., 2008. Structure and evolution of the continental margin off Norway and the Barents Sea. Episodes 31, 82–91.

Faleide, J.I., Vågnes, E., Gudlaugsson, S.T., 1993. Late Mesozoic-Cenozoic evolution of the south-western Barents Sea in a regional rift-shear tectonic setting. Marine and Petroleum Geology 10, 186–214. https://doi.org/10.1016/0264-8172(93)90104-Z

Gartrell, A.P., 2001. Crustal rheology and its effect on rift basin styles. In: Koyi, H.A., Mancktelow, N.S. (Eds.), Tectonic modeling: A Volume in Honor of Hans Ramberg, Memoir – Geological Society of America, 193, pp. 221-233.

Gartrell, A.P., 1997. Evolution of rift basins and low-angle detachments in multilayer analog models. Geology 25, 615. https://doi.org/10.1130/0091-7613(1997)025<0615:EORBAL>2.3.CO;2

Gupta, A., Scholz, C.H., 2000. A model of normal fault interaction based on observations and

theory. Journal of Structural Geology 22, 865–879. https://doi.org/10.1016/S0191-8141(00)00011-0

Hayward, N.J., Ebinger, C.J., 1996. Variations in the along-axis segmentation of the Afar Rift system. Tectonics 15, 244–257. https://doi.org/10.1029/95TC02292

Healy, D., Blenkinsop, T.G., Timms, N.E., Meredith, P.G., Mitchell, T.M., Cooke, M.L., 2015. Polymodal faulting: Time for a new angle on shear failure. Journal of Structural Geology 80, 57–71. https://doi.org/10.1016/j.jsg.2015.08.013

Henza, A.A., Withjack, M.O., Schlische, R.W., 2011. How do the properties of a pre-existing normal-fault population influence fault development during a subsequent phase of extension? Journal of Structural Geology 33, 1312–1324. https://doi.org/10.1016/j.jsg.2011.06.010

Henza, A.A., Withjack, M.O., Schlische, R.W., 2010. Normal-fault development during two phases of non-coaxial extension: An experimental study. Journal of Structural Geology 32, 1656–1667. https://doi.org/10.1016/j.jsg.2009.07.007

Keep, M., McClay, K.R., 1997. Analogue modelling of multiphase rift systems. Tectonophysics 273, 239–270. https://doi.org/10.1016/S0040-1951(96)00272-7

Keir, D., Pagli, C., Bastow, I.D., Ayele, A., 2011. The magma-assisted removal of Arabia in Afar: Evidence from dike injection in the Ethiopian rift captured using InSAR and seismicity. Tectonics 30, n/a-n/a. https://doi.org/10.1029/2010TC002785

McClay, K.R., White, M.J., 1995. Analogue modelling of orthogonal and oblique rifting. Marine and Petroleum Geology 12, 137–151. https://doi.org/10.1016/0264-8172(95)92835-K

Mckenzie, D.P., Davies, D., Molnar, P., 1970. Plate Tectonics of the Red Sea and East Africa. Nature 226, 243–248. https://doi.org/10.1038/226243a0

Mohr, P., 1983. Ethiopian flood basalt province. Nature 303, 577–584. https://doi.org/10.1038/303577a0

Montanari, D., Agostini, A., Bonini, M., Corti, G., Ventisette, C., 2017. The Use of Empirical Methods for Testing Granular Materials in Analogue Modelling. Materials 10, 635. https://doi.org/10.3390/ma10060635

Morley, C.., 1999. How successful are analogue models in addressing the influence of pre-existing fabrics on rift structure? Journal of Structural Geology 21, 1267–1274. https://doi.org/10.1016/S0191-8141(99)00075-9

Mouslopoulou, V., Nicol, A., Little, T.A., Walsh, J.J., 2007. Displacement transfer between intersecting regional strike-slip and extensional fault systems. Journal of Structural

Geology 29, 100–116. https://doi.org/10.1016/j.jsg.2006.08.002

Mulrooney, M.J., Leutscher, J., Braathen, A., 2017. A 3D structural analysis of the Goliat field, Barents Sea, Norway. Marine and Petroleum Geology 86, 192–212. https://doi.org/10.1016/j.marpetgeo.2017.05.038

Osmundsen, P.T., Braathen, A., Rød, R.S., Hynne, I., Mørk, A., 2014. Styles of normal faulting and fault-controlled deposition in the Triassic of Hopen and Edgeøya, Svalbard. Norwegian Petroleum Directorate Bulletin 11, 61–79.

Reches, Z., 1983. Faulting of rocks in three-dimensional strain fields II. Theoretical analysis. Tectonophysics 95, 133–156. https://doi.org/10.1016/0040-1951(83)90264-0

Reches, Z., 1978. Analysis of faulting in three-dimensional strain field. Tectonophysics 47, 109–129. https://doi.org/10.1016/0040-1951(78)90154-3

Serck, C.S., Faleide, J.I., Braathen, A., Kjølhamar, B., Escalona, A., 2017. Jurassic to Early Cretaceous basin configuration(s) in the Fingerdjupet Subbasin, SW Barents Sea. Marine and Petroleum Geology 86, 874–891. https://doi.org/10.1016/j.marpetgeo.2017.06.044

Stein, R.S., 1999. The role of stress transfer in earthquake occurrence. Nature 402, 605–609. https://doi.org/10.1038/45144

Tesfaye, S., Harding, D.J., Kusky, T.M., 2003. Early continental breakup boundary and migration of the Afar triple junction, Ethiopia. Geological Society of America Bulletin 115, 1053. https://doi.org/10.1130/B25149.1

Toda, S., Stein, R.S., Beroza, G.C., Marsan, D., 2012. Aftershocks halted by static stress shadows. Nature Geoscience 5, 410–413. https://doi.org/10.1038/ngeo1465

Vendeville, B., Cobbold, P.R., Davy, P., Choukroune, P., Brun, J.P., 1987. Physical models of extensional tectonics at various scales. Geological Society, London, Special Publications 28, 95–107. https://doi.org/10.1144/GSL.SP.1987.028.01.08

Weijermars, R., 1986. Flow behaviour and physical chemistry of bouncing putties and related polymers in view of tectonic laboratory applications. Tectonophysics 124, 325–358. https://doi.org/10.1016/0040-1951(86)90208-8

Withjack, M.O., Henza, A.A., Schlische, R.W., 2017. Three-dimensional fault geometries and interactions within experimental models of multiphase extension. AAPG Bulletin 101, 1767–1789. https://doi.org/10.1306/02071716090

Withjack, M.O., Jamison, W.R., 1986. Deformation produced by oblique rifting. Tectonophysics 126, 99–124. https://doi.org/10.1016/0040-1951(86)90222-2

Wolfenden, E., Ebinger, C., Yirgu, G., Deino, A., Ayalew, D., 2004. Evolution of the northern

Main Ethiopian rift: birth of a triple junction. Earth and Planetary Science Letters 224, 213–228. https://doi.org/10.1016/j.epsl.2004.04.022

PAPER 3

Submitted to *Basin Research* 3 June 2018, received in revised form 31 October 2018, accepted 3 November 2018, available online 11 November 2018

NORMAL FAULT GROWTH INFLUENCED BY BASEMENT FABRICS: THE IMPORTANCE OF PREFERENTIAL NUCLEATION FROM PRE-EXISTING STRUCTURES

Luca Collanega[1], Christopher A-L. Jackson[2], Rebecca E. Bell[2], Alexander J. Coleman[2], Antje Lenhart[2], Anna Breda[1]

[1]Dipartimento di Geoscienze, University of Padova, Via G. Gradenigo, 6, 35131 Padova, Italy

[2]Basins Research Group (BRG), Department of Earth Science and Engineering, Imperial College, London, SW7 2BP, UK

Corresponding author: luca.collanega@gmail.com

doi: 10.1111/bre.12327

Luca Collanega did the entire seismic interpretation work and kinematic analysis, wrote the first version of the manuscript and drafted all the figures. Christopher A-L. Jackson, Rebecca E. Bell designed the general structure of the paper and edited the final manuscript. Alexander J. Coleman contributed to the interpretation of the kinematic analysis and gave helpful comments on the manuscript. Antje Lenhart offered important discussions on the interpretation of the intra-basement structures. Anna Breda contributed to the preliminary discussions and to the general structure of the paper.

ABSTRACT

Pre-existing intra-basement structures can have a strong influence on the evolution of rift basins. Although 3D geometric relationships provide some insight into how intra-basement structures determine the broad geometry and spatial development (e.g. strike and dip) of rift-related faults, little is known about the impact of the former on the detailed kinematics (i.e. nucleation and tip propagation) of the latter. Understanding the kinematic as well as geometric relationship between intra-basement structures and rift-related fault networks is important, with the extension direction in many rifted provinces typically thought to lie normal to fault strike. We here investigate this problem using a borehole-constrained, 3D seismic reflection dataset from the Taranaki Basin, offshore New Zealand. Excellent imaging of intra-basement structures and a relatively weakly-deformed, stratigraphically simple sedimentary cover allow us to: (i) identify a range of interaction styles between intra-basement structures and overlying, Plio-Pleistocene rift-related normal faults; and (ii) examine the cover fault kinematics associated with each interaction style. Some of the normal faults parallel and are physically connected to intra-basement reflections, which are interpreted as mylonitic thrusts related to Mesozoic subduction and basement terrane accretion. These geometric relationships indicate pre-existing, intra-basement fabrics locally controlled the position and attitude of Plio-Pleistocene rift-related normal faults. However, through detailed 3D kinematic analysis of selected normal faults, we show that: (i) normal faults only nucleated above intra-basement structures that experienced Late Miocene compressional reactivation; (ii) thrusts and folds resulting from Late Miocene reactivation and upward propagation of intra-basement structures acted as nucleation sites for Plio-Pleistocene rift-related faults; and (iii) despite playing an important role during rifting, intra-basement structures do not appear to have been significantly extensionally reactivated. Our analysis shows how km-wide, intra-basement structures can have a temporally and spatially far-reaching influence over the nucleation and development of newly formed normal faults, most likely related to a local perturbation of the regional stress field. Because of this, simply inverting fault strike for causal extension direction may be incorrect, especially in provinces where pre-existing, intra-basement structures occur. We also show that a detailed kinematic analysis is key to deciphering the temporal as well as simply spatial or geometric relationship between structures developed at multiple structural levels.

1. Introduction

Crystalline basement typically hosts a variety of mechanical anisotropies consisting of structures at different scales; e.g. metamorphic mineral fabrics, brittle faults, fracture networks, ductile shear zones, and major tectonic boundaries. Pre-existing structures may control the strike and distribution of normal faults developed during rifting, resulting in the formation of non-colinear fault networks (e.g. Korme *et al.*, 2004; Morley *et al.*, 2004; Reeve *et al.*, 2015). However, non-colinear fault systems may also form in response to multiphase rifting (e.g. Keep and McClay, 1997**;** Morley *et al*., 2007; Henza *et al.***,** 2010**;** Whipp *et al.*, 2014; Duffy *et al.*, 2015), the breaching of relay zones bound by otherwise co-linear faults (e.g. Trudgill, 2002), the development of release faults (e.g. Destro, 1995), or local stress perturbation around major faults (Maerten *et al.*, 2002). Understanding the causal mechanism underlying the formation of non-colinear faults is crucial when attempting to infer and reconstruct the stresses and overall tectonic history of an area (cf. Henza *et al.*, 2010; Peace *et al.*, 2017). Intra-basement structures can affect large-scale rift development, as recognized in both conjugate margins of the North Atlantic Rift System (e.g. Bartholomew *et al.*, 1993; Doré *et al.*, 1997; Gudlaugsson *et al.*, 1998; Henstra *et al.*, 2015; Fossen *et al.*, 2017 for the Norwegian margin and Rotevatn *et al.*, 2018 for the Greenland margin), the East African Rift (e.g. McConnel, 1969; McConnel, 1972**;** Corti *et al.*, 2007 and 2013), the rift basins of Thailand (Morley *et al.***,** 2004 and 2011; Morley, 2014 and 2017) and the Taranaki Basin (Muir *et al.*, 2000). Offshore-onshore correlations, combined with aeromagnetic data, suggest pre-existing basement structures can control the position of major basin-bounding fault systems, shaping the overall rift physiography (e.g. Muir *et al.*, 2000; Gernigon *et al.*, 2014; Fazlikhani *et al.*, 2017). However, the influence of basement fabrics is complex, with their orientation relative to the extension direction, strength, dip, spacing and type (pervasive or discrete) contributing to determine whether and to which extent they influence the overlying normal faults (Morley, 1995; Morley *et al.*, 2004).

Recently, 3D seismic reflection data have allowed the three-dimensional geometric relationships between intra-basement structures and normal faults to be resolved (e.g. Reeve *et al.*, 2013; Bird *et al.*, 2014; Morley 2014; Phillips *et al*., 2016). In particular, analysis of 3D seismic data from the North Sea show that intra-basement structures can be either reactivated or cross-cut by later normal faults, with dip and obliquity with respect to the new extension direction thought to be the key factors controlling their selective reactivation (Phillips *et al.*, 2016; Claringbould *et al.*, 2017; Fazlikhani *et al.*, 2017). However, pre-existing structures may exert their influence through other processes rather than simple reactivation, for example by acting as nucleation sites for later-formed normal faults (e.g. Henza *et al.*, 2010, 2011, Duffy *et al.,* 2015), or by perturbing the local stress field (e.g. Zhang *et al.*, 1994; Bell, 1996; Morley, 2010), resulting in normal faults striking obliquely to the dominant extension direction.

New normal faults may nucleate preferentially in the weak regions offered by pre-existing structures, even when pre-existing structures are not directly reactivated (Morley 1999; Morley *et al.*, 2004); such examples of this spatial and kinematic relationship are shown in the physical models of Faccenna *et al.* (1995), Henza *et al.* (2010), Henza *et al.* (2011), and the numerical models of Deng *et al.*, (2017). Furthermore, local stress perturbations near pre-existing structures are supported by inversion of earthquake focal mechanisms (Morley, 2010), analysis of borehole break-out data (King *et al.*, 2010; Tingay *et al.*, 2010), and the outputs of numerical models (Homberg *et al.*, 1997; Maerten *et al.*, 1999; Maerten *et al.*, 2002). Recently, Duffy *et al.* (2015) showed how the throw distribution on normal fault planes can be used to infer the kinematics of normal faults and their complex interaction styles in a multiphase rift setting. However, to the best of our knowledge, this powerful approach has not yet been applied to the interactions between intra-basement structures and overlying, rift-related normal fault networks.

In this study we: i) identify and characterise a range of three-dimensional geometric relationships between intra-basement structures and overlying normal faults; ii) use growth strata and fault displacement distribution mapping to perform a kinematic analysis of the normal faults; and iii) based on their geometric and kinematic relationships, interpret how intra-basement structures influenced the development of the rift-related normal faults. To do this we use 3D seismic reflection and well data from the western margin of the Taranaki Basin, offshore New Zealand (Fig. 1). The shallow depth of the crystalline basement (*c.* 3.5 km) results in excellent seismic imaging of the intra-basement structures; this, combined with a stratigraphically simple, relatively low-strain setting, makes this an ideal location to examine the early-stage interactions between intra-basement structures and overlying, rift-related normal faults. We first use qualitative, plan-view- and cross-section-based observations to show that, to the first-order, intra-basement structures controlled the growth of the later, rift-related normal fault network (Bird *et al.*, 2015; Peace *et al.*, 2017). We then conduct a quantitative, three-dimensional analysis of throw distributions on individual fault surfaces to understand how each interaction style evolved (cf. Duffy *et al.*, 2015). Our 3D kinematic analysis shows how preferential nucleation from pre-existing structures and local perturbation of the regional stress field can strongly influence the development of overlying rift-related normal fault network, resulting in characteristic spatial and temporal relationships between structures at different levels.

2. Geological framework

The Taranaki Basin is situated mostly offshore the west coast of New Zealand's North Island. The basin is defined by two major, approximately N-trending fault systems: the Cape Egmont and Taranaki faults (Fig. 1). Up to 8 km thick sedimentary cover records two rifting episodes in the Late Cretaceous-Early Eocene and Plio-Pleistocene respectively (Fig. 2A), with an intervening phase of contraction and basin inversion.

2.1. Basement geology

The basement structural grain of the Taranaki Basin developed during Mesozoic subduction and terrane accretion along the SW-Pacific margin of Gondwana (e.g. Bradshaw, 1989; Fig. 2A). By the Early Cretaceous, subduction had resulted in the juxtaposition of three approximately N-trending basement terranes (Bradshaw, 1993; Kimbrough *et al.*, 1993; Fig. 1): (i) the Western Province, consisting of a Gondwana fragment made up of mainly meta-sedimentary rocks (Bradshaw *et al.*, 1997; Mortimer *et al.*, 1997), (ii) the Eastern Province, comprising arc volcanic and arc-derived meta-sedimentary sequences (e.g. Bradshaw, 1989) and (iii) the Median Tectonic Zone, a narrow belt of plutonic rocks, which separates the Western and Eastern Provinces (e.g. Bradshaw, 1993; Mortimer *et al.*, 1999). This basement fabric influenced the subsequent structural evolution of the sedimentary cover during the Cenozoic, with the Cape Egmont and Taranaki Faults exploiting the boundaries between basement terranes (Muir *et al.*, 2000; Fig. 1). Our study area sits on the uplifted footwall of the Cape Egmont Fault, which corresponds to the eastern edge of the Western Province (Figs. 1 and 2B).

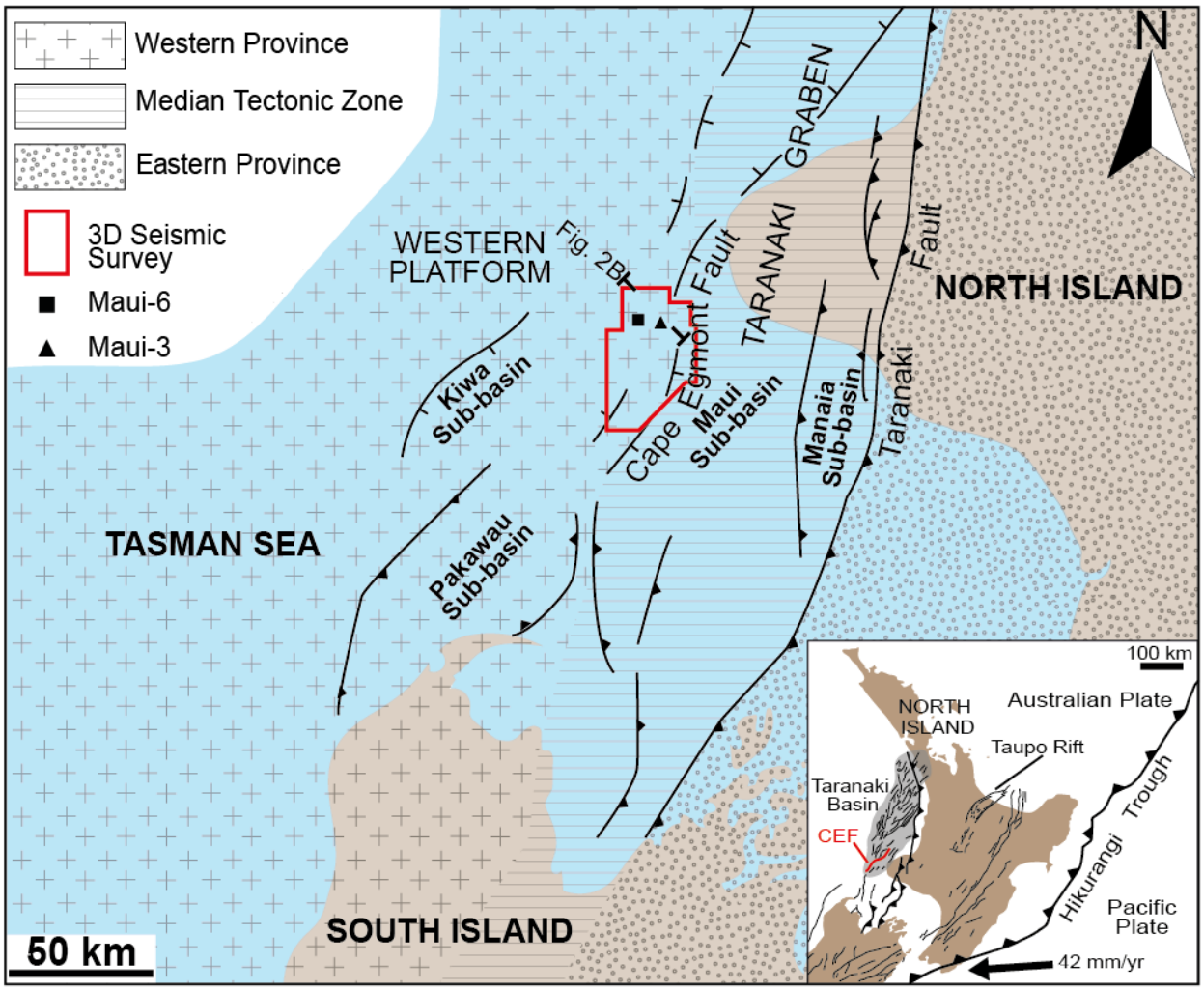

Fig. 1. Map illustrating the main structural elements of the Taranaki Basin (modified from Miur *et al.*, 2000). Underlying basement terranes are shown in grey. Note the plan-view correlation between the Cape Egmont Fault (CEF) and Taranaki Fault with the basement terrane boundaries. The red box indicates the location of the 3D seismic survey. Inset – plate tectonic setting of the Taranaki Basin. Note the location of the Taranaki Basin in the proximity of the Pacific Plate Subduction Zone (modified from Giba *et al.*, 2010). The black arrow indicates the relative plate motion vector of the Pacific Plate (from Beavan and Haines, 2001).

2.2. Structural evolution of the Southern Taranaki Basin

In the Late Cretaceous-Early Eocene, the Taranaki Basin initially evolved as an intra-plate rift related to the break-up of Gondwana, which was associated with thermally induced uplift and the development of a major regional unconformity at the top of the crystalline basement (Moore *et al.*, 1986; Strogen *et al.*, 2017). Normal faulting initiated in the Mid-Cretaceous and continued until the Paleocene, with the cessation of faulting being diachronous across the Taranaki Basin (Strogen *et al.*, 2017). This rift event formed a series of NE-trending half-graben (e.g. Maui Sub-basin, Pakawau Sub-basin, Kiwa Sub-basin) that filled with up to 1800 m of fluvial-deltaic-to-shallow marine sediments sourced from the adjacent fault scarps (North Cape and Farewell formations;

King and Thrasher, 1996; Fohrmann *et al.*, 2012; Reilly *et al.*, 2015; Strogen *et al.*, 2017). Once rifting ceased, post-rift thermal subsidence resulted in an overall deepening of the basin and the deposition of mudstone-dominated, marine sediments (Turi Formation; King and Thrasher, 1996; Strogen, 2011; Strogen *et al.*, 2014).

In the Mid-Eocene, in response to the onset of subduction of the Pacific Plate along the Hikurangi Trough, compression initiated at the eastern margin of the Taranaki Basin, resulting in an increase of crustal thickness from 26 km beneath the Western Platform to 40 km beneath the Taranaki Fault system (e.g. Holt and Stern, 1994; Stagpoole and Nicol, 2008; Stern and Davey, 1990). During the Miocene, compression spread westwards through the Taranaki Basin, with the inversion of the Cape Egmont Fault occurring in the late Miocene (Nicol *et al.*, 2005). Shortening was associated with the formation of NE-to-NNW-trending reverse faults and folds, which occasionally exploited pre-existing normal faults and basement fabric (Reilly *et al.*, 2015). In the Southern Taranaki Basin, compression was rapidly followed by back-arc extension at about 4 Ma, with this tectonic regime continuing to the present day (e.g. Giba *et al.*, 2010; Mouslopoulou *et al.*, 2012). The dominant strike of the Plio-Pleistocene rift-related normal faults is NE-SW, with NNE-SSW-striking normal faults prevailing west of the Cape Egmont Fault (Reilly *et al.*, 2015). This fault pattern is consistent with the current NW-SE regional extension direction indicated by borehole breakouts and focal mechanisms (Giba *et al.*, 2010). During Plio-Pleistocene rifting, reactivation and upward propagation of pre-existing, predominantly Late Cretaceous-to-Paleocene faults resulted in the formation of relatively small (in terms of displacement), N-S-striking segments (Giba *et al.*, 2012). Since the onset of rifting, the regional extension was relatively low (average total extension of ≈ 1.9 km and extension rate of ≈ 0.5 mm/year; Giba *et al.*, 2010; Reilly *et al.*, 2015) and was focussed on the Cape Egmont Fault (Reilly *et al.*, 2015), resulting in relatively mild deformation throughout the Southern Taranaki Basin.

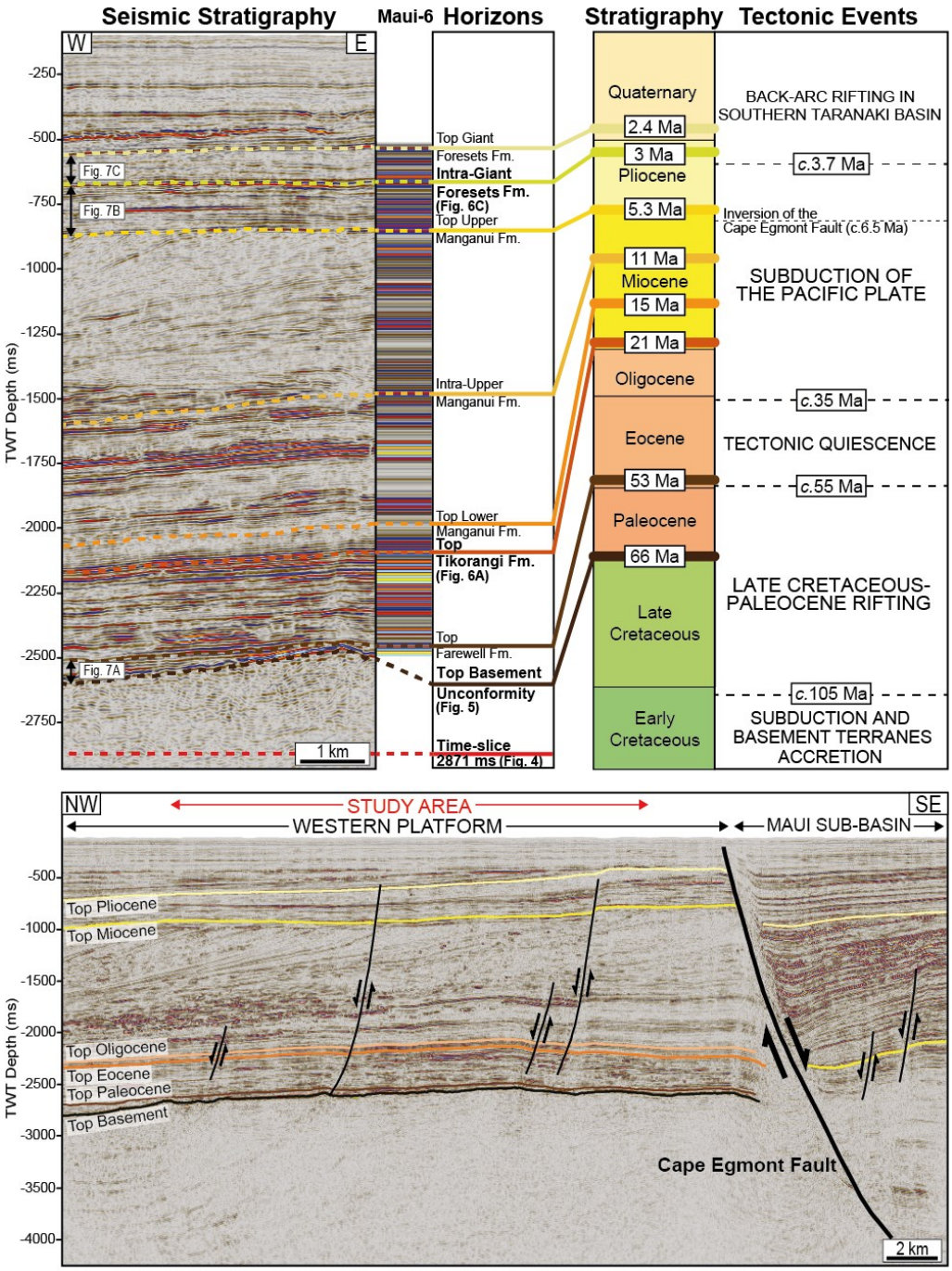

Fig. 2. Stratigraphic and structural setting of the study area. (A) Stratigraphic framework indicating the interpreted seismic reflection events. The Maui-6 synthetic seismogram, which was used to tie the seismic reflection data to stratigraphic data, is also shown. Seismic-stratigraphic packages are correlated to the major regional tectonic events, using biostratigraphic data provided in well Maui-3 (location of wells shown in Fig. 1). The stratigraphic position of key TWT-structure maps (i.e. Figs. 4, 5 and 6) and time-thickness maps (i.e. Fig. 7) presented in this study are also shown. (B) Regional seismic line showing the structural setting of the study area and the main stratigraphic units (location shown in Fig. 1; see Appendix A for enlarged uninterpreted and interpreted versions of this section). Note the position of the study area in the uplifted footwall of the Cape Egmont Fault and the low-strain, stratigraphically simple setting (stratigraphic correlation across the Cape Egmont Fault based on Nicol *et al.*, 2005).

3. Dataset

We use a 1500 km^2, pre-stack time-migrated, 3D seismic reflection dataset and seven wells (Appendix B), the latter containing well-log, formation top and biostratigraphic data. Two wells (Maui-2 and Rahi-1) penetrate the uppermost part of the crystalline basement. The 3D survey has a record length of 5500 ms two-way time (TWT), and a vertical sampling interval of 3 ms, with an inline (N-trending) and crossline (E-trending) spacing of 25 m and 12.5 m, respectively. Seismic data are presented with SEG normal polarity, such that trough events (blue reflections) correspond to a downward decrease in acoustic impedance and peak events (red reflections) correspond to a downward increase in acoustic impedance. The dominant frequency decreases downwards from *c.* 50 Hz in the Pliocene interval (c. 750 ms TWT) to *c.* 35 Hz in the shallow crystalline basement (c. 2700 ms TWT); taking velocity data for the sedimentary cover from wells, and by assuming a velocity of 5500 ms-1 for the crystalline basement based on its lithologic composition (i.e. metasedimentary rock; *cf.* Muir *et al.*, 2000), we estimate a downward decrease of the vertical seismic resolution from *c.* 10 m to 40 m.

4. Methods

To map the plan-view distribution of the intra-basement structures we used a seismic attribute sensitive to amplitude contrast (i.e. Root Mean Square or 'RMS' amplitude attribute), and one revealing the normalized dip of the reflections (i.e. Dip Illumination). We mapped the Top Basement and eight key seismic horizons across the survey area, tying them to wells using checkshots and synthetic seismograms (Fig. 2A). To constrain the onset of rift-related faulting, we created isochron (thickness) maps between the Top Basement and the Top Farewell Formation, the Top Upper Manganui and Intra-Giant Foresets formations, and the Intra-Giant Foresets and the Top Giant Foresets formations. (Fig. 2A). We compared the spatial distribution of intra-basement structures and normal faults at different stratigraphic levels, and evaluated their connectivity in cross-section, thereby revealing their three-dimensional geometric relationships.

To determine how each geometric relationship developed, we carefully reconstructed the 3D geometry of, and throw distribution on, key faults. We infer regions of high-displacement represent fault nucleation points, whereas local throw minima represent areas of fault linkage (Walsh and Watterson, 1987; Mansfield and Cartwright, 1996; Walsh *et al.*, 2003; Giba *et al.*, 2012). Throw distribution on the fault surface can thus be used to determine if the fault grew as a single, isolated structure, or whether it evolved through the coalescence of initially isolated segments. We mapped

faults on seismic sections taken orthogonal to fault strike at intervals of 62.5 m, paying particular attention to tip line position and degree of linkage with intra-basement structures. We determined the footwall and hanging wall cut-offs for 8-15 horizons to constrain throw variations on the fault surface. In addition, we calculated the ratio of hanging wall thickness to footwall thickness (i.e the Expansion Index; Hongxing and Anderson, 2007) for each interval delimited by two adjacent horizons. In order to remove the effect of fault-related folding, and to thus account for the continuous (ductile) component of strain, we projected the regional trend of horizon dip away from the fault-related folds (Appendix C). We displayed throw values as throw-depth (T-z) plots, where the throw is plotted against the depth to the midpoint between hanging-wall and footwall cut-offs (e.g. Muraoka and Kamata, 1983; Cartwright *et al.*, 1995; Hongxing and Anderson, 2007; Baudon and Cartwright, 2008a, b and c). From these data we compiled fault strike-projections (e.g. Walsh and Watterson, 1991; Duffy *et al.*, 2015). Finally, we converted our TWT kinematic analysis to the depth domain using a simple best-fit second-order polynomial relationship derived from the time-depth curves of two nearby wells (Appendix D). The measurement error imposed by well-derived velocity variations increases downwards from 10 m in the Pliocene interval to 190 m immediately above Top Basement. Given the simple velocity structure of the sedimentary cover, this error may influence the absolute throw values presented, but will not significantly influence the overall throw pattern on, or kinematic interpretation of, individual segments (cf. Baudon and Cartwright, 2008c; Conneally *et al.*, 2014; Duffy *et al.*, 2015). In addition, because of: (i) the stratigraphically simple, sub-horizontally layered nature of the host rock; and (ii) the relatively low throw values, meaning footwall and hangingwall strata are not buried to significantly different depths, we argue that primary throw distribution will not be substantially altered by ongoing and/or subsequent compaction or differential compaction (cf. Mansfield and Cartwright, 1996; Taylor *et al.*, 2008).

5. Interpretation of intra-basement structures

5.1. Types of intra-basement reflections

Intra-basement reflections are well-imaged within the upper ~1000 ms TWT of the basement rocks (c. 5500 m below Top Basement). The crystalline basement is generally acoustically transparent, with sub-horizontal reflections in the upper part (Figs. 3D and E). The most prominent features in the crystalline basement are medium-to-high amplitude, continuous to semi-continuous, gently west-dipping (15° to 30°) reflections defined by a peak-trough-peak wave train (Fig. 3). Based on their amplitude, spacing, and vertical and lateral continuity, these reflections can be subdivided into three types (Figs. 3C, D and E):

- Type 1 consists of a *c.* 2.5 km-wide zone of shallowly dipping (15°-20°) reflections (Fig. 3A). The seismic character changes laterally within this package, from high-amplitude, continuous reflections at the boundaries, to chaotic, discontinuous, folded reflections towards the centre. Type 1 reflections typically offset Top Basement (Fig. 3C).
- Type 2 is represented by narrow (*c.* <100 m-wide), isolated, high-amplitude reflections that dip at 20°-30° and have a lateral spacing of 1-2 km (Fig. 3B). Reflections are vertically continuous from the Top Basement to the survey record length (5500 ms). Although Type 2 reflections are generally associated with a fold in the overlying Paleocene succession, they do not generally offset the Top Basement (Fig. 3D).
- Type 3 has similar characteristics to Type 2, but the reflections are weaker and vertically segmented (<500 m long in the dip direction; Fig. 3E). Type 3 reflections are truncated by the Top Basement Unconformity and are overlain by flat-lying Paleocene strata (Fig. 3E).

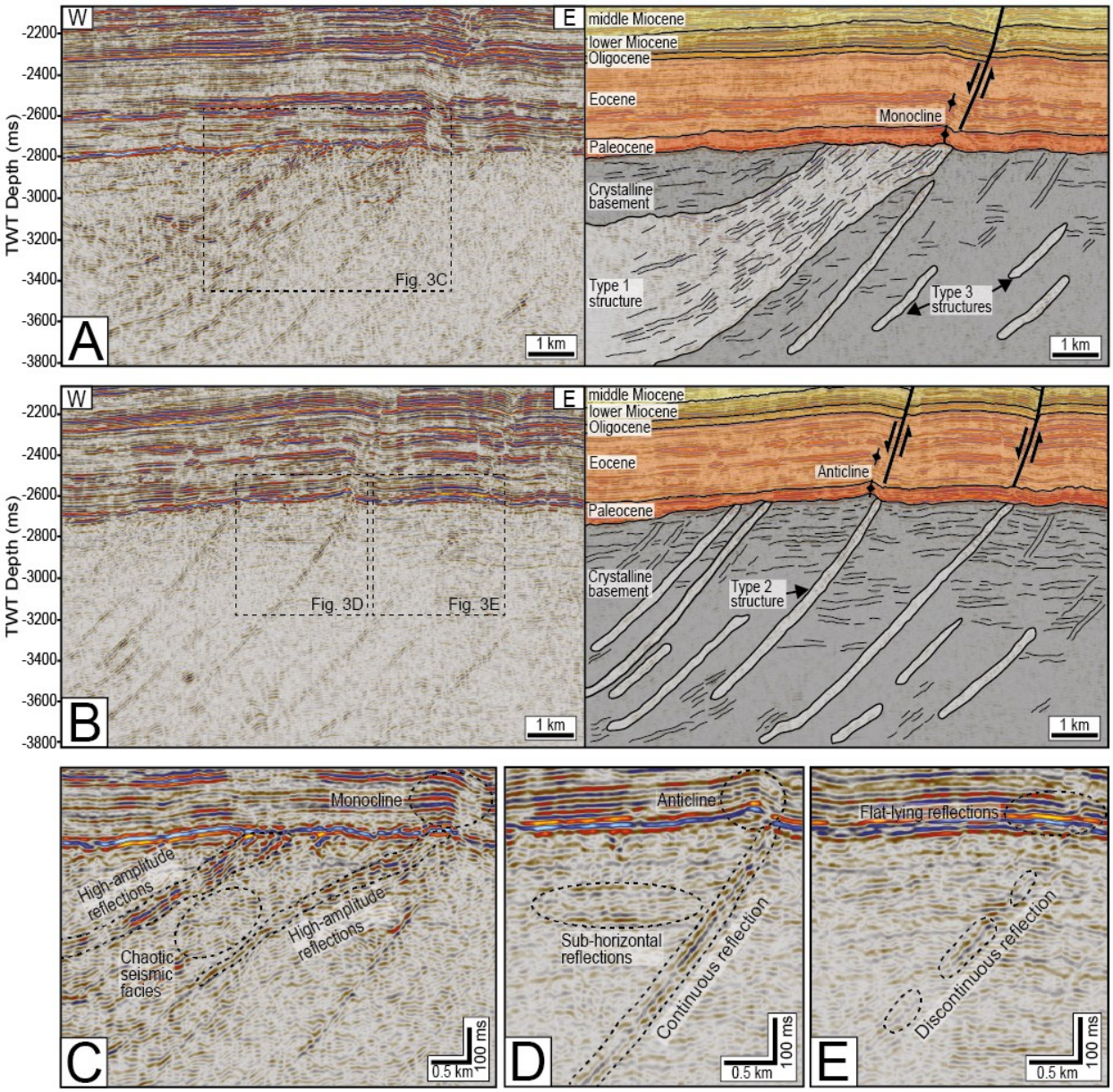

Fig. 3. Series of uninterpreted seismic profiles and geo-seismic sections illustrating the key characteristics of intra-basement reflections (locations of sections shown in Fig. 4C; see Appendix A for enlarged uninterpreted and interpreted versions of the sections). (A) Seismic and geo-seismic section oriented orthogonal to the Type 1 reflections in the northern part of the survey area. Note the linkage between the Type 1 reflections and the overlying normal fault. (B) Seismic and geo-seismic section oriented orthogonal to Type 2 and Type 3 reflections in the centre of the survey area. (C) Close-up of the Type 1 reflections. Note the high-amplitude reflections at the boundaries and the chaotic seismic facies towards the inner zone. (D) Close-up of a Type 2 reflection, which typically offset Top Basement and are often associated with an anticline. (E) Close-up of a Type 3 reflection. Note the flat-lying reflections above Top Basement.

5.2. Plan-view distribution

Type 1 reflections are only observed in a broadly N-trending, 5 km-long, 2.5 km-wide zone in the northern part of the survey (Fig. 4A). The eastern and western boundaries of this zone are relatively sharp. In contrast, the southern boundary is gradational, with several Type 2 reflections splaying off from the package of Type 1 reflections (Figs. 4B and C). Type 2 and Type 3 reflections are typically 1-15 km long, curvilinear (Fig. 4C), and trend NNW to NNE (see rose diagram in Fig. 4C). Type 2 reflections are concentrated in the central part of the survey (Fig. 4C) and are laterally continuous (Fig. 4B). In contrast, Type 3 reflections occur in the eastern and western sectors (Fig. 4C), and are segmented along strike (<3 km long segments; Fig. 4B). Type 2 and Type 3 reflections are often interconnected, displaying an anastomosing geometry (Fig. 4C).

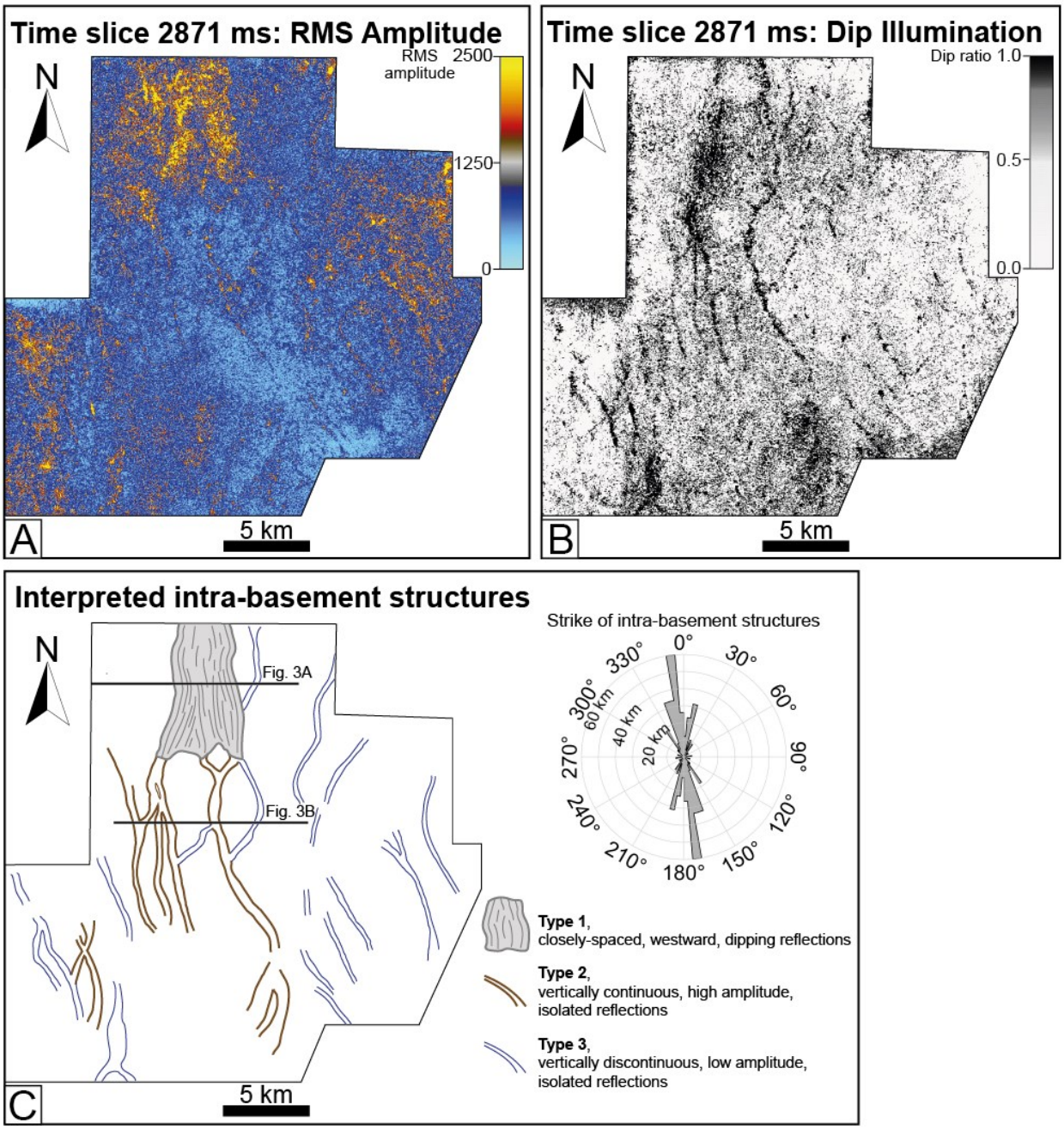

Fig. 4. Seismic attributes and interpreted intra-basement reflections in the shallow crystalline basement. (A) Root Mean Square (RMS) Amplitude and (B) Dip Illumination on time slice 2871 ms (see Fig. 2A). Note the high-amplitude zone corresponding to the Type 1 reflections in (A). (C) Interpreted intra-basement reflections based on the maps of RMS Amplitude (A) and Dip Illumination (B). The inset rose diagram highlights the orientation of the intra-basement reflections; note that the strike varies from NNW-SSE to NNE-SSW.

5.3. Top Basement structures

The Top Basement is dominated by reverse faults and folds, with only few (n=8) normal faults confined to the eastern part of the survey (Fig. 5B). Reverse structures are curvilinear in map-view, and are up to 15 km long, strike NNW-SSE to NNE-SSW (see upper rose diagram in Fig. 5C), and dip westwards. Of the 22 reverse displacement structures (i.e. thrusts and folds), 16 correlate with the intra-basement reflections on time-slice 2871 ms for at least some of their strike length, with 6 thrusts being physically connected to intra-basement reflections for their total strike length (Fig. 5C). In particular, the eastern boundary of the Type 1 reflections zone, and the entirety of a Type 2 reflection connected to it at its southeastern corner, are expressed by prominent anticlines and reverse faults at Top Basement level (Figs. 3C, D and 5C). By contrast, the Type 3 reflections in the eastern part of the survey, and the closely spaced Type 2 reflections in the central part of the survey, are truncated by the Top Basement Unconformity (Fig. 5C), with flat-lying reflections overlying them in the sedimentary cover (Fig. 3E). Normal faults at Top Basement level are linear and strike NE-SW to NNE-SSW (see lower rose diagram in Fig. 5C), with a maximum length of 7 km (Fig. 5B), and displacements of 25-65 ms TWT (50-125 m). They generally show no direct spatial correlation with the intra-basement reflections on time-slice 2871 ms (Fig. 5C) and three of them terminate along-strike against reverse structures (Fig. 5B). In cross-section, reverse faults have a vertical extent of 100-200 ms TWT (150-350 m), with a maximum throw of 30 ms TWT (60 m) at Top Basement (Figs. 3C and D). Reverse faults are typically overlain by west-facing monoclines (Fig. 3C) and anticlines (Fig. 3D), and are physically connected to Type 1 and Type 2 reflections (Figs. 3C and D). In some instances, reverse faults at Top Basement level may become normal faults at shallower levels (Figs. 3A, 3B and 6).

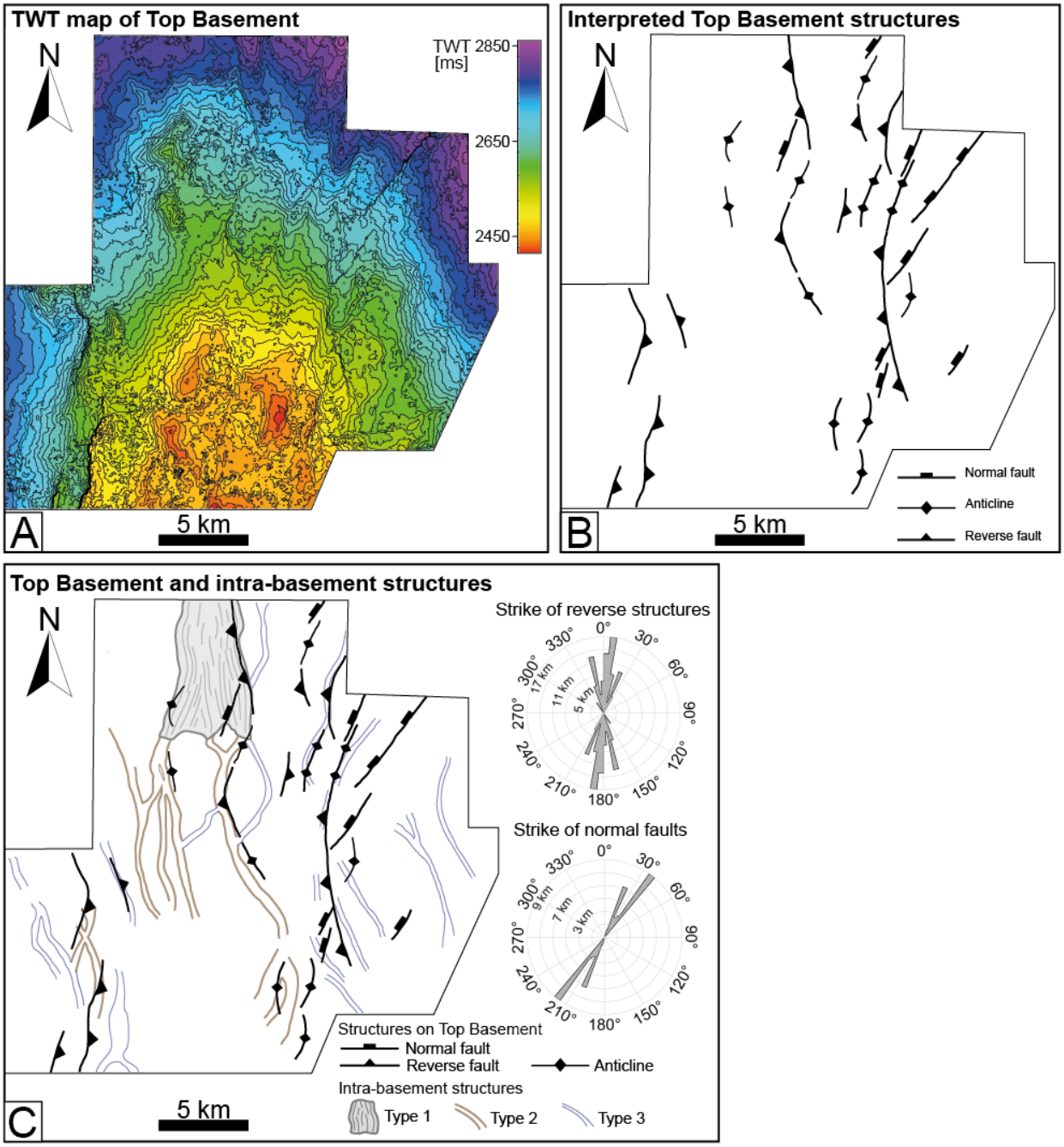

Fig. 5. (A) TWT-structure map of Top Basement. (B) Line drawing of the structures at Top Basement level based on the Top Basement map in (A). (C) Map showing Top Basement structures (in black) together with the intra-basement reflections interpreted on time-slice 2871 ms (in grey). Note the plan-view correlation between Top Basement reverse structures and intra-basement reflections.

5.4. Origin of intra-basement reflections

Prominent intra-basement reflections are typically interpreted as the seismic expression of mylonites within ductile shear zones (e.g. Brewer *et al.*, 1983; Wang *et al.*, 1989; Reeve *et al.*, 2013; Phillips *et al.*, 2016). In particular, the trough-peak-trough wavetrain of intra-basement reflections (Fig. 3) are interpreted as the result of the interference between stacks of 50-100 m thick layers of mylonitic and relatively undeformed rock (Fig. 3) (e.g. Fountain *et al.*, 1984; Hurich *et al.*, 1985; Reeve *et al.*, 2013; Phillips *et al.*, 2016). In addition, the anastomosing geometry of the intra-basement reflections (Fig. 4) strongly resembles the typical pattern of shear zones (e.g. Arbaret and Burg 2003; Carreras *et al.*, 2010; Rennie *et al.*, 2013). We therefore interpret the thick package of reflections (i.e. Type 1; Fig. 3C) as the seismic expression of a stack of mylonitic and intervening, relatively undeformed protolith layers (cf. Phillips *et al.*, 2016). The chaotic seismic character in the centre of the Type 1 structure (Fig. 3C) could be due to lateral variations in composition, different amounts of strain, or complex internal geometries (Klemperer, 1987; Brocher and Christensen, 1990; McDonough and Fountain, 1993). An alternative interpretation is that the discontinuous, complex reflections may be related to destructive interference between adjacent mylonitic bands (Phillips *et al.*, 2016). The low dip (20°-30°) of the isolated reflections (i.e. Type 2 and Type 3; Figs. 3B, D and E) suggests they may have formed as mylonite-bearing thrusts. The higher amplitude of Type 2 (Fig. 3D) compared to Type 3 (Fig. 3E) structures may reflect an increase of the acoustic impedance contrast due to the development of preferred crystallographic orientations and mineralogical segregation during mylonitization (e.g. Robin, 1979). As intrabasement structures are truncated by the Top Basement Unconformity (Fig. 3E), they were already in place before the onset of sedimentation, and thus before the Paleocene (Fig. 2). Furthermore, the shallow dip of intra-basement structures suggests they developed as contractional shear zones, making Mesozoic subduction and basement terranes accretion the most likely event responsible for their origin (e.g. Muir *et al.*, 2000). To support this interpretation, onshore New Zealand's South Island similar contractional ductile shear zones developed during the Early Cretaceous at the eastern edge of the Western Province, accommodating the compression due to terranes accretion (Scott, 2013). The successive kinematic history of the intra-basement structures was reconstructed based on their expression on Top Basement (Fig. 5) due to the lack of pre-kinematic markers within the basement rocks (i.e. reflective, pre-kinematic layering). The plan-view correlation and physical connection between several intra-basement structures and the Top Basement thrusts/folds (Fig. 5C) suggest contractional reactivation and upward propagation of the former (e.g. Mitra, 1990; Erslev and Mayborn, 1997; Brandes and Tanner, 2014), with

vertically and laterally continuous intra-basement structures (i.e. Type 1 and 2) being preferentially reactivated. We attribute this contractional reactivation to the late Miocene inversion (e.g. Reilly *et al.*, 2015), as this is the only compressional event that affected the Taranaki Basin during the Cenozoic.

6. Structures within the sedimentary cover

6.1. Structural style

The Top Tikorangi Horizon illustrates the structural style at a distance of 350-450 ms TWT (650-850 m) above Top Basement (Fig. 2A). This seismic surface highlights an elevated, dome-shaped area towards the southern limit of the survey, which largely reflects the basement paleotopography (cf. Figs. 5A and 6A). Faulting was mostly localised north of this elevated area, with several (n=45), low displacement (<50 m), closely spaced (1-2 km) normal faults (Figs. 6A and B). The overall strike of these faults changes from NNE-SSW to NE-SW towards the east (Fig. 6B), with the fault planes generally dipping westwards. However, in three different parts of the survey fault segments deviate from this trend (blue segments in Fig. 6B), with NNE-SSW faults curving to a N-S strike (F7; Fig. 6B) and a NW-SE strike (F3, F5; Fig. 6B). Although individual fault segments are generally 1-5 km long, they are often linked by connecting faults to form longer and curvilinear fault traces.

The Intra-Giant Foresets Formation Horizon illustrates the fault pattern at a distance of 1850-1950 ms TWT (2000-2100 m) above Top Basement (Fig. 2A). At this structural level, faults are more distributed than at Top Tikorangi level, with several (n=23), low-displacement (<30 m) normal faults spaced 3-4 km one from the other (Figs. 6C and D). The normal faults generally strike from NNE-SSW to NE-SW and dip to the west, defining a series of half-grabens (Figs. 6C and D). In the northern part of the survey, the N-S-striking faults observed at Top Tikorangi level dissect also the Intra-Giant Foresets Formation Horizon, producing three left-stepping N-S-striking fault segments (F7a, b and c; Figs. 6D and E). Furthermore, in the eastern part of the survey a NE-SW-striking fault curves to a N-S strike in its central portion (see red box in Fig. 6D), mimicking the underlying fault geometries (cf. Figs. 6B and 6D). Normal fault segments are 3-8 km long and are clearly separated by relay ramps, suggesting that the fault network is less mature than at Top Tikorangi level.

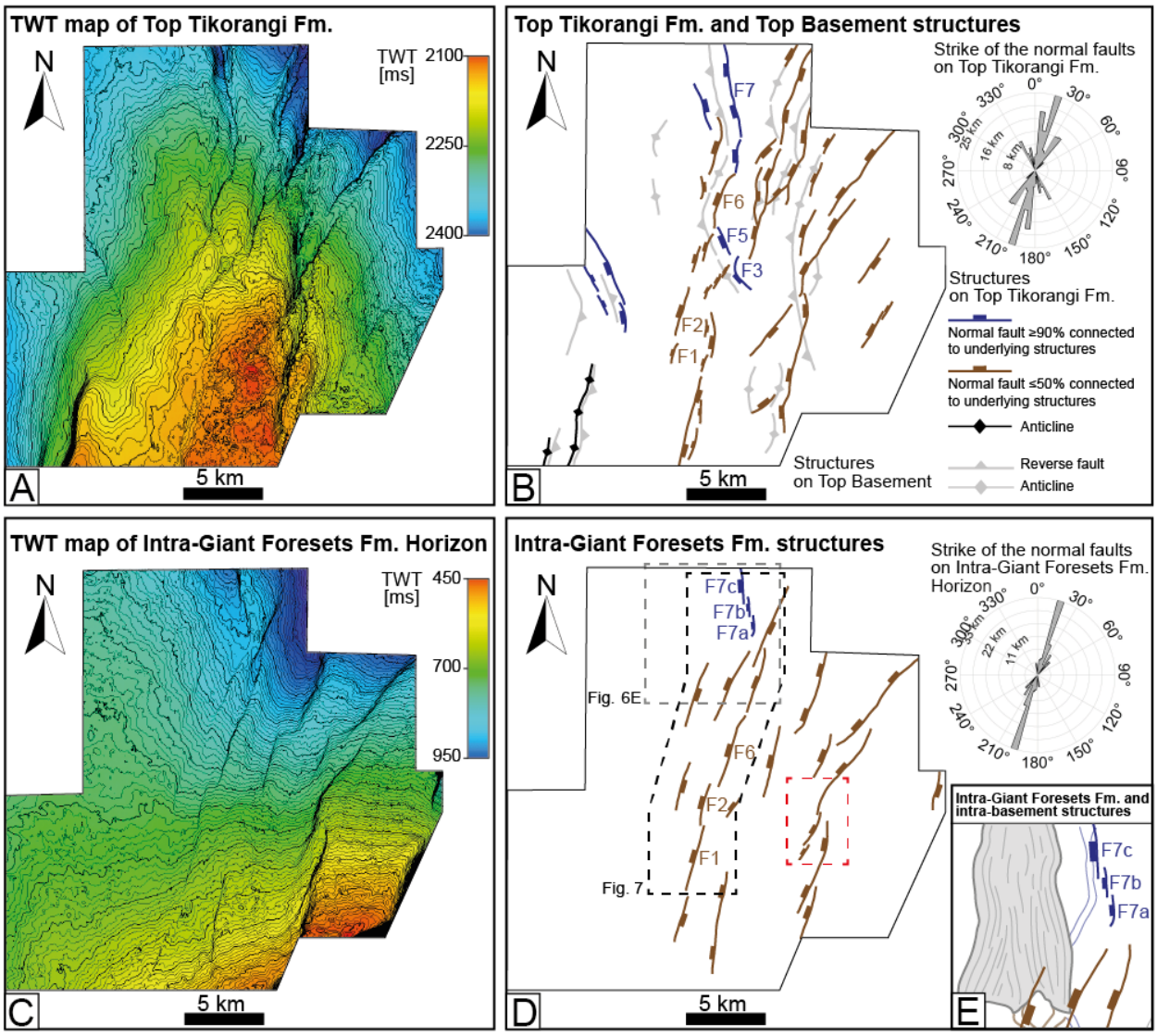

Fig. 6. TWT-structure maps and line drawing illustrating the structural style at different levels of the sedimentary cover (see Fig. 2A). (A) TWT-structure map of Top Tikorangi Formation and (B) line drawing of the interpreted structures. Grey lines delineate the underlying Top Basement structures. Note the plan-view correlation between Top Basement reverse structures and later rift-related faults. (C) TWT-structure map of the Intra-Giant Foresets Formation Horizon and (D) line drawing of the interpreted structures. The mean fault strike highlighted by the inset rose diagram is NNE-SSW. (E) Map showing the normal faults on Intra-Giant Foresets Formation Horizon (coloured segments) together with the underlying intra-basement structures (in grey) in the northern part of the survey (location shown in Fig. 6D). Note the plan-view correlation between the Type 1 structure and the overlying normal faults.

6.2. Timing of normal faulting

Having established the geometry of the normal fault network, we use thickness and seismic-stratigraphic patterns to deduce its temporal evolution. In particular, we describe and interpret the isochron maps of the stratigraphic intervals corresponding to the main rifting events shaping the southern Taranaki Basin (i.e. Paleocene and Pliocene intervals).

The Paleocene succession (65-55 Ma) comprises the Farewell Formation, which uncomformably overlies the crystalline basement (Fig. 2A). The isochron for the Top Basement - Top Farewell Formation interval illustrates an overall northward thickening from 40 to 170 ms TWT (c. 250 m; Fig. 7A), with localised thinning (<30 ms TWT, c. 50 m) above intra-basement structures. For example, we clearly observe thinning of this interval corresponding to the eastern boundary of the Type 1 structure (see red box in Fig. 7A). The absence of thickening into the hanging-wall of normal faults (Fig. 7A), and the lack of wedge-shaped seismic geometries (Fig. 2A) in the Top Basement - Top Farewell Formation interval (65-55 Ma), together suggest the study area was not affected by Late Cretaceous-Early Eocene rifting. This interpretation is supported by the development of conformable, flat-lying, onlapping reflections on the Top Basement (Fig. 2A), suggesting simple infill of inherited relief during the Paleocene.

The overlying Pliocene succession (5.3-2.5 Ma) comprises northward prograding clinothems of the Giant Foresets Formation (e.g. Hansen and Kamp, 2002, 2004; Chenrai and Huuse, 2017; Fig. 2A). In our study area, this succession can be split into two parts based on a vertical change in seismic facies defined by the Intra-Giant Foresets Formation horizon (Fig. 2A). The interval between the Top Upper Manganui Formation and the Intra-Giant Foresets Formation horizons (5.3-3 Ma) thickens northwards from 170 to 270 ms TWT (c. 100 m; Fig. 7B). Within this interval, minimal thickness variations have been observed across the normal faults. The interval between the Intra-Giant Foresets Formation horizon and the Top Giant Foresets Formation (3-2.5 Ma) locally thickens (20 ms TWT, *c.* 20 m) across the NNE-SSW-striking segments (F1, F2 and F6) and the N-S striking segments (F7a-c), delineating two distinct Pliocene depocentres (Fig. 7C). These across fault thickness variations constrain the onset of faulting 3-2.5 Ma (cf. Giba *et al.*, 2010). The rapid change in the thickness pattern between the 5.3-3 Ma and 3-2.5 Ma intervals (cf. Figs. 7B and C), and the elongated shape of the depocentres (Fig. 7C) suggest the bounding normal faults relatively rapidly established their total length in <0.5 Ma.

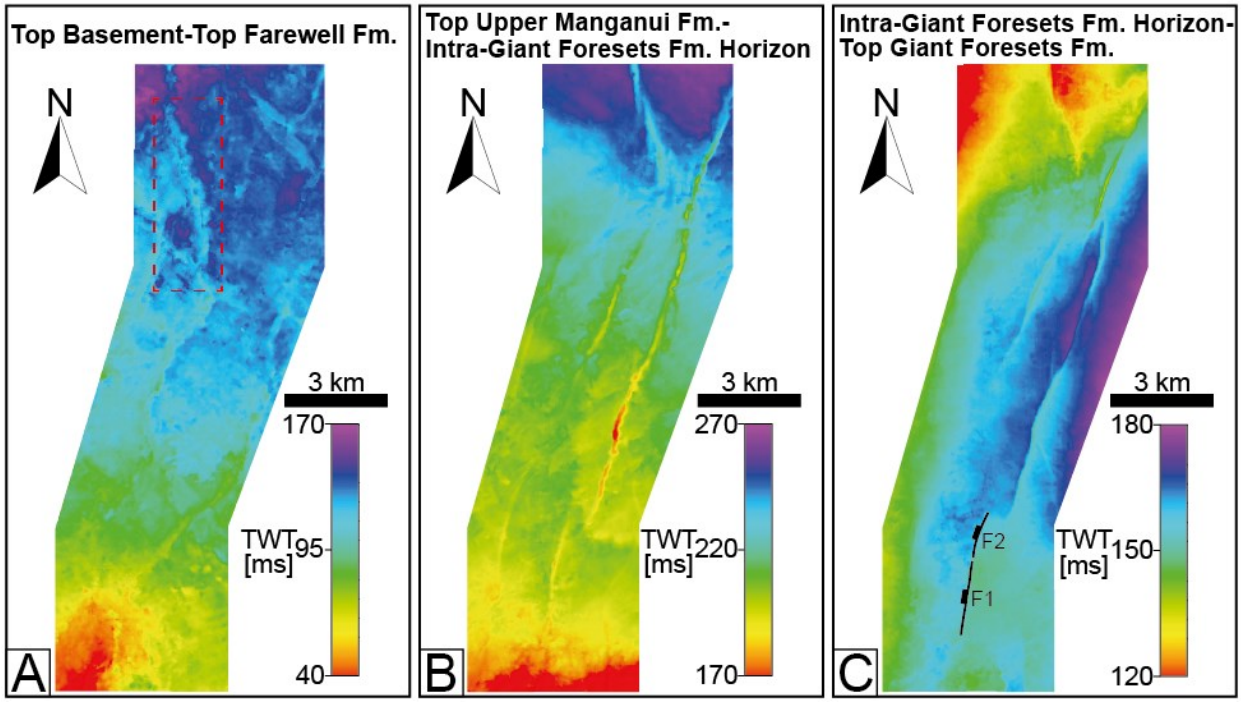

Fig. 7. TWT-thickness maps of the stratigraphic intervals corresponding to the rifting events of the Taranaki Basin (see Fig. 2A). (A) Top Basement - Top Farewell Formation interval (Paleocene). The red box indicates a local thickness decrease corresponding to the edge of the underlying Type 1 structure. (B) Top Upper Manganui Formation - Intra-Giant Foresets Formation Horizon interval (pre-Pliocene rifting). (C) Intra-Giant Foresets Formation Horizon – Top Giant Foresets Formation interval (Pliocene rifting). Note that across-fault thickness variations are only observed in (C). The location of the maps is shown in Fig. 6D.

6.3. Basement structure-cover faults plan-view relationships

In this section, we compare the structural trends immediately below (Fig. 4) and at Top Basement level (Fig. 5) with the normal faults defined at multiple structural levels in the overlying sedimentary cover (i.e. Top Tikorangi Formation, Fig. 6B; and Intra-Giant Foresets Formation horizon, Fig. 6D). Cover faults having different degrees of physical connectivity to intra-basement structures generally display different strikes and vertical extent. Nine normal faults appear physically connected to intra-basement structures for ≥ 90 % of their strike length (blue segments in Figs. 6B and D). These dominantly connected normal faults strike NNW-SSE to N-S (Fig. 6) and generally only extend <1500 m above Top Basement (cf. Figs. 6B and D). Within this group of normal faults, only the N-S-striking fault segments that are connected to the Type 1 structure (F7a-c) extend through the whole sedimentary succession and cross-cut the Intra-Giant Foresets Formation horizon (Fig. 6E). On the other hand, the majority of normal faults (36 out of 45) are physically disconnected or are connected to intra-basement structures for ≤ 50% of their strike length (brown segments in Figs. 6B and D). These partially connected/disconnected normal faults strike NE-SW to NNE-SSW (Fig. 6D) and extend up to 3000 m above Top Basement, crosscutting almost the entire cover succession (cf. Figs. 6B and D). Most of the partially connected normal faults occurs in the northern part of the survey, where intra-basement structures are favourably oriented to link with the overlying normal faults (Fig. 6B).

7. 3D geometry and throw distribution on cover normal faults

We identify four possible styles of interaction and linkage between normal faults in the sedimentary cover and intra-basement structures based on their 3D geometric relationships, and throw distribution on the former. These styles are: I) normal faults physically disconnected from intra-basement structures; II) NW-SE-striking normal faults physically connected to Type 2 structures; III) NNE-SSW-striking normal faults physically connected to Type 2 structures; and IV) N-S-striking normal faults physically connected to the Type 1 structure.

7.1. Normal faults physically disconnected from intra-basement structures

Faults F1 and F2 are representative of the NE-SW to NNE-SSW-striking normal faults that are physically disconnected from the intra-basement structures (Fig. 8A). Both F1 and F2 have linear fault planes, dip westwards (Fig. 8A), and are characterised by minor, across-fault thickening of the interval between the Intra-Giant Foresets Formation and the Top Giant Foresets Formation horizons (20 ms TWT, c. 20 m; Fig. 7C). However, we note that the expansion index is c. 1 at the lateral tips of F1 and F2 (Fig. 8C), suggesting that, in these regions at least, the faults never reached the surface and remained blind. The tip line of F1 is semi-elliptical, with a flat upper tip line in the Pliocene interval, and an arcuate lower tip line in the Eocene/Miocene succession (Fig. 8D). The fault is tallest (c. 2000 m) at its centre (Fig. 8D). The throw contours on the fault surface define a "bullseye pattern" (Fig. 8D), centered on a throw maximum (*c.* 30 m) in Miocene strata (Fig. 8B). The throw gradient is higher towards the upper tip line than the lower or lateral tips (Fig. 8D). F2 is up to 2400 m tall, with a relatively irregular, concave downward, crescentic fault surface (Fig. 8D), which may reflect the strain shadowing (e.g. Gupta and Scholz, 2000) due to the flanking faults (F1 and F6; Fig. 6D). The lower tip line is c. 200-500 m above an underlying, N-trending Type 2 intra-basement structure (Figs. 8A) that, differently from several other Type 2 intra-basement structures, do not appear to have been significantly reactivated during the late Miocene inversion, as indicated by the absence of associated thrusts and folds at Top Basement level. T-z profile for F2 is broadly symmetrical, with a single throw maximum at the fault centre (*c.* 30 m) decreasing radially and smoothly away from this point towards the tip line (Figs. 8B and D; cf. "C-type" profiles of Muraoka and Kamata, 1983).

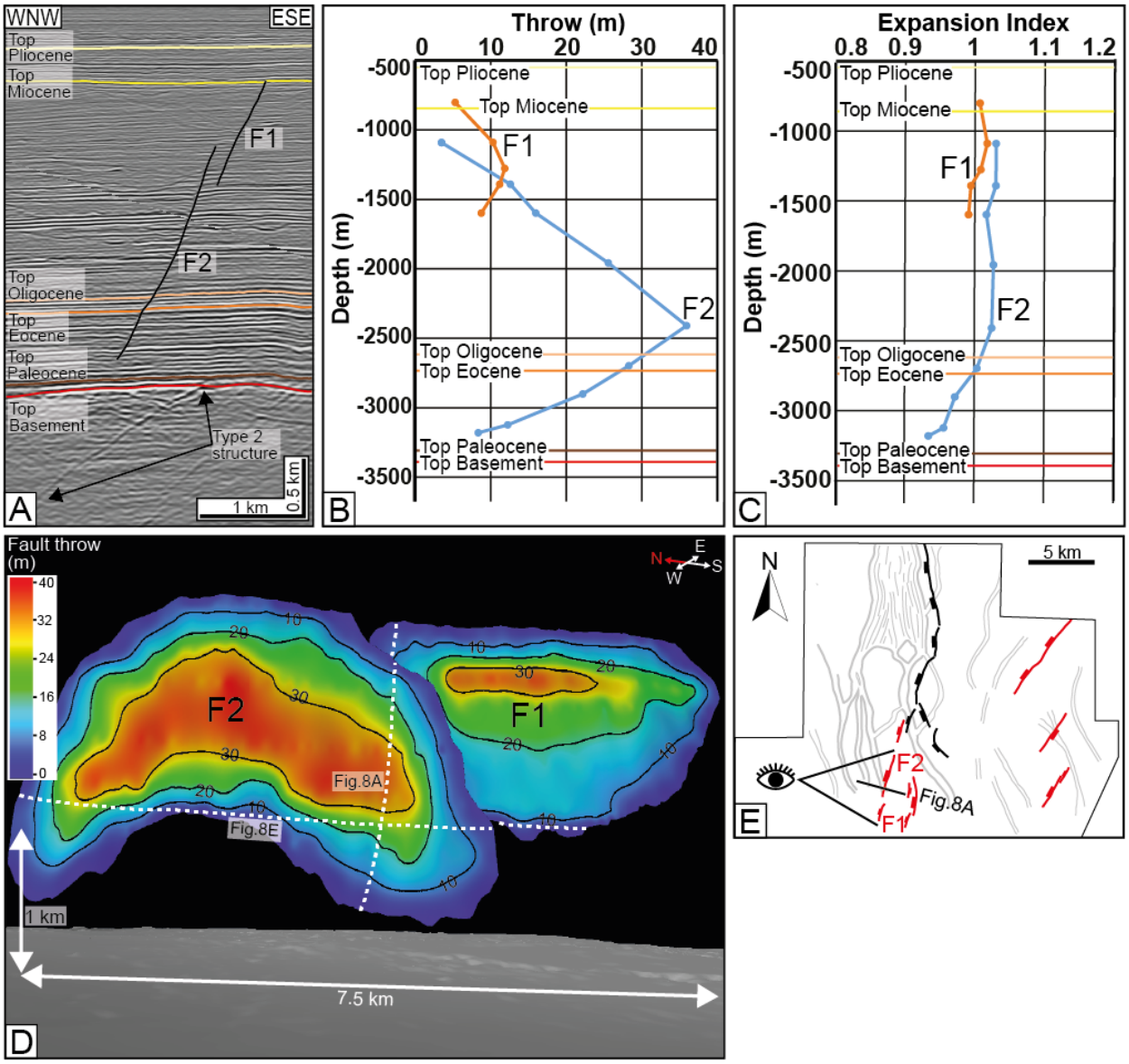

Fig. 8. Quantitative analysis of faults F1 and F2. (A) Seismic section oriented orthogonal to F1 and F2 (location shown in Fig. 8E). Note the straight, steep (60°) fault surfaces and the presence of a Type 2 structure under the cover faults. (B) T-z and (C) expansion index plots taken from the seismic section in (A). Note the broadly, symmetrical throw profiles. (D) Throw distribution on faults F1 and F2. Each fault surface displays a single throw maximum, with broadly elliptical contours. Dashed lines indicate the intersection of the fault planes with the seismic section and the map shown in Figs. 8B and E, respectively. The grey surface is Top Basement. (E) Simplified map based on Top Tikorangi Formation showing the location of F1, F2 and the other normal faults disconnected from intra-basement structures (in red).

7.2. NW-SE-striking normal faults physically connected to Type 2 structures

Faults F3-5 represent examples of NW-SE-striking normal faults that are physically connected to Type 2 structures along most of their strike length (Fig. 9A). F3-5 are <1500 m tall, offsetting only the lowermost part of the sedimentary cover (Fig. 9A), and are not associated with any significant across-fault thickness variations (Figs. 7 and 9C). F3 is *c.* 3 km long, with its upper tip line located in Middle Miocene strata, c. 1500 m above Top Basement (Figs. 9A and D). F4 and F5 are shorter (*c.* 1 km) than F3, terminating upwards in Eocene strata, c. 800 m above Top Basement (Figs. 9B and D). Each fault displays a single throw maximum (*c.* 30-40 m) in Eocene strata (Fig. 9D), with throw decreasing smoothly away from this point towards its tip line (Fig. 9D). The key difference between F3-5, and normal faults physically disconnected from intra-basement structures (i.e. F1-2), is the reverse throw region (up to -30 m) just above Top Basement (cf. Figs. 8D and 9D).

7.3. NNE-SSW-striking normal faults physically connected to Type 2 structures

Fault F6 is representative of the numerous NNE-SSW-striking normal fault physically connected to Type 2 structures (Fig. 10A). F6 consists of two vertically offset, c. 5 km long segments (F6a, lower segment; and F6b, upper segment), with a total fault height of *c.* 2900 m (Fig. 10A and D). The lower fault segment, F6a, is physically connected to the underlying Type 2 structure along its central portion (for c. 50% of its total length; Fig. 10D) as well as to the overlying normal fault segment F6b (for c. 1 km; Fig. 10A). No across-fault thickness variations occur in association with F6a, although the Paleocene thins slightly from the fault footwall to its hangingwall (Fig. 7A; see also expansion index values <1 in Fig. 10C). The T-z plot for F6a reveals a throw maximum in Eocene strata (*c.* 60 m) and, in a similar way to F3-5, reverse throw values (up to -40 m) near Top Basement (Fig. 10B). This Eocene throw maximum is elongated, approximately corresponding to the area of physical linkage between this and the underlying intra-basement structure (Fig. 10D). The upper segment F6b is associated with across-fault thickening of Pliocene strata (Fig. 7C) and a flat upper tip line (Fig. 10D). The throw maximum on F6b is located in Miocene rocks (*c.* 60 m), with the throw profile being slightly skewed towards the fault lower tip (Figs. 10B). Throw values are higher towards the zone of physical connection with the lower segment (F6a) than towards the lower tip line (Fig. 10D).

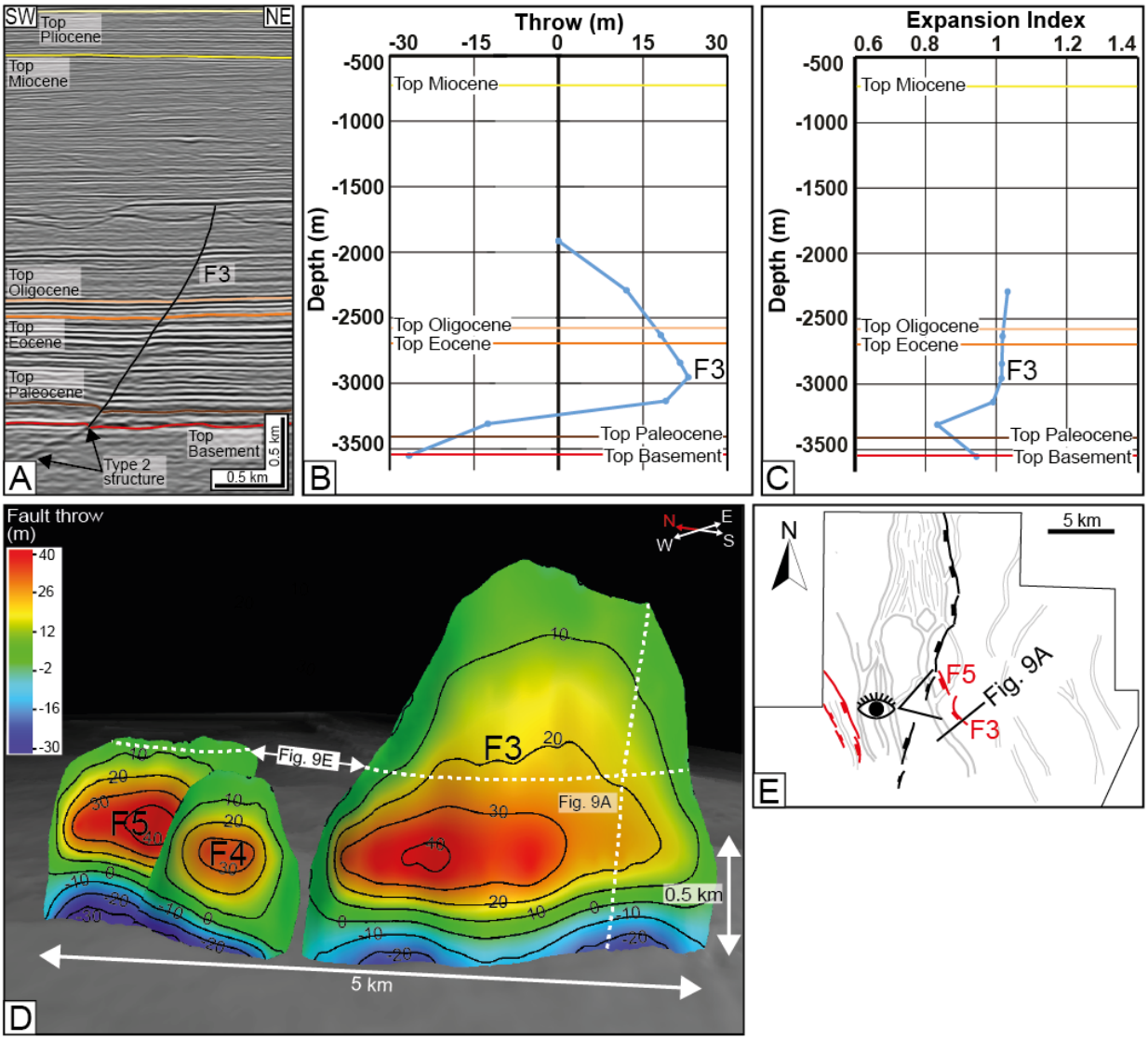

Fig. 9. Quantitative analysis of F3, F4 and F5. (A) Seismic section oriented orthogonal to F3 (location shown in Fig. 9E). Note the physical linkage between F3 and the underlying Type 2 structure. (B) T-z and (C) expansion index plots taken from the seismic section in (A). Note the rapid transition to the zone of reverse throw near Top Basement. (D) Throw distribution on F3-F5. Each fault displays a single throw maximum, and a zone of reverse throw near Top Basement. Dashed lines indicate the intersection of the fault planes with the seismic section and the map shown in Figs. 9A and E, respectively. The grey surface is Top Basement. (E) Simplified map based on Top Tikorangi Formation showing the location of F3, F5, and the other NW-SE-striking normal faults physically connected to Type 2 structures (in red).

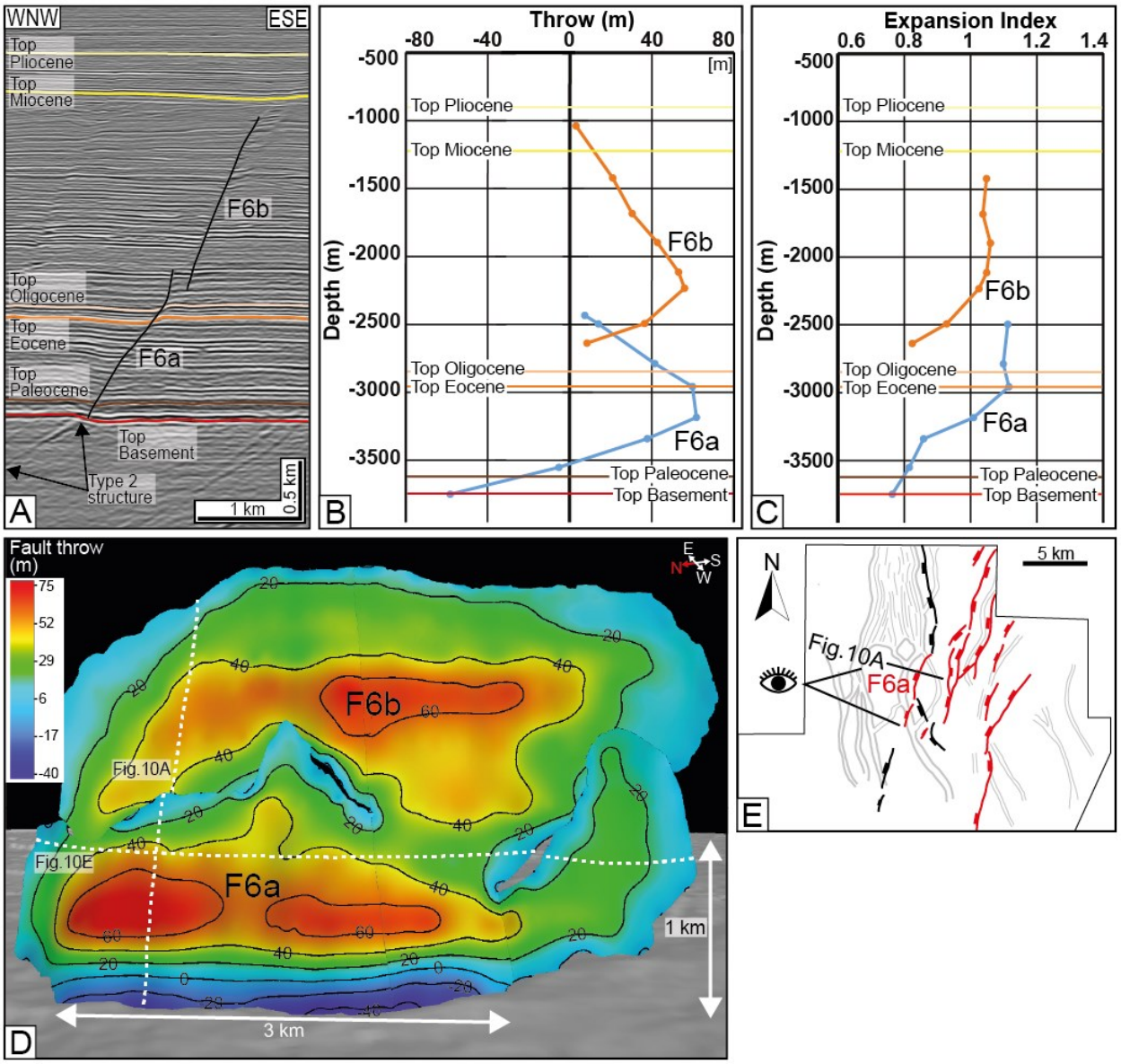

Fig. 10. Quantitative analysis of F6a and F6b. (A) Seismic section oriented orthogonal to F6a and b (location shown in Fig. 10E). Note the physical linkage between F6a and the underlying Type 2 structure. (B) T-z and (C) expansion index plots taken from the seismic section in (A). (D) Throw distribution on F6a and b. The fault segments are physically connected along a small portion of their length, and display two distinct throw maxima. Dashed lines indicate the intersection of the fault planes with the seismic section and the map shown in Figs. 10A and E, respectively. The grey surface is Top Basement. (E) Simplified map based on Top Tikorangi Formation showing the location of F6a, b and the other NE-SW to NNE-SSW-striking normal faults physically connected to Type 2 structures (in red).

7.4. N-S-striking normal faults physically connected to the Type 1 structure

Fault F7 represents the normal faults physically connected to the Type 1 structure, which is located in the northern part of the study area (Fig. 11A). F7 is at least *c.* 5 km long and 3200 m tall, with its northern extent located beyond the limit of the 3D seismic survey (Fig. 11D). F7 is physically connected to the underlying Type 1 structure for its entire length and strikes approximately parallel to it (i.e. N165°; Figs. 11D and E). Similar to faults physically connected to the Type 2 structures (i.e. F3-6), F7 is characterised by reverse throw values (up to -60 m) and expansion index values <1 immediately above Top Basement (Figs. 11B and C). Approximately 1300 m above Top Basement, F7 splays upwards into three, left-stepping, en-echelon segments (F7a-c; Fig. 11D), which extend to the Intra-Giant Foresets Formation horizon (Fig. 11 F). However, at this structural level, segments F7a-c strike N180°, oblique to and defining a 15° clockwise rotation from the lowermost part of the fault (cf. Figs. 11E and F), resulting in twisting of the fault surface. Furthermore, the upper segments dip more gently than the lower part of the fault, resulting in a broadly sigmoidal cross-sectional geometry (Fig. 11A). The T-z plot reveals a B-shaped throw profile, with two throw maxima (*c.* 60-80 m) in Eocene and Miocene strata (Fig. 11B). On the fault surface, the lower throw maximum extends laterally for almost the entire fault length, whereas we observe three discrete throw maxima in the Miocene succession, corresponding to the individual segments (F7a-c; Fig. 11D).

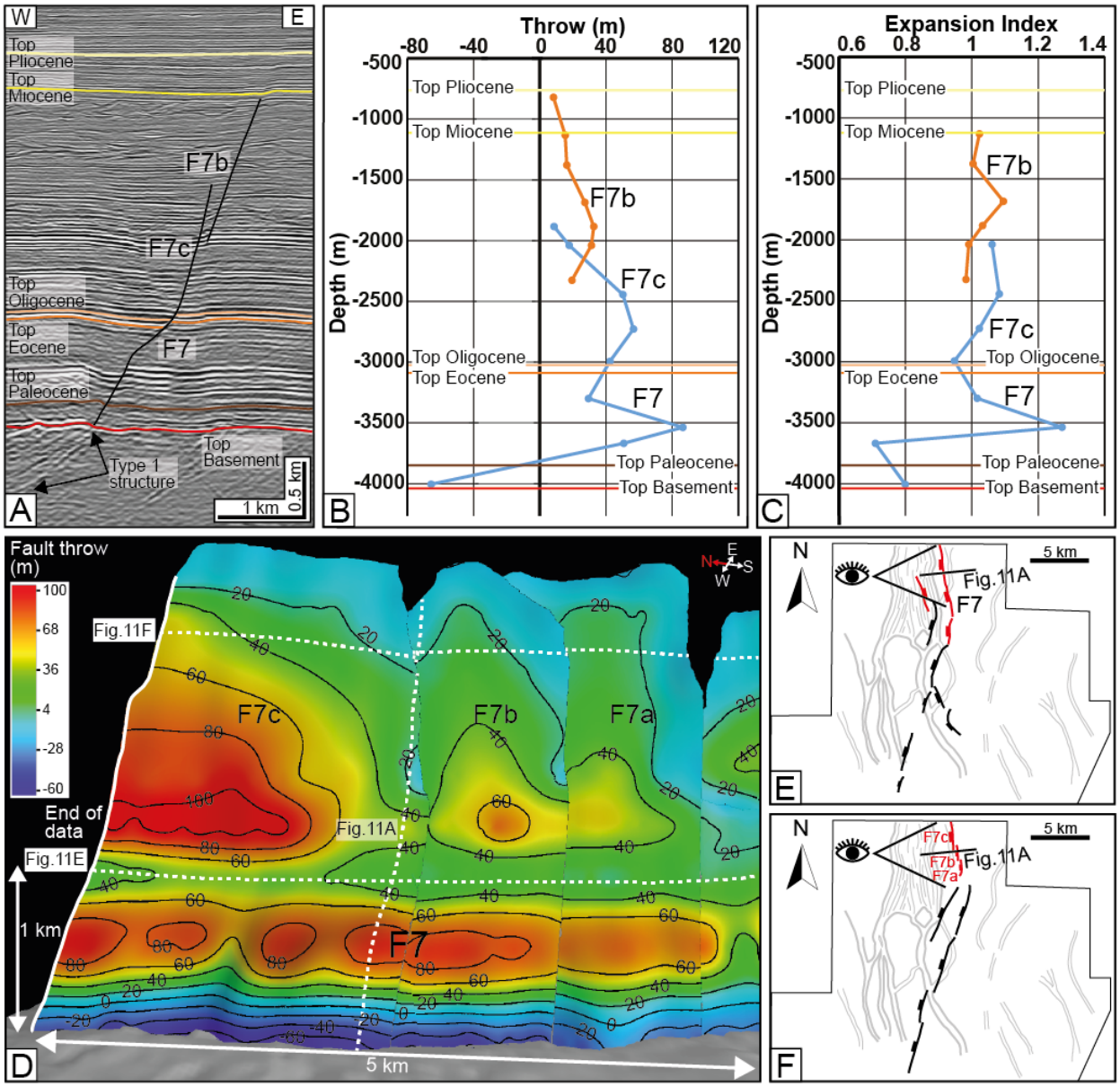

Fig. 11. Quantitative analysis of F7. (A) Seismic section oriented orthogonal to F7 (location shown in Fig. 11E). Note the sigmoidal cross-sectional geometry of the fault surface, and physical connection with the underlying Type 1 structure. (B) T-z and (C) expansion index plots taken from the seismic section in (A). Note the B-shaped profile and the reverse throw near Top Basement. (D) Throw distribution on F7. The fault plane splays upwards into three, en-echelon, left-stepping segments, having discrete throw maxima (F7a, F7b and F7c). A fourth, elongated throw maximum is present on the lower part of the fault. Dashed lines indicate intersection of the fault planes with the seismic section and the maps shown in Figs. 11A, E and F. (E) Simplified map based on Top Tikorangi Formation showing the location of F7 and the other normal faults physically connected to the Type 1 structure (in red). (F) Simplified map based on Intra-Giant Foresets Formation horizon. Note the presence of three distinct fault segments at this stratigraphic level (F7a, b and c; in red).

8. Interpretation and discussion

8.1. Growth history of normal faults

The cover normal faults physically disconnected from the intra-basement structures (e.g. F1 and F2; Fig. 8) show a more regular throw distribution than those that are physically connected (e.g. F3-7; Figs. 9, 10 and 11). The former display a single throw maximum in the Miocene sedimentary sequence that decreases radially towards the tip line (Fig. 8), whereas the latter display an area of reverse throw at the base of the fault plane (i.e. in Paleocene strata, 200-300 m above Top Basement; Figs. 9, 10 and 11), with a throw maximum located in Eocene strata (400-500 m above Top Basement; Figs. 9, 10 and 11). Of the faults physically connected to intra-basement structures, some display a single throw maximum in Eocene sedimentary sequence (Fig. 9), whereas others display an additional throw maximum in Miocene sedimentary cover, resulting in B-shaped throw profiles (Figs. 10 and 11). Importantly, the areas of reverse throw at the fault base are commonly overlain by folds (Figs. 3C and D), suggesting: (i) intra-basement structures were compressionally reactivated during late Miocene inversion and propagated upwards into the sedimentary cover as blind structures, resulting in fault-propagation folds (e.g. Mitra, 1990; Erslev and Mayborn, 1997; Figs. 12A and B); and (ii) intra-basement structures were slightly, if at all, extensionally reactivated during Plio-Pleistocene rifting, as any hypothetical normal slip must be smaller than the late Miocene reverse displacement (Fig. 12C). We consider this lack of or only very limited extensional reactivation reflects: (i) the shallow dip of intra-basement structures (20°-30°, Fig. 3), making them unfavourable structures to accommodate extension (Sibson, 1985); and (ii) the relatively small amount of regional extension (low beta-factor) accommodated in the Taranaki Basin during the Plio-Pleistocene (Giba *et al.*, 2010).

Given the lack of evidence for significant extensional reactivation of the intra-basement structures, we infer the cover normal faults preserved broadly the original throw distribution, which can thus be used to infer their growth history (cf. Deng *et al.*, 2017). Hence, we interpret that the lower (i.e. Eocene) and the upper (i.e. Miocene) throw maxima represent nucleation of normal faults in Eocene and Miocene sedimentary succession, respectively (cf. Mansfield and Cartwright, 1996; Hongxing and Anderson, 2007). Normal faults must necessarily initiate after the deposition of the stratigraphic package hosting their nucleation sites; this implies that normal faults with nucleation sites in Miocene strata formed during the Plio-Pleistocene rifting event, whereas normal faults with nucleation sites in Eocene strata reflect Cretaceous-Early Eocene or the Plio-Pleistocene extension. However, rift-related extensional activity ceased by the end of the Paleocene in the

western part of the Taranaki Basin (Strogen *et al.*, 2017), where our study area is located (Fig. 1). Furthermore, in the Paleocene interval we see no fault-related thickness variations that could be attributed to normal faulting of this age (Fig. 7A). These stratigraphic considerations suggest the studied normal fault network formed during the Plio-Pleistocene rifting event (Fig. 12C). Furthermore, Plio-Pleistocene normal faulting is clearly indicated by distinct fault-related thickness variations (Fig. 7) and, in some cases, by flat upper tiplines associated with steep throw gradient (Fig. 8; cf. Nicol *et al.*, 1996; Childs *et al.*, 2003; Baudon and Cartwright, 2008c). However, we cannot rule out that some normal faults first developed during Paleocene-Early Eocene rifting and were subsequently compressionaly reactivated during late Miocene inversion. The B-shaped profiles of some normal faults physically connected to intra-basement structures (Figs. 10 and 11) likely reflect dip linkage between initially isolated, and occasionally still partly disconnected (Fig. 10), fault segments that nucleated in Eocene and Miocene sedimentary succession. Importantly, our stratigraphic considerations suggest the lower and the upper fault segments developed during the same rifting event (i.e. Plio-Pleistocene rifting), implying they may have been kinematic coupled (Fig. 12, case 2). However, the normal faults disconnected from intra-basement structures, which nucleated in the upper part of the cover (i.e. in the Miocene sedimentary succession), grew freely by simple radial tip line propagation, suggesting only limited mechanical and kinematic constraints by deeper fault segments as well as intra-basement structures (Fig. 12C, case 1).

8.2. Influence of intra-basement structures on normal faulting

Having established that the studied normal fault network largely developed during a single phase of Plio-Pleistocene extension, we argue that the variability of fault strikes within this relatively small area (Fig. 6) reflects the variable influence of pre-existing mechanical anisotropies in the underlying basement rocks, rather than a temporal or spatial change of extension direction. Given the intra-basement structures have been poorly, if at all, extensionally reactivated during the Plio-Pleistocene rifting event, their influence on the development of normal faults cannot be explained by simple extensional reactivation and upward propagation. Hence, other processes must be invoked to explain the spatial correlation and the physical connectivity between intra-basement structures and cover faults (Figs. 9, 10 and 11). The reverse throw region just above the physical connection to intra-basement structures (Figs. 9, 10 and 11) suggests that cover faults initiated as thrusts due to late Miocene reverse reactivation and upward propagation of intra-basement structures. The sharp transition from this reverse throw region to elongated throw maxima (Figs. 9, 10 and 11) indicates that Plio-Pleistocene normal faults nucleated at a short distance away, and

possibly directly, from the upper tip of late Miocene thrusts. The localisation of new normal faults at a short distance from pre-existing structures may reflect: (i) accumulation of stress on pre-existing structures (i.e. intra-basement structures and the overlying late Miocene thrusts; Jackson and Rotevatn, 2013); (ii) and, possibly, preferential nucleation of new normal faults from pre-existing weak anisotropies (i.e. late Miocene thrusts).

A variety of mechanisms can contribute to the nucleation of faults within the damage zones of thrusts and folds, rather than within intact country rock: (i) strength reduction due to pervasive fracturing (e.g. Gudmundsson, 2011; Sun *et al.*, 2017); (ii) reduction of the effective stress due to higher permeability and pore fluid pressure (e.g. Sibson, 1995); and (iii) a range of strain weakening effects, including gouge formation, mineral transformation and microstructural re-arrangement (e.g. Bos and Spiers, 2002). The positive feedback between these processes may result in propagation and linkage of fractures, leading to the final development of through-going faults (cf. Vass *et al.*, 2014). The nucleation of normal faults at the upper tips of deeper lying, pre-existing thrusts is also observed in both physical models of and natural examples presented by Faccenna *et al.* (1995). Furthermore, these models support the possibility that new normal faults can nucleate also from pre-existing structures that do not undergo extensional reactivation. In a more general sense, nucleation of new normal faults from pre-existing structures has been widely documented during multiphase extension, with new normal faults nucleating from older normal faults (e.g. Henza *et al.*, 2010; Duffy *et al.*, 2015; Withjack *et al.*, 2017). Interestingly, when normal faults emanated from pre-existing structures striking nearly perpendicularly to the Plio-Pleistocene extension direction (i.e. NW-SE; Giba *et al.*, 2012), they propagated to the upper part of the cover through nucleation and dip linkage of kinematically related segments (Fig. 10). In contrast, when normal faults emanated from pre-existing structures striking strongly obliquely to the Plio-Pleistocene extension direction, they remained restricted to the lower part of the cover (Fig. 9). This selective upward propagation of normal faults suggests the regional stress field becomes dominant over the intra-basement structures as distance from the latter increases, allowing only for favourably oriented structures to propagate to the upper part of the cover (Fig. 12C, case 2). The dominant influence of the regional stress field in the upper part of the cover is supported also by the nucleation and growth of optimally-oriented (i.e. NE/NNE-striking) normal faults in the Miocene-Pliocene sedimentary succession (Fig. 12C, case 1).

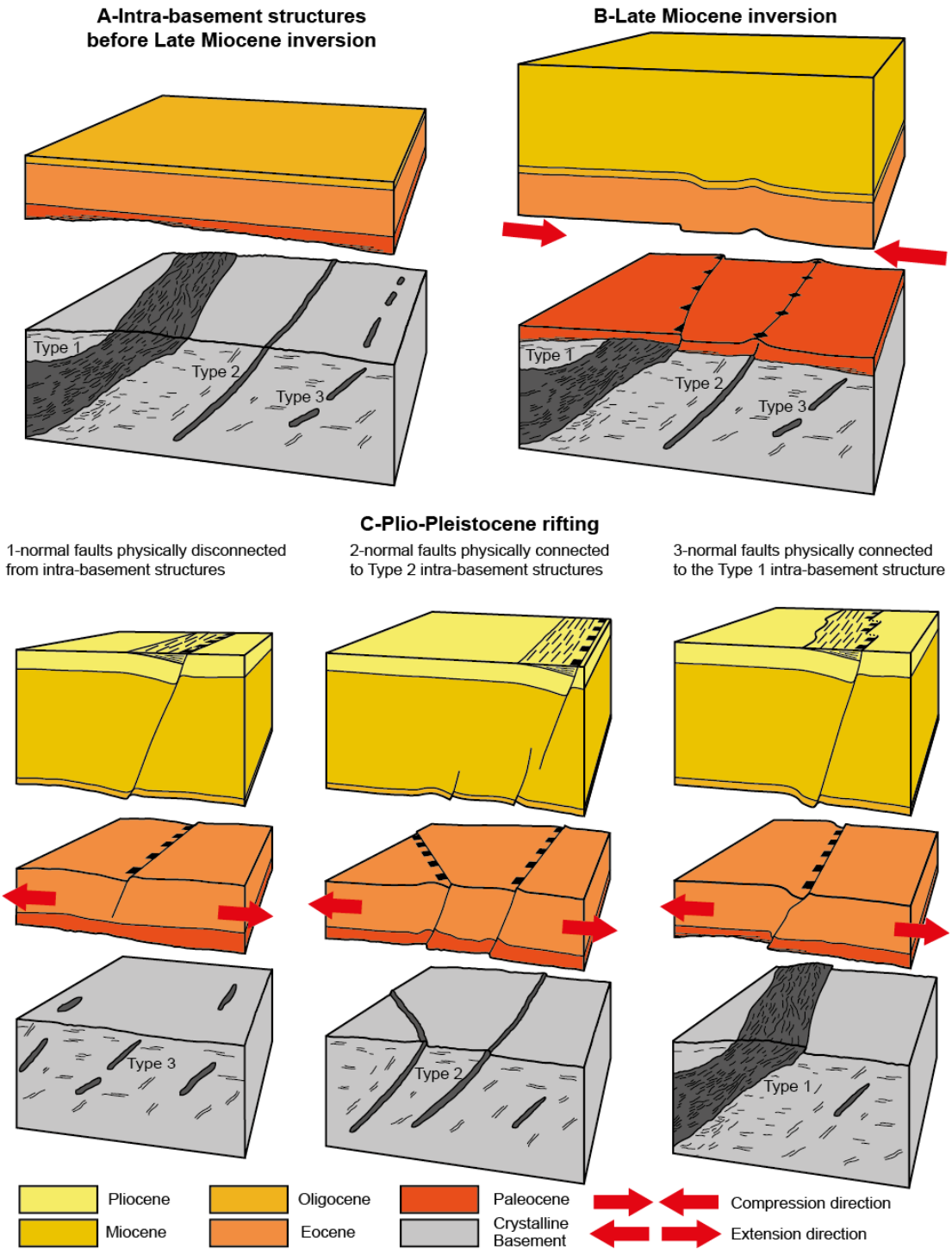

Fig. 12. Synoptic figure illustrating the structural evolution of the study area. Block diagrams have been cut along horizontal sections to highlight the possible geometric relationships between structures at different levels. (A)-(B) Note the selective reactivation and upward propagation of intra-basement structures during late Miocene inversion. (C) Pre-existing structures offered sites for the nucleation of new normal faults and locally perturb the regional stress field during Plio-Pleistocene rifting. Note that type, strike and reactivation history of intra-basement structures determine whether, and to which extent, they influence overlying normal faults, producing different geometric and kinematic relationships (cf. case 1, 2 and 3).

8.3. Far-reaching influence of km-wide intra-basement structures over normal faults

We have now established the general geometric and kinematic relationships between intra-basement structures and cover normal faults, highlighting that oblique normal faults are generally restricted to the lower part of the sedimentary sequence (<1500 m from Top Basement; Fig 12C, case 2). Only the normal faults physically connected to the Type 1 structure propagated through the entire sedimentary succession (Fig. 12C, case 3), despite being oblique to the Plio-Pleistocene extension direction (i.e. NW-SE; Giba *et al.*, 2012). Differently from the other cover faults, they display a clear up-sequence rotation of fault strike, with the obliquity to the Plio-Pleistocene extension direction decreasing progressively towards the upper part of the sedimentary cover (cf. Figs. 11E and F). Furthermore, our kinematic analysis indicates that F7, F7a-c likely initiated as isolated segments that eventually linked to form a single, somewhat sigmoidal fault plane. Hence, new normal faults geometrically and kinematically related to the intra-basement structures (i.e. F7a-c) appear to have nucleated at a significant distance from the latter (c. 1500 m), propagating to the upper part of the cover (Fig. 11). Similarly, numerical models highlighted that the upward propagation of a deep, reactivated structure is often associated with the nucleation and downward propagation of a normal fault in the upper part of the sedimentary sequence, which later merge into a single fault plane (Abe *et al.*, 2011). Although the mechanism by which a pre-existing deep structure can constrain the geometry and kinematics of a normal fault in the upper part of the sedimentary sequence is still to be understood, such far-reaching influence may be contributed by the stress field perturbation arising around mechanical anisotropies. Indeed, Tingay *et al.* (2010) document perturbations of the regional stress field around deep, pre-existing faults, resulting in a rotation of the fault strike through the sedimentary succession, which strongly resembles the overall geometry of F7, F7a-c (cf. Figs. 11E and F). In particular, pervasive mechanical anisotropies within km-wide intrabasement structures have been suggested to give broad perturbation of the regional stress field (Morley, 2010), as suggested also by normal faults merging at depth with km-wide shear zones (Phillips *et al.*, 2016). The development of an oblique fault across the entire sedimentary succession may suggest that the lower fault segment (F7) has favoured a form of stress transfer between the mechanically anisotropic intrabasement shear zone and the upper part of the sedimentary succession.

8.4. Implications for non-colinear rift fault network

We reconstructed the evolution of a non-colinear rift fault network overlying crystalline basement, highlighting different geometric and kinematic relationships between normal faults and intra-basement structures (Fig. 12). Our study shows that widespread fabrics in the crystalline basement can lead to the development of pervasive non-colinear fault systems also during a single rifting event, as observed in the Gulf of Thailand (e.g. Morley *et al.*, 2004; 2011; Morley, 2017) and in the North Sea (e.g. Bartholomew *et al.*, 1993; Foerseth *et al.*, 1995; Reeve *et al.*, 2015). In particular, pre-existing basement structures have been shown to act as a template for later rift-related faults also in the neighbouring Taupo Rift, located onshore New Zealand's North Island (Fig. 1, inset; Seeback *et al.*, 2014). The complex fault patterns arising due to the influence of pre-existing structures may be misinterpreted as the result of multiple tectonic phases, leading to erroneous reconstruction of the tectonic histories of sedimentary basins. Although both pre-existing fabrics and multiple rotations of the main extension axis may contribute to non-colinear faulting in the same setting (Morley *et al.*, 2004; 2011; Morley, 2017), here we propose some simple criteria for discriminating between these two driving mechanisms for non-colinear faulting. The best way to determine whether underlying intra-basement structures influence the development of the overlying rift-related normal fault network is by comparing the distribution and geometry of both sets of structures, and, if possible, their kinematics. However, intra-basement structures are often poorly imaged in seismic data and are rarely preserved along with the overlying normal faults in the same outcrop, implying we typically rely on only qualitative correlation between seismically imaged normal faults and basement tectonic trends observed onshore (e.g. Roberts and Holdsworth, 1999; Wilson *et al.*, 2006). Our study highlights that the influence of basement fabrics over normal faults changes through the sedimentary cover, resulting in a non-colinear fault system being mostly restricted within few hundred metres from the Top Basement. When the mechanical stratigraphy is relatively simple and homogeneous, non-colinear fault systems restricted to the lower part of sedimentary cover may be related to the influence of deep basement fabrics. Alternatively, an increase in structural complexity in the lower part of the sedimentary sequence may be explained by multiple rifting events, which are more likely to affect the lower, and thus older, part of the sedimentary sequence than the upper part. When a portion of the sedimentary sequence is affected by multiple rifting events, the most common linkage style is represented by sharp, abutting intersections (Henza *et al.*, 2010; 2011), with the second stage faults having a single throw maximum near the branchline (Duffy *et al.*, 2015). In contrast, in our study no abutting intersections are observed, fault strike changes gradually along the fault length (Fig.

6B), and throw maxima are elongated, having approximately the same lateral extent as the underlying intra-basement structures (Figs. 8, 9, 10 and 11). However, (i) the degree of rotation of the extension axis (Keep and McClay, 1997; Henza *et al.*, 2010; 2011) and (ii) the oblique component of the deformation (Keep and McClay, 1997) can result in strong variability of the final fault pattern in multiphase rifts, making difficult to highlight the influence of basement fabrics based only on final fault geometries. Thus, we recommend 3D reconstruction of the throw distribution as a powerful tool to assess the influence of deep basement fabrics on the overlying normal faults, when it is not possible to visualise directly their geometric relationships.

9. Conclusions

Based on the integration of time-structure maps, cross-sections and detailed 3D kinematic analyses, we draw the following key conclusions regarding the influence of intra-basement structures on the development of rift-related normal faults in the Taranaki Basin, offshore New Zealand:

1. In the study area, intra-basement structures appear to have played a key role during the Plio-Pleistocene rifting, as suggested by several normal faults mimicking the underlying intra-basement structures and physically connected to them. This resulted in non-colinear faulting, with normal faults striking obliquely to the regional trend of the rift. However, in the upper part of the cover there are also normal faults that do not seem to be affected by intra-basement structures.
2. The normal faults physically connected to underlying intra-basement structures typically show a sharp transition to a zone of reverse throw near Top Basement. Reverse throw is interpreted as the result of compressive reactivation and upward propagation of the intra-basement structures during the late Miocene. The preservation of the original reverse throw suggests that intra-basement structures were not significantly reactivated during the Plio-Pleistocene rifting. This implies that extensional reactivation is not a fundamental condition for intra-basement structures to have an influence on rift-related normal faults.
3. The normal faults physically connected to intra-basement structures display throw maxima (i.e. nucleation points) at a short distance (100-200 m) from, and with approximately the same lateral extent as, the area of reverse throw just above Top Basement. This throw distribution suggests that during the Plio-Pleistocene rifting

normal faults nucleated from underlying late Miocene reverse structures, which resulted from preceding reactivation and upward propagation of intra-basement structures.

4. The normal faults associated to km-wide intra-basement structures (i.e. Type 1) propagated through the entire sedimentary succession, despite being oblique to the regional trend of the rift. This far-reaching influence of km-wide intra-basement structures appears to be at least partially related to the local perturbation of the regional stress field due to pervasive mechanical anisotropies. As distinct fault segments nucleated in the lower and in the upper part of the sedimentary cover, we suggest a form of stress transfer through the sedimentary succession.
5. Nucleation from pre-existing structures and perturbation of the local stress field can be the core of the influence of basement structures on rift-related faults and not just ancillary processes with respect to simple reactivation. Future models for structural inheritance in rifting settings should incorporate long-length influence of pre-existing structures and kinematic coupling between

structures at different levels. Kinematic analysis proved to be a fundamental tool to extract information from 3D seismic data, posing important constraints to analogue and numerical models.

Acknowledgements

Funding for this research was primarily provided by the University of Padova and the Aldo Gini Foundation in the form of a studentship awarded to Luca Collanega. We would like to thank Matteo Massironi, Thomas Phillips, Dancho Azagra and Josè Reis for insightful discussions during the course of this work. We also thank Schlumberger (Petrel) and Badley Geoscience (T7) for providing access to software.

References

Abe, S., van Gent, H., Urai, J.L., 2011. DEM simulation of normal faults in cohesive materials. Tectonophysics 512, 12–21. https://doi.org/10.1016/j.tecto.2011.09.008

Arbaret, L., Burg, J.-P., 2003. Complex flow in lowest crustal, anastomosing mylonites: Strain gradients in a Kohistan gabbro, northern Pakistan. Journal of Geophysical Research: Solid Earth 108. https://doi.org/10.1029/2002JB002295

Bartholomew, I.D., Peters, J.M., Powell, C.M., 1993. Regional structural evolution of the North Sea: oblique slip and the reactivation of basement lineaments. Petroleum Geology Conference Series 4, Geological Society, London, 1109-1122

Baudon, C., Cartwright, J., 2008a. Early stage evolution of growth faults: 3D seismic insights from the Levant Basin, Eastern Mediterranean. Journal of Structural Geology 30, 888–898. https://doi.org/10.1016/j.jsg.2008.02.019

Baudon, C., Cartwright, J., 2008b. The kinematics of reactivation of normal faults using high resolution throw mapping. Journal of Structural Geology 30, 1072–1084. https://doi.org/10.1016/j.jsg.2008.04.008

Baudon, C., Cartwright, J.A., 2008c. 3D seismic characterisation of an array of blind normal faults in the Levant Basin, Eastern Mediterranean. Journal of Structural Geology 30, 746–760. https://doi.org/10.1016/j.jsg.2007.12.008

Beavan, J., Haines, J., 2001. Contemporary horizontal velocity and strain rate fields of the Pacific–Australian plate boundary zone through New Zealand. J. Geophys. Res. 106 (B1), 741–770.

Bell, J.S., 1996. In situ stresses in sedimentary rocks (part 2): applications of stress measurements, Geoscience Canada, 23, 135-153

Bird, P.C., Cartwright, J.A., Davies, T.L., 2015. Basement reactivation in the development of rift basins: an example of reactivated Caledonide structures in the West Orkney Basin. Journal of the Geological Society 172, 77–85. https://doi.org/10.1144/jgs2013-098

Bradshaw, J.D., 1989. Cretaceous geotectonic patterns in the New Zealand Region. Tectonics 8, 803–820. https://doi.org/10.1029/TC008i004p00803

Bradshaw, J.D., 1993. A review of the Median Tectonic Zone: Terrane boundaries and terrane amalgamation near the Median Tectonic Line. New Zealand Journal of Geology and Geophysics 36, 117–125. https://doi.org/10.1080/00288306.1993.9514559

Bradshaw, J.D., Pankhurst, R.J., Weaver, S.D., Storey, B.C., Muir, R.J., Ireland, T.R., 1997. New Zealand Superterranes Recognized in Marie Byrd Land and Thurston Island. Terra

Antartica, 3, 429-436.

Brandes, C., Tanner, D.C., 2014. Fault-related folding: A review of kinematic models and their application. Earth-Science Reviews 138, 352–370. https://doi.org/10.1016/j.earscirev.2014.06.008

Brewer, J.A., Matthews, D.H., Warner, M.R., Hall, J., Smythe, D.K., Whittington, R.J., 1983. BIRPS deep seismic reflection studies of the British Caledonides. Nature 305, 206–210. https://doi.org/10.1038/305206a0

Brocher, T.M., Christensen, N.I., 1990. Seismic anisotropy due to preferred mineral orientation observed in shallow crustal rocks in southern Alaska. Geology 18, 737. https://doi.org/10.1130/0091-7613(1990)018<0737:SADTPM>2.3.CO;2

Carreras, J., Czeck, D.M., Druguet, E., Hudleston, P.J., 2010. Structure and development of an anastomosing network of ductile shear zones. Journal of Structural Geology 32, 656–666. https://doi.org/10.1016/j.jsg.2010.03.013

Cartwright, J.A., Trudgill, B.D., Mansfield, C.S., 1995. Fault growth by segment linkage: an explanation for scatter in maximum displacement and trace length data from the Canyonlands Grabens of SE Utah. Journal of Structural Geology 17, 1319–1326. https://doi.org/10.1016/0191-8141(95)00033-A

Chenrai, P., Huuse, M., 2017. Pockmark formation by porewater expulsion during rapid progradation in the offshore Taranaki Basin, New Zealand. Marine and Petroleum Geology 82, 399–413. https://doi.org/10.1016/j.marpetgeo.2017.02.017

Childs, C., Nicol, A., Walsh, J.J., Watterson, J., 2003. The growth and propagation of synsedimentary faults. Journal of Structural Geology 25, 633–648. https://doi.org/10.1016/S0191-8141(02)00054-8

Claringbould, J.S., Bell, R.E., Jackson, C.A.-L., Gawthorpe, R.L., Odinsen, T., 2017. Pre-existing normal faults have limited control on the rift geometry of the northern North Sea. Earth and Planetary Science Letters 475, 190–206. https://doi.org/10.1016/j.epsl.2017.07.014

Conneally, J., Childs, C., Walsh, J.J., 2014. Contrasting origins of breached relay zone geometries. Journal of Structural Geology 58, 59–68. https://doi.org/10.1016/j.jsg.2013.10.010

Corti, G., Iandelli, I., Cerca, M., 2013. Experimental modeling of rifting at craton margins. Geosphere 9, 138–154. https://doi.org/10.1130/GES00863.1

Corti, G., van Wijk, J., Cloetingh, S., Morley, C.K., 2007. Tectonic inheritance and continental rift architecture: Numerical and analogue models of the East African Rift system. Tectonics 26. https://doi.org/10.1029/2006TC002086

Deng, C., Gawthorpe, R.L., Finch, E., Fossen, H., 2017. Influence of a pre-existing basement weakness on normal fault growth during oblique extension: Insights from discrete element modeling. Journal of Structural Geology 105, 44–61. https://doi.org/10.1016/j.jsg.2017.11.005

Destro, N., 1995. Release fault: A variety of cross fault in linked extensional fault systems, in the Sergipe-Alagoas Basin, NE Brazil. Journal of Structural Geology 17, 615–629. https://doi.org/10.1016/0191-8141(94)00088-H

Duffy, O.B., Bell, R.E., Jackson, C.A.-L., Gawthorpe, R.L., Whipp, P.S., 2015. Fault growth and interactions in a multiphase rift fault network: Horda Platform, Norwegian North Sea. Journal of Structural Geology 80, 99–119. https://doi.org/10.1016/j.jsg.2015.08.015

Erslev, E.A., Mayborn, K.R., 1997. Multiple geometries and modes of fault-propagation folding in the Canadian thrust belt. Journal of Structural Geology 19, 321–335. https://doi.org/10.1016/S0191-8141(97)83027-1

Faccenna, C., Nalpas, T., Brun, J.-P., Davy, P., Bosi, V., 1995. The influence of pre-existing thrust faults on normal fault geometry in nature and in experiments. Journal of Structural Geology 17, 1139–1149. https://doi.org/10.1016/0191-8141(95)00008-2

Fazlikhani, H., Fossen, H., Gawthorpe, R.L., Faleide, J.I., Bell, R.E., 2017. Basement structure and its influence on the structural configuration of the northern North Sea rift. Tectonics 36, 2017TC004514. https://doi.org/10.1002/2017TC004514

Færseth, R.B., Gabrielsen, R.H. & Hurich C.A., 1995. Influence of basement in structuring of North Sea basin, offshore southwest Norway. Norsk Geologisk Tidsskrift 75, 105-119

Fossen, H., Khani, H.F., Faleide, J.I., Ksienzyk, A.K., Dunlap, W.J., 2017. Post-Caledonian extension in the West Norway–northern North Sea region: the role of structural inheritance. Geological Society, London, Special Publications 439, 465–486. https://doi.org/10.1144/SP439.6

Fountain, D.M., Hurich, C.A., Smithson, S.B., 1984. Seismic reflectivity of mylonite zones in the crust. Geology 12, 195. https://doi.org/10.1130/0091-7613(1984)12<195:SROMZI>2.0.CO;2

Gernigon, L., Brönner, M., Roberts, D., Olesen, O., Nasuti, A., Yamasaki, T., 2014. Crustal and basin evolution of the southwestern Barents Sea: From Caledonian orogeny to continental breakup. Tectonics 33, 2013TC003439. https://doi.org/10.1002/2013TC003439

Giba, M., Nicol, A., Walsh, J.J., 2010. Evolution of faulting and volcanism in a back-arc basin and its implications for subduction processes. Tectonics 29, TC4020.

https://doi.org/10.1029/2009TC002634

Giba, M., Walsh, J.J., Nicol, A., 2012. Segmentation and growth of an obliquely reactivated normal fault. Journal of Structural Geology 39, 253–267. https://doi.org/10.1016/j.jsg.2012.01.004

Gudlaugsson, S.T., Faleide, J.I., Johansen, S.E., Breivik, A.J., 1998. Late Palaeozoic structural development of the South-western Barents Sea. Marine and Petroleum Geology 15, 73–102. https://doi.org/10.1016/S0264-8172(97)00048-2

Gupta, A., Scholz, C.H., 2000. A model of normal fault interaction based on observations and theory. Journal of Structural Geology 22, 865–879. https://doi.org/10.1016/S0191-8141(00)00011-0

Gudmundsson, A. 2011. Rock fractures in Geological Processes. Cambridge University Press, Cambridge.

Hansen, R.J., Kamp, P.J., 2004. Rapid progradation of the Pliocene-Pleistocene continental margin, northern Taranaki Basin, New Zealand, and implications. Proceedings of New Zealand Petroleum Conference 1–9.

Hansen, R.J., Kamp, P.J., 2002. Evolution of the Giant Foresets Formation, northern Taranaki Basin, New Zealand.

Henstra, G.A., Rotevatn, A., Gawthorpe, R.L., Ravnås, R., 2015. Evolution of a major segmented normal fault during multiphase rifting: The origin of plan-view zigzag geometry. Journal of Structural Geology 74, 45–63. https://doi.org/10.1016/j.jsg.2015.02.005

Henza, A.A., Withjack, M.O., Schlische, R.W., 2011. How do the properties of a pre-existing normal-fault population influence fault development during a subsequent phase of extension? Journal of Structural Geology 33, 1312–1324. https://doi.org/10.1016/j.jsg.2011.06.010

Henza, A.A., Withjack, M.O., Schlische, R.W., 2010. Normal-fault development during two phases of non-coaxial extension: An experimental study. Journal of Structural Geology 32, 1656–1667. https://doi.org/10.1016/j.jsg.2009.07.007

Holt, W.E., Stern, T.A., 1994. Subduction, platform subsidence, and foreland thrust loading: The late Tertiary development of Taranaki Basin, New Zealand. Tectonics 13, 1068–1092. https://doi.org/10.1029/94TC00454

Homberg, C., Hu, J.C., Angelier, J., Bergerat, F., Lacombe, O., 1997. Characterization of stress perturbations near major fault zones: insights from 2-D distinct-element numerical modelling and field studies (Jura mountains). Journal of Structural Geology 19, 703–718.

https://doi.org/10.1016/S0191-8141(96)00104-6

Hongxing, G., Anderson, J.K., 2007. Fault throw profile and kinematics of Normal fault: conceptual models and geologic examples. Geol. J. China Univ. 13, 75–88.

Hurich, C.A., Smithson, S.B., Fountain, D.M., Humphreys, M.C., 1985. Seismic evidence of mylonite reflectivity and deep structure in the Kettle dome metamorphic core complex, Washington. Geology 13, 577. https://doi.org/10.1130/0091-7613(1985)13<577:SEOMRA>2.0.CO;2

Jackson, C.A.-L., Rotevatn, A., 2013. 3D seismic analysis of the structure and evolution of a salt-influenced normal fault zone: A test of competing fault growth models. Journal of Structural Geology 54, 215–234. https://doi.org/10.1016/j.jsg.2013.06.012

Keep, M., McClay, K.R., 1997. Analogue modelling of multiphase rift systems. Tectonophysics 273, 239–270. https://doi.org/10.1016/S0040-1951(96)00272-7

Kimbrough, D.L., Tulloch, A.J., Geary, E., Coombs, D.S., Landis, C.A., 1993. Isotopic ages from the Nelson region of South Island New Zealand: crustal structure and definition of the Median Tectonic Zone. Tectonophysics 225, 433–448. https://doi.org/10.1016/0040-1951(93)90308-7

King, R.C., Tingay, M.R.P., Hillis, R.R., Morley, C.K., Clark, J., 2010. Present-day stress orientations and tectonic provinces of the NW Borneo collisional margin. J. Geophys. Res. 115, B10415. https://doi.org/10.1029/2009JB006997

King, P.R., Thrasher, G.P., 1996. Cretaceous-Cenozoic geology and petroleum systems of the Taranaki Basin, New Zealand. Institute of Geological and Nuclear Sciences Monographs.

Klemperer, S.L., BIRPS group1, 1987. Reflectivity of the crystalline crust: hypotheses and tests. Geophysical Journal International 89, 217–222. https://doi.org/10.1111/j.1365-246X.1987.tb04411.x

Korme, T., Acocella, V., Abebe, B., 2004. The Role of Pre-existing Structures in the Origin, Propagation and Architecture of Faults in the Main Ethiopian Rift. Gondwana Research 7, 467–479. https://doi.org/10.1016/S1342-937X(05)70798-X

Maerten, L., Gillespie, P., Pollard, D.D., 2002. Effects of local stress perturbation on secondary fault development. Journal of Structural Geology 24, 145–153. https://doi.org/10.1016/S0191-8141(01)00054-2

Maerten, L., Willemse, E.J.M., Pollard, D.D., Rawnsley, K., 1999. Slip distributions on intersecting normal faults. Journal of Structural Geology 21, 259–272. https://doi.org/10.1016/S0191-8141(98)00122-9

Mansfield, C.S., Cartwright, J.A., 1996. High resolution fault displacement mapping from three-dimensional seismic data: evidence for dip linkage during fault growth. Journal of Structural Geology 18, 249–263. https://doi.org/10.1016/S0191-8141(96)80048-4

McConnell, R.B., 1972. Geological Development of the Rift System of Eastern Africa. GSA Bulletin 83, 2549–2572. https://doi.org/10.1130/0016-7606(1972)83[2549:GDOTRS]2.0.CO;2

McConnell, R.B., 1969. East African Rift System. Nature 224, 65. https://doi.org/10.1038/224065a0

McDonough, D.T., Fountain, D.M., 1988. Reflection characteristics of a mylonite zone based on compressional wave velocities of rock samples. Geophysical Journal International 93, 547–558. https://doi.org/10.1111/j.1365-246X.1988.tb03880.x

Mitra, S., 1990. Fault-propagation folds: geometry, kinematic evolution, and hydrocarbon traps. AAPG Bulletin, 74, 921-945.

Moore, M.E., Gleadow, A.J.W., Lovering, J.F., 1986. Thermal evolution of rifted continental margins: new evidence from fission tracks in basement apatites from southeastern Australia. Earth and Planetary Science Letters 78, 255–270. https://doi.org/10.1016/0012-821X(86)90066-X

Morley, C.K., 2017. The impact of multiple extension events, stress rotation and inherited fabrics on normal fault geometries and evolution in the Cenozoic rift basins of Thailand. Geological Society, London, Special Publications 439, 413. https://doi.org/10.1144/SP439.3Morley, C.K., 2014. The widespread occurrence of low-angle normal faults in a rift setting: Review of examples from Thailand, and implications for their origin and evolution. Earth-Science Reviews 133, 18–42. https://doi.org/10.1016/j.earscirev.2014.02.007

Morley, C.K., 2010. Stress re-orientation along zones of weak fabrics in rifts: An explanation for pure extension in “oblique” rift segments? Earth and Planetary Science Letters 297, 667–673. https://doi.org/10.1016/j.epsl.2010.07.022

Morley, C.K., 1999. Influence of Preexisting Fabrics on Rift Structure In: Geoscience of Rift Systems-Evolution of East Africa (Ed. by C.K. Morley) AAPG Studies in Geology No. 44, 151-160

Morley, C.K., 1995. Developments in the structural geology of rifts over the last decade and their impact on hydrocarbon exploration. Geological Society, London, Special Publications 80, 1. https://doi.org/10.1144/GSL.SP.1995.080.01.01

Morley, C.K., Charusiri, P., Watkinson, I.M. (2011) Structural geology of Thailand during the Cenozoic. In: Geology of Thailand (Ed. by M.F. Ridd, A.J. Barber, M.J. Crow) Geological Society, London, Special Publications, 273-334.

Morley, C.K., Gabdi, S., Seusutthiya, K., 2007. Fault superimposition and linkage resulting from stress changes during rifting: Examples from 3D seismic data, Phitsanulok Basin, Thailand. Journal of Structural Geology 29, 646–663. https://doi.org/10.1016/j.jsg.2006.11.005

Morley, C.K., Haranya, C., Phoosongsee, W., Pongwapee, S., Kornsawan, A., Wonganan, N., 2004. Activation of rift oblique and rift parallel pre-existing fabrics during extension and their effect on deformation style: examples from the rifts of Thailand. Journal of Structural Geology 26, 1803–1829. https://doi.org/10.1016/j.jsg.2004.02.014

Mortimer, N., Tulloch, A.J., Ireland, T.R., 1997. Basement geology of Taranaki and Wanganui Basins, New Zealand. New Zealand Journal of Geology and Geophysics 40, 223–236. https://doi.org/10.1080/00288306.1997.9514754

Mortimer, N., Tulloch, A.J., Spark, R.N., Walker, N.W., Ladley, E., Allibone, A., Kimbrough, D.L., 1999. Overview of the Median Batholith, New Zealand: a new interpretation of the geology of the Median Tectonic Zone and adjacent rocks. Journal of African Earth Sciences 29, 257–268. https://doi.org/10.1016/S0899-5362(99)00095-0

Mouslopoulou, V., Nicol, A., Walsh, J.J., Begg, J.G., Townsend, D.B., Hristopulos, D.T., 2012. Fault-slip accumulation in an active rift over thousands to millions of years and the importance of paleoearthquake sampling. Journal of Structural Geology 36, 71–80. https://doi.org/10.1016/j.jsg.2011.11.010

Muir, R.J., Bradshaw, J.D., Weaver, S.D., Laird, M.G., 2000. The influence of basement structure on the evolution of the Taranaki Basin, New Zealand. Journal of the Geological Society 157, 1179–1185. https://doi.org/10.1144/jgs.157.6.1179

Muraoka, H., Kamata, H., 1983. Displacement distribution along minor fault traces. Journal of Structural Geology 5, 483–495. https://doi.org/10.1016/0191-8141(83)90054-8

Nicol, A., Walsh, J., Berryman, K., Nodder, S., 2005. Growth of a normal fault by the accumulation of slip over millions of years. Journal of Structural Geology 27, 327–342. https://doi.org/10.1016/j.jsg.2004.09.002

Nicol, A., Watterson, J., Walsh, J.J., Childs, C., 1996. The shapes, major axis orientations and displacement patterns of fault surfaces. Journal of Structural Geology 18, 235–248. https://doi.org/10.1016/S0191-8141(96)80047-2

Peace, A., McCaffrey, K., Imber, J., van Hunen, J., Hobbs, R., Wilson, R., 2017. The role of pre-existing structures during rifting, continental breakup and transform system development, offshore West Greenland. Basin Research. https://doi.org/10.1111/bre.12257

Phillips, T.B., Jackson, C.A.-L., Bell, R.E., Duffy, O.B., 2018. Oblique reactivation of lithosphere-scale lineaments controls rift physiography – the upper-crustal expression of the Sorgenfrei–Tornquist Zone, offshore southern Norway. Solid Earth 9, 403–429. https://doi.org/10.5194/se-9-403-2018

Phillips, T.B., Jackson, C.A.-L., Bell, R.E., Duffy, O.B., Fossen, H., 2016. Reactivation of intrabasement structures during rifting: A case study from offshore southern Norway. Journal of Structural Geology 91, 54–73. https://doi.org/10.1016/j.jsg.2016.08.008

Reeve, M.T., Bell, R.E., Duffy, O.B., Jackson, C.A.-L., Sansom, E., 2015. The growth of non-colinear normal fault systems; What can we learn from 3D seismic reflection data? Journal of Structural Geology 70, 141–155. https://doi.org/10.1016/j.jsg.2014.11.007

Reeve, M.T., Bell, R.E., Jackson, C.A.L., 2014. Origin and significance of intra-basement seismic reflections offshore western Norway. Journal of the Geological Society 171, 1. https://doi.org/10.1144/jgs2013-020

Reilly, C., Nicol, A., Walsh, J.J., Seebeck, H., 2015. Evolution of faulting and plate boundary deformation in the Southern Taranaki Basin, New Zealand. Tectonophysics 651–652, 1–18. https://doi.org/10.1016/j.tecto.2015.02.009

Rennie, S.F., Fagereng, Å., Diener, J.F.A., 2013. Strain distribution within a km-scale, mid-crustal shear zone: The Kuckaus Mylonite Zone, Namibia. Journal of Structural Geology 56, 57–69. https://doi.org/10.1016/j.jsg.2013.09.001

Ring, U., 1994. The influence of preexisting structure on the evolution of the Cenozoic Malawi rift (East African rift system). Tectonics 13, 313–326. https://doi.org/10.1029/93TC03188

Roberts, A.M., Holdsworth, R.E., 1999. Linking onshore and offshore structures: Mesozoic extension in the Scottish Highlands. Journal of the Geological Society 156, 1061–1064. https://doi.org/10.1144/gsjgs.156.6.1061

Robin, P.-Y.F., 1979. Theory of metamorphic segregation and related processes. Geochimica et Cosmochimica Acta 43, 1587–1600. https://doi.org/10.1016/0016-7037(79)90179-0

Rotevatn, A., Kristensen, T.B., Ksienzyk, A.K., Wemmer, K., Henstra, G.A., Midtkandal, I., Grundvåg, S.A., Andresen, A., 2018. Structural Inheritance and Rapid Rift-Length Establishment in a Multiphase Rift: The East Greenland Rift System and its Caledonian Orogenic Ancestry. Tectonics 37, 1858–1875. https://doi.org/10.1029/2018TC005018

Scott, J.M., 2013. A review of the location and significance of the boundary between the Western Province and the Eastern Province, New Zealand. New Zealand Journal of Geology and Geophysics 56, 276-293, doi:10.1080/00288306.2013.812971

Seebeck, H., Nicol, A., Villamor, P., Ristau, J., Pettinga, J., 2014. Structure and kinematics of the Taupo Rift, New Zealand. Tectonics 33, 1178–1199. https://doi.org/10.1002/2014TC003569

Sibson, R.H., 1995. Selective fault reactivation during basin inversion: potential for fluid redistribution through fault-valve action. Geological Society, London, Special Publications 88, 3–19. https://doi.org/10.1144/GSL.SP.1995.088.01.02

Sibson, R.H., 1985. A note on fault reactivation. Journal of Structural Geology 7, 751–754. https://doi.org/10.1016/0191-8141(85)90150-6

Stagpoole, V., Nicol, A., 2008. Regional structure and kinematic history of a large subduction back thrust: Taranaki Fault, New Zealand. Journal of Geophysical Research 113. https://doi.org/10.1029/2007JB005170

Stern, T.A., Davey, F.J., 1990. Deep seismic expression of a foreland basin: Taranaki basin, New Zealand. Geology 18, 979–982. https://doi.org/10.1130/0091-7613(1990)018<0979:DSEOAF>2.3.CO;2

Strogen, D.P., 2011. Updated paleogeographic maps for the Taranaki Basin and surrounds. Lower Hutt, New Zealand: GNS Science.

Strogen, D.P., Bland, K.J., Nicol, A., King, P.R., 2014. Paleogeography of the Taranaki Basin region during the latest Eocene–Early Miocene and implications for the "total drowning" of Zealandia. New Zealand Journal of Geology and Geophysics 57, 110–127. https://doi.org/10.1080/00288306.2014.901231

Strogen, D.P., Seebeck, H., Nicol, A., King, P.R., 2017. Two-phase Cretaceous–Paleocene rifting in the Taranaki Basin region, New Zealand; implications for Gondwana break-up. Journal of the Geological Society 174, 929–946. https://doi.org/10.1144/jgs2016-160

Sun, S., Hou, G., Zheng, C., 2017. Fracture zones constrained by neutral surfaces in a fault-related fold: Insights from the Kelasu tectonic zone, Kuqa Depression. Journal of Structural Geology 104, 112–124. https://doi.org/10.1016/j.jsg.2017.10.005

Taylor, S.K., Nicol, A., Walsh, J.J., 2008. Displacement loss on growth faults due to sediment compaction. Journal of Structural Geology 30, 394–405. https://doi.org/10.1016/j.jsg.2007.11.006

Tingay, M.R.P., Morley, C.K., Hillis, R.R., Meyer, J., 2010. Present-day stress orientation in

Thailand's basins. Journal of Structural Geology 32, 235–248. https://doi.org/10.1016/j.jsg.2009.11.008

Trudgill, B.D., 2002. Structural controls on drainage development in the Canyonlands grabens of southeast Utah. AAPG Bulletin 86, 1095–1112.

Vass, A., Koehn, D., Toussaint, R., Ghani, I., Piazolo, S., 2014. The importance of fracture-healing on the deformation of fluid-filled layered systems. Journal of Structural Geology 67, 94–106. https://doi.org/10.1016/j.jsg.2014.07.007

Walsh, J.., Bailey, W.., Childs, C., Nicol, A., Bonson, C.., 2003. Formation of segmented normal faults: a 3-D perspective. Journal of Structural Geology 25, 1251–1262. https://doi.org/10.1016/S0191-8141(02)00161-X

Walsh, J.J., Watterson, J., 1991. Geometric and kinematic coherence and scale effects in normal fault systems. Geological Society, London, Special Publications 56, 193–203. https://doi.org/10.1144/GSL.SP.1991.056.01.13

Walsh, J.J., Watterson, J., 1987. Distributions of cumulative displacement and seismic slip on a single normal fault surface. Journal of Structural Geology 9, 1039–1046. https://doi.org/10.1016/0191-8141(87)90012-5

Wang, C.-Y., Okaya, D.A., Ruppert, C., Davis, G.A., Guo, T.-S., Zhong, Z., Wenk, H.-R., 1989. Seismic reflectivity of the Whipple Mountain shear zone in southern California. J. Geophys. Res. 94, 2989–3005. https://doi.org/10.1029/JB094iB03p02989

Whipp, P.S., Jackson, C.A.L., Gawthorpe, R.L., Dreyer, T., Quinn, D., 2014. Normal fault array evolution above a reactivated rift fabric; a subsurface example from the northern Horda Platform, Norwegian North Sea. Basin Research 26, 523–549. https://doi.org/10.1111/bre.12050

Wilson, R.W., McCaffrey, K.J.W., Holdsworth, R.E., Imber, J., Jones, R.R., Welbon, A.I.F., Roberts, D., 2006. Complex fault patterns, transtension and structural segmentation of the Lofoten Ridge, Norwegian margin: Using digital mapping to link onshore and offshore geology: TRANSTENSION AND SEGMENTATION IN LOFOTEN. Tectonics 25, n/a-n/a. https://doi.org/10.1029/2005TC001895

Withjack, M.O., Henza, A.A., Schlische, R.W., 2017. Three-dimensional fault geometries and interactions within experimental models of multiphase extension. AAPG Bulletin 101, 1767–1789. https://doi.org/10.1306/02071716090

Ying-Zhen, Z., Dusseault, M.B., Yassir, N.A., 1994. Effects of rock anisotropy and heterogeneity on stress distributions at selected sites in North America. Engineering Geology 37, 181–

197. https://doi.org/10.1016/0013-7952(94)90055-8

APPENDIX A

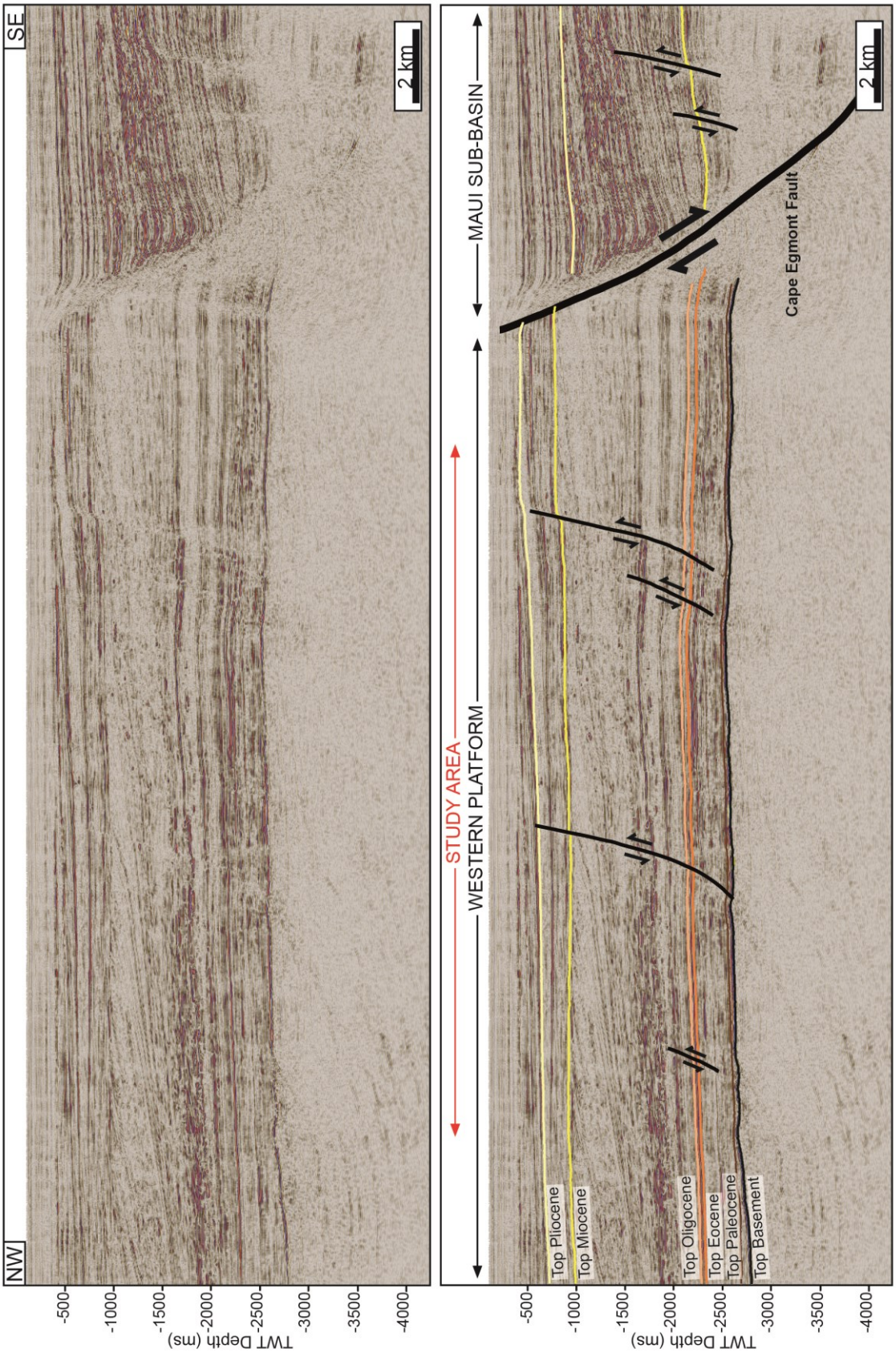

Fig. 2B (Expanded). Uninterpreted (top) and interpreted (bottom) regional seismic line oriented orthogonal to the Cape Egmont Fault (CEF), with main stratigraphic units and location of the study area shown (see Fig. 1 for location). CEF defines the boundary between the relatively low-strain, stratigraphically simple Western Platform (to the west) and the high-subsidence Maui Sub-basin (to the east) (stratigraphic correlation across the Cape Egmont Fault based on Nicol et al., 2005).

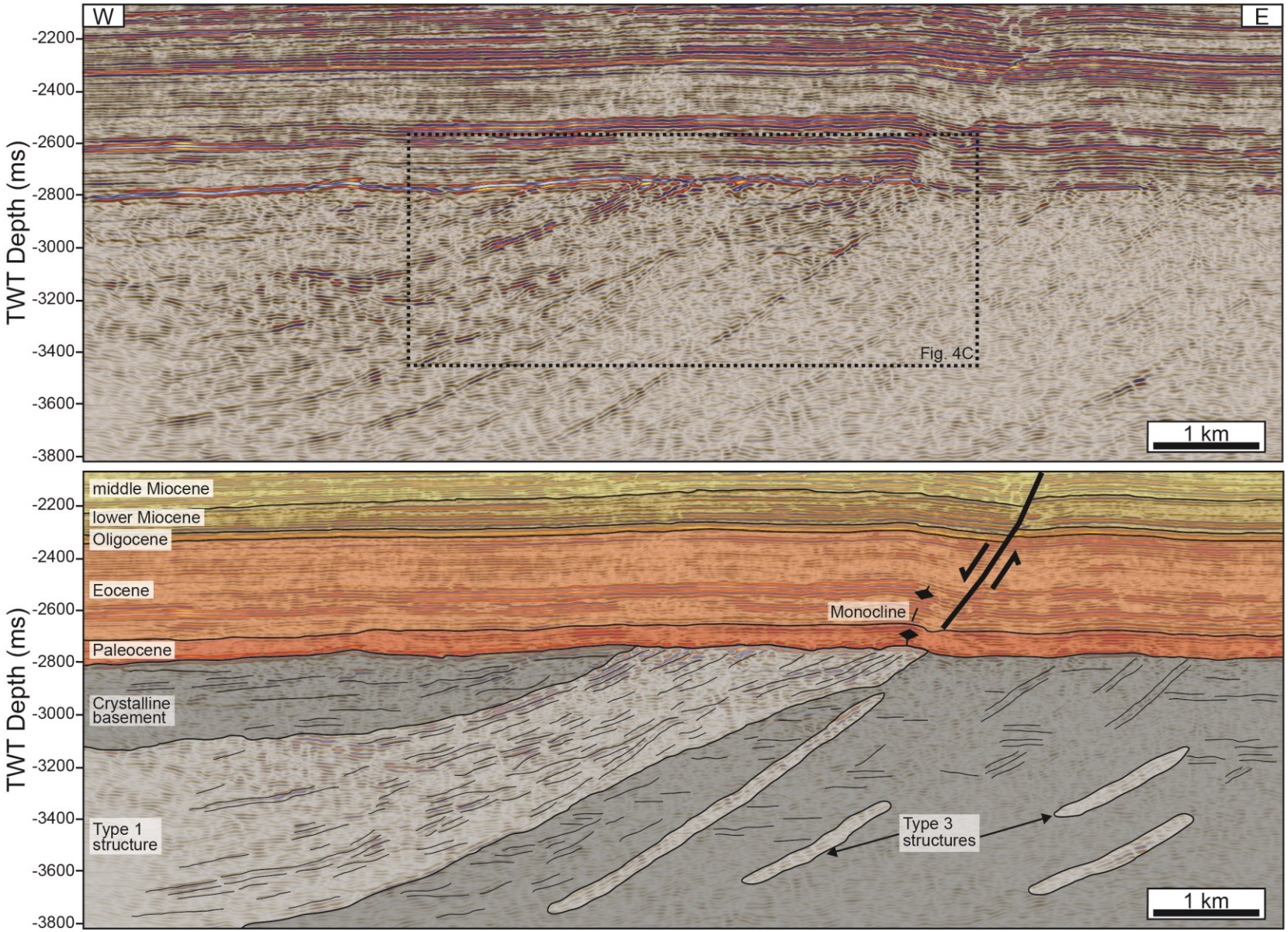

Fig. 4A (Expanded). Uninterpreted (top) and interpreted (bottom) seismic profile oriented orthogonal to the Type 1 intra-basement structure in the northern part of the survey area (location shown in Fig. 5C). The Type 1 structure is defined by high-amplitude reflections at the boundaries, which delimit a zone of chaotic seismic reflections towards the centre of the structure. At Top Basement level, this intra-basementstructure is physically connected to a fault of the cover sequence, which displays negative throw immediately above Top Basement, passing upwards to positive throw.

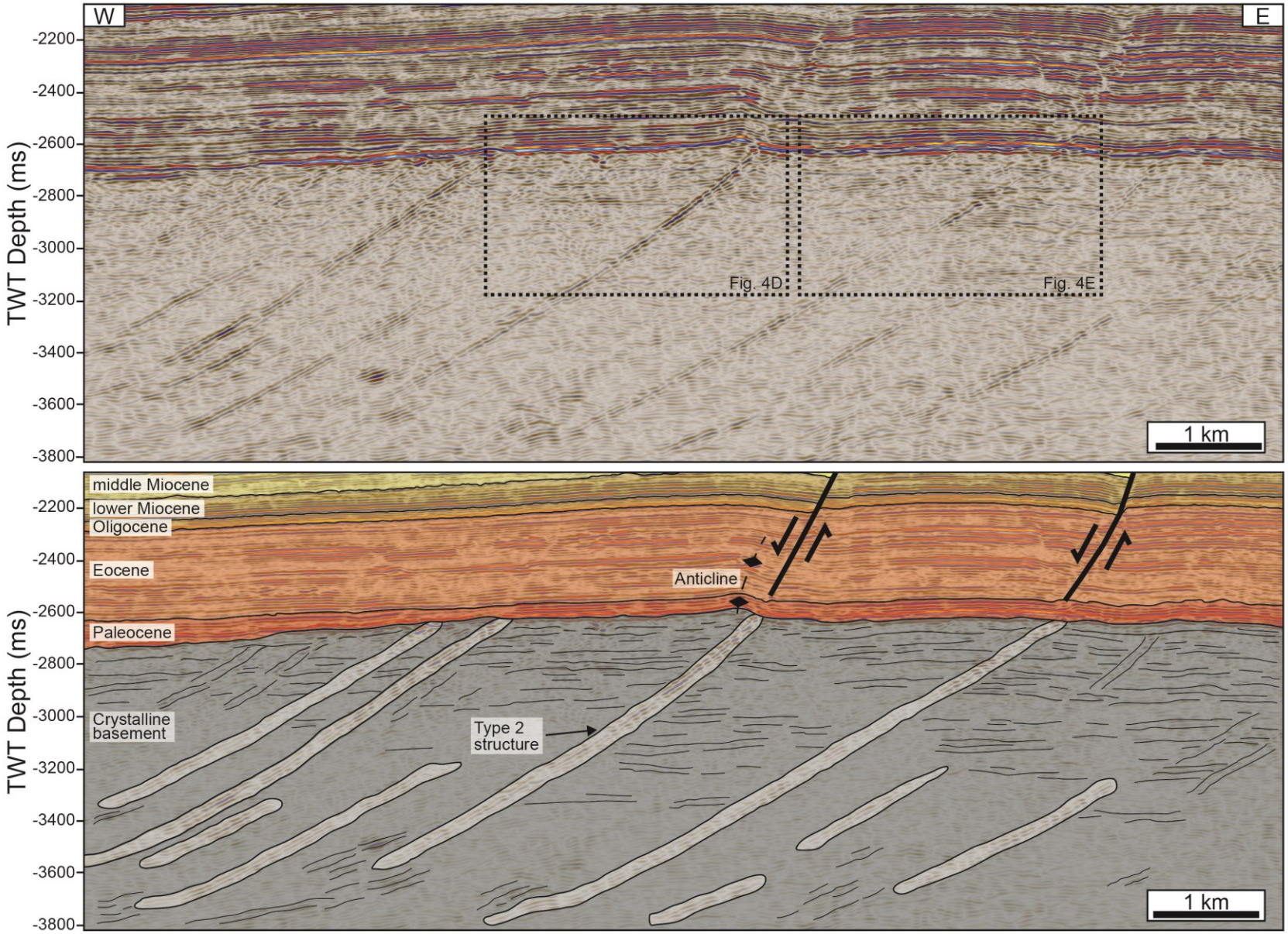

Fig. 4B (Expanded). Uninterpreted (top) and interpreted (bottom) seismic profile oriented orthogonal to the Type 2 and Type 3 intra-basement structures in the central part of the survey area (location shown in Fig. 5C). Type 2 structures are defined by high-amplitude, continuous reflections, which commonly offset the Top Basement; whereas Type 3 structures are defined by weak, vertically segmented reflections, which are typically erosively truncated by the Top Basement. At Top Basement level, Type 2 structures are often physically connected to overlying faults of the cover sequence, which typically display negative throw immediately above Top Basement, passing upwards to positive throw.

APPENDIX B

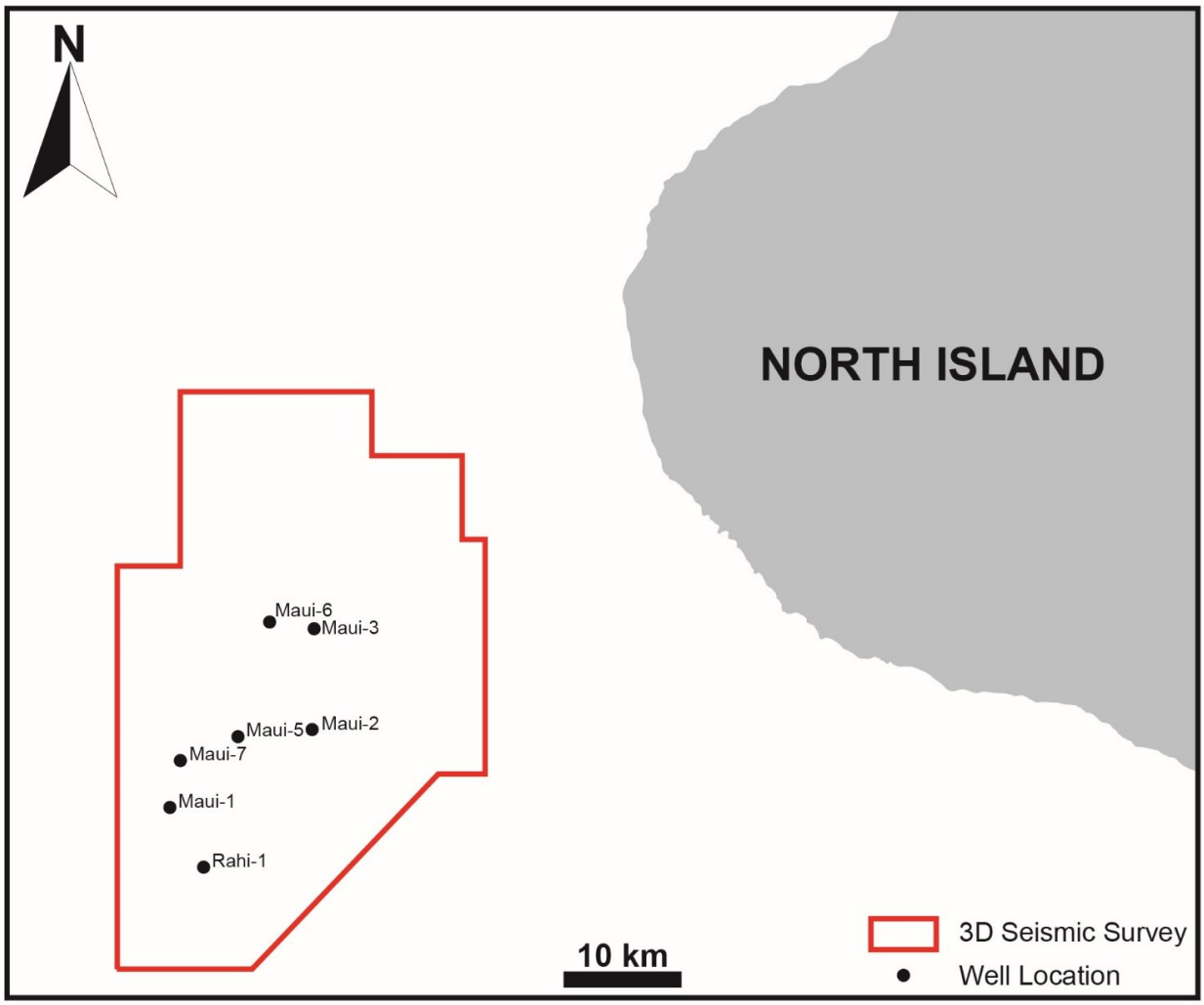

Appendix B. Map illustrating the location of the 3D seismic survey and wells used in this study.

APPENDIX C

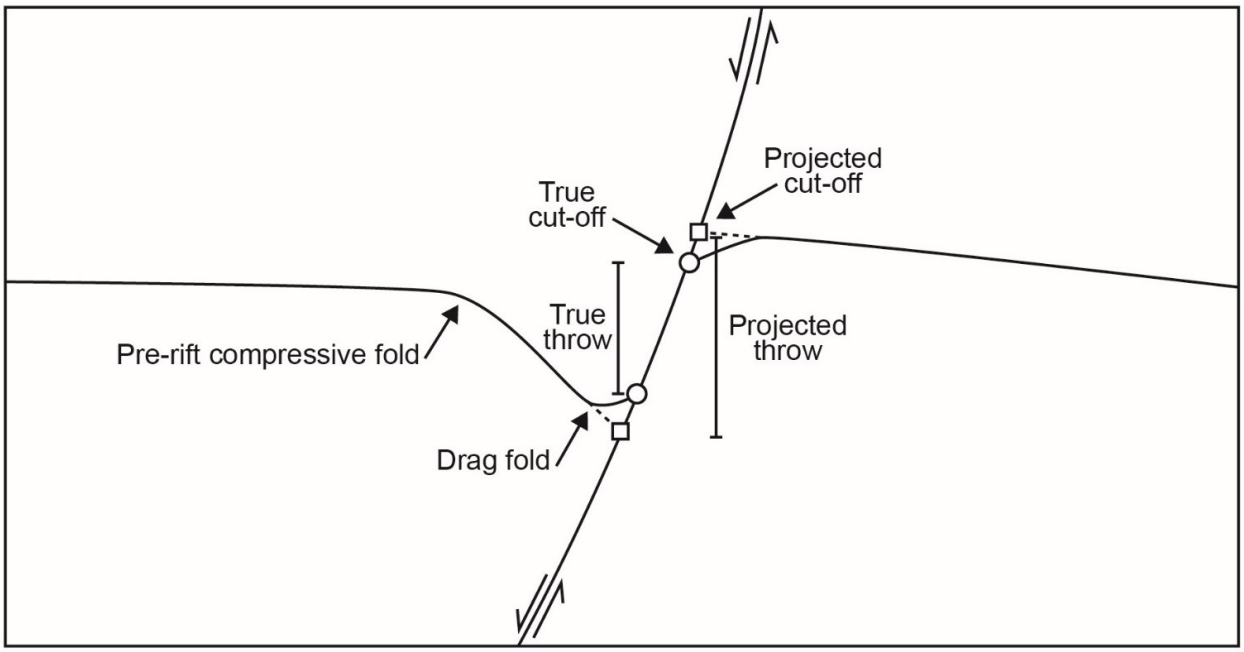

Appendix C. Schematic diagram illustrating the difference between true and projected throw.

APPENDIX D

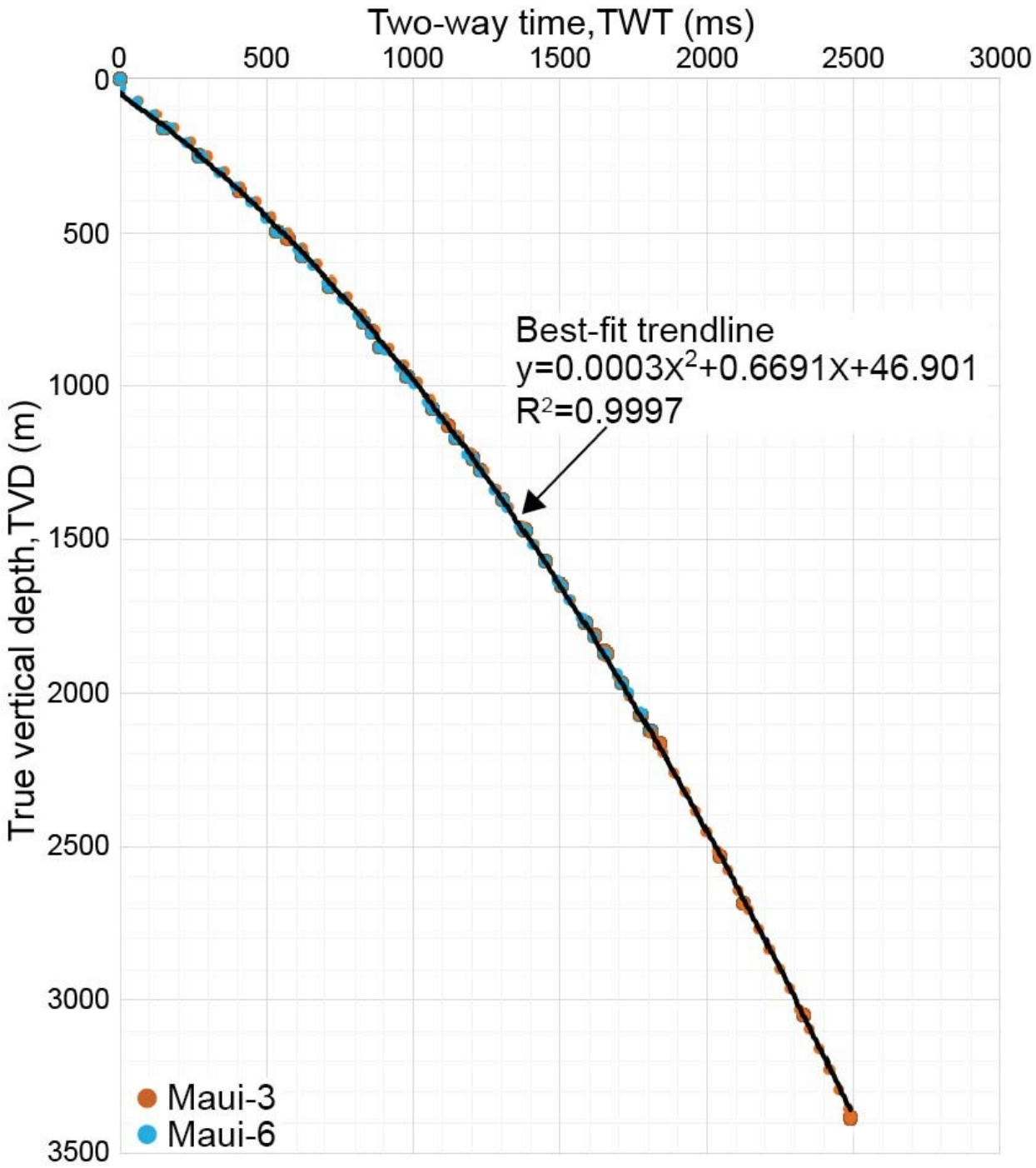

Appendix D. Time-depth curves from two wells in close proximity to the key faults analysed in this study and the best-fit trendline, which was used for depth conversion.

CONCLUSIONS

1. Concluding remarks

This thesis provides strong evidence for polymodal faulting at the 10s of km scale in two different extensional tectonic settings: the Barents Sea rift-shear margin (**Paper 1**) and the Taranaki Basin back-arc rift (**Paper 3**). The occurrence of polymodal faulting has potentially a strong impact on the reconstruction of the structural histories of these sedimentary basins, reducing the number of tectonic phases necessary to account for the different fault systems. Although studies at the scale of the whole platform/basin are required to assess the tectonic significance of polymodal faulting, this concept may change our understanding of plate tectonics, implying that the regional stress field is more stable than previously thought.

Comparing the Barents Sea rift-shear margin and the Taranaki back-arc rift, the driving mechanism of polymodal faulting appears related to the tectonic setting. The interactions between different rift systems make rift-shear margins prone to the onset of 3D strain fields (*cf.* McCormack and McClay, 2018); whereas in the back-arc rift Taranaki Basin, pre-existing compressive structures acted as a template for later normal faults, resulting in the simultaneous development of faults with different strikes.

This thesis shows that in 3D strain fields the strike of new faults responds primary to the influence of adjacent, more developed faults and, secondly, to the regional strain field (**Paper 2**). Although no direct measurements of the stress field have been performed in the analogue models, the alternated development of faults perpendicular one to the other suggests a direction-sensitive stress drop. Similarly, new faults propagating outwards from pre-existing faults tend to strike perpendicularly to the pre-existing faults rather than to the regional extension direction (Henza *et al.*, 2010; Deng *et al.*, 2018). These deviations from the regional trend suggest that local perturbation of the regional stress field may represent a key control on fault patterns in complex and instable strain fields.

The analysis of polymodal faulting in the Taranaki Basin highlights that deep pre-existing structures can affect the strike and distribution of overlying normal faults even without being directly reactivated during the extension (**Paper 3**). Our reconstruction of the growth history of normal faults shows that preferential nucleation from pre-existing weaknesses and local perturbations of the regional stress field may strongly constrain the development of normal faults.

In conclusion, this thesis suggests that complex fault patterns may not necessarily be the mirror of a complex tectonic history but may result from the intrinsic complexity of deformation processes,

which appear strongly susceptible to local perturbations arising from pre-existing as well as developing structures.

2. Future developments

In this thesis, time-thickness variations across faults were used to constrain the activity ranges of normal faults, inferring the simultaneous activity of two different fault systems in the Hoop Fault Complex, SW Barents Sea (**Paper 1**). However, time-thickness variations do not provide any information regarding the genetic relationships between the two fault systems. The throw distribution on the fault planes may be used to reconstruct how the normal faults nucleated and grew, with the throw distribution along strike (i.e. T-x plots) being the best tool to infer if faults of each system nucleated from faults of the other. In particular, it is expected a different structural style with respect to the one observed for multiphase rifts, where 2nd-phase faults generally nucleated from 1st-phase faults (Duffy *et al.*, 2015). Kinematic analyses might also help to rule out an influence of pre-existing structures on the faults of the orthorhombic system. Indeed, T-z plots are expected to show a D-shaped throw profile (typical of normal faults developed independently of pre-existing structures; e.g. Walsh and Watterson, 1987), rather than a B-shaped throw profile (characteristic of normal faults resulting from the linkage of once-distinct vertical segments; e.g. Mansfield and Cartwright, 1996). Moreover, as we suggested in **Paper 1**, the absence of systematic cross-cutting relationships between the two newly-formed fault systems supports their coeval development. A topological analysis of their intersection style would represent a more detailed and rigorous approach for characterising their cross-cutting relationships (cf. Morley and Nixon, 2016; Duffy *et al.*, 2017).

In this thesis, the strain field associated with the orthorhombic system was inferred from the geometric parameters of the faults according to the model of Krantz (1988). However, our analogue models (**Paper 2**) suggest that the principal strain axes should be placed perpendicularly to the fault systems rather than along their bisectors, as predicted by Reches and Krantz (e.g. Reches, 1978; Reches, 1983; Krantz, 1988). This discrepancy between our models (**Paper 2**) and the theory of Reches may be clarified by inferring the strain field directly from the seismic data (**Paper 1**), summing the fault heaves for each fault set along different cross-sections (e.g. Rouby *et al.*, 1996; Coleman *et al.*, 2017) or inverting the fault-slip data (e.g. Angelier, 1984; Xu, 2004; Shan and Fry, 2006). Futhermore, the complexity of our models should be increased to account for the obliquity and the relative magnitude of the applied extension directions.

Finally, one of the most interesting and novel results of this thesis is represented by the far-reaching influence of km-wide intra-basement structures, which was highlighted in the Taranaki Basin (**Paper 3**). However, the mechanism through which this far-reaching influence takes place is yet to be understood. A discrete element model (cf. Homberg *et al.*, 1997) may clarify if and to which extent stress perturbation can propagate away from the anisotropic medium where they originate.

References

Angelier, J., 1984. Tectonic analysis of fault slip data sets. Journal of Geophysical Research: Solid Earth 89, 5835–5848. https://doi.org/10.1029/JB089iB07p05835

Coleman, A.J., Jackson, C.A.-L., Duffy, O.B., 2017. Balancing sub- and supra-salt strain in salt-influenced rifts: Implications for extension estimates. Journal of Structural Geology 102, 208–225. https://doi.org/10.1016/j.jsg.2017.08.006

Deng, C., Gawthorpe, R.L., Fossen, H., Finch, E., 2018. How Does the Orientation of a Preexisting Basement Weakness Influence Fault Development During Renewed Rifting? Insights From Three-Dimensional Discrete Element Modeling. Tectonics 37, 2221–2242. https://doi.org/10.1029/2017TC004776

Duffy, O.B., Bell, R.E., Jackson, C.A.-L., Gawthorpe, R.L., Whipp, P.S., 2015. Fault growth and interactions in a multiphase rift fault network: Horda Platform, Norwegian North Sea. Journal of Structural Geology 80, 99–119. https://doi.org/10.1016/j.jsg.2015.08.015

Duffy, O.B., Nixon, C.W., Bell, R.E., Jackson, C.A.-L., Gawthorpe, R.L., Sanderson, D.J., Whipp, P.S., 2017. The topology of evolving rift fault networks: Single-phase vs multi-phase rifts. Journal of Structural Geology 96, 192–202. https://doi.org/10.1016/j.jsg.2017.02.001

Henza, A.A., Withjack, M.O., Schlische, R.W., 2010. Normal-fault development during two phases of non-coaxial extension: An experimental study. Journal of Structural Geology 32, 1656–1667. https://doi.org/10.1016/j.jsg.2009.07.007

Krantz, R.W., 1988. Multiple fault sets and three-dimensional strain: Theory and application. Journal of Structural Geology 10, 225–237. https://doi.org/10.1016/0191-8141(88)90056-9

Mansfield, C.S., Cartwright, J.A., 1996. High resolution fault displacement mapping from three-dimensional seismic data: evidence for dip linkage during fault growth. Journal of Structural Geology 18, 249–263. https://doi.org/10.1016/S0191-8141(96)80048-4

McCormack, K.D., McClay, K.R., 2018. Orthorhombic faulting in the Beagle Sub-basin, North West Shelf, Australia. Geological Society, London, Special Publications SP476.3. https://doi.org/10.1144/SP476.3

Morley, C.K., Nixon, C.W., 2016. Topological characteristics of simple and complex normal fault networks. Journal of Structural Geology 84, 68–84. https://doi.org/10.1016/j.jsg.2016.01.005

Reches, Z., 1983. Faulting of rocks in three-dimensional strain fields II. Theoretical analysis. Tectonophysics 95, 133–156. https://doi.org/10.1016/0040-1951(83)90264-0

Reches, Z., 1978. Analysis of faulting in three-dimensional strain field. Tectonophysics 47, 109–129. https://doi.org/10.1016/0040-1951(78)90154-3

Rouby, D., Fossen, H., Cobbold, P.R., 1996. Extension, displacement, and block rotation in the larger Gullfaks area, northern North Sea: determined from map view restoration. AAPG Bull. 80 (6), 875e889.

Shan, Y., Fry, N., 2006. The moment method used to infer stress from fault/slip data in sigma space: invalidity and modification. Journal of Structural Geology 28, 1208–1213. https://doi.org/10.1016/j.jsg.2006.03.002

Walsh, J.J., Watterson, J., 1987. Distributions of cumulative displacement and seismic slip on a single normal fault surface. Journal of Structural Geology 9, 1039–1046. https://doi.org/10.1016/0191-8141(87)90012-5

Xu, P., 2004. Determination of regional stress tensors from fault-slip data. Geophysical Journal International 157, 1316–1330. https://doi.org/10.1111/j.1365-246X.2004.02271.x